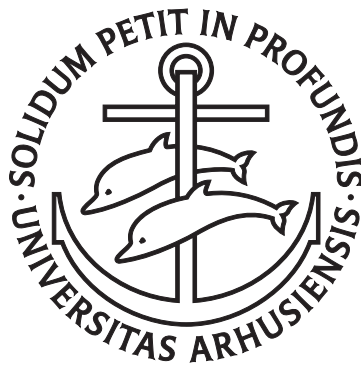

Cold atoms in one-dimensional periodic potentials



Rune Tousgaard Piił

Lundbeck Foundation Theoretical Center for Quantum System Research
Department of Physics and Astronomy
University of Aarhus
DK-8000 Århus C
Denmark

PhD Thesis
November 2008

This thesis is submitted to the Faculty of Science at the University of Aarhus, Denmark, in order to fulfill the requirements for obtaining the PhD degree in Physics. The studies have been carried out under the supervision of Professor Klaus Mølmer in the Lundbeck Foundation Theoretical Center for Quantum System Research at the Department of Physics and Astronomy.

Preface

In this dissertation you will find a presentation of work in which I have been involved during my PhD program. The research was carried out in the period from February 1st 2005 to November 7th 2008 under supervision of Klaus Mølmer. Most of the work covered in this thesis has been presented in the publications listed below. I hope, however, in this document the reader will find a comprehensive introduction to my research. Moreover, some of the work, in particular chapter 7, covers unpublished work.

List of publications

- i R. Piil and K. Mølmer, *Tunneling couplings in discrete lattices, single-particle band structure, and eigenstates of interacting atom pairs*, Phys. Rev. A **76**, 023607 (2007)
- ii N. Nygaard, R. Piil and K. Mølmer, *Feshbach molecules in a one-dimensional optical lattice*, Phys. Rev. A **77**, 021601(R) (2008)
- iii N. Nygaard, R. Piil and K. Mølmer, *Two-channel Feshbach physics in a structured continuum*, Phys. Rev. A **78**, 023617 (2008)
- iv R. T. Piil, N. Nygaard and K. Mølmer, *Scattering and binding of different atomic species in a one-dimensional optical lattice*, Phys. Rev. A **78**, 033611 (2008)

Acknowledgments

First of all, I would like to thank my supervisor Klaus Mølmer for his encouragement and support. His commitment to physics has been a great inspiration and motivation. He always has time for an enthusiastic discussion and always has a solution at hand for all the troubles I have had.

I would also like to sincerely thank my college Nicolai Nygaard, with whom I have had fruitful and educational collaboration. His insight and enthusiasm have been inspiring. I am deeply indebted to him for thoroughly proofreading the entire thesis providing enormous suggestions for enhancements.

Moreover, I am very thankful for Klaus Mølmer proofreading a chapter of my thesis in the last minute and my wife for proofreading an early draft of the entire document. I would also like to acknowledge my fellow students and the group members of the Lundbeck Foundation Theoretical Center for Quantum System Research for an enjoyable time and for creating a productive atmosphere.

Finally, I owe much to my family and friends for always supporting me and especially my parents for always believing in me and encouraging me to achieve my goals. Last but not least I would like to thank my lovely wife for her support without which I would certainly not have been where I am today, and my daughter for bringing tears and laughter into my life.

Contents

1	Introduction and thesis outline	1
1.1	Introduction	1
1.2	Outline of the thesis	3
2	Ultracold atoms in optical lattices	5
2.1	Introduction	5
2.2	Optical lattices	6
2.3	Reduced dimensionality	7
2.4	Single particle states in a periodic potential	8
2.5	Wannier functions	8
2.6	Tunneling amplitudes	10
2.7	Nearest-neighbor approximation	13
2.8	Energy dispersion derivatives	13
2.8.1	Group velocity	14
2.8.2	Effective mass	14
2.8.3	Density of states	14
2.9	Time-of-flight measurements	16
2.10	Conclusion	16
3	Two-particle states in a discrete basis	19
3.1	Introduction	19
3.2	Noninteracting particles	20
3.3	Interaction potential	23
3.4	Green's functions	23
3.4.1	Useful relations for the Green's function	24
3.4.2	Interacting pairs	25
3.5	Scattering properties	26
3.5.1	Transmission profile	26
3.5.2	Identical particles	28
3.5.3	Scattering length	28
3.6	Bound states	30
3.6.1	Pair tunneling	30
3.6.2	Bound state wave functions	31
3.6.3	Repulsively bound atom pairs	33
3.6.4	Investigating the bound state wave functions	33

3.6.5	Symmetries	34
3.7	Spectral analysis	34
3.7.1	Non-interaction particles	35
3.7.2	Interacting particles	35
3.8	Conclusion	36
4	Two-channel Feshbach model	37
4.1	Introduction	37
4.2	Two-channel picture	41
4.2.1	Energy of the resonance state	41
4.2.2	Lattice part of the resonance shift	42
4.3	The coupling matrix	43
4.4	Scattering properties	44
4.4.1	Transmission profile	45
4.4.2	Spectroscopic probing of the Fano profile	49
4.4.3	Scattering length	50
4.4.4	Sweep experiment	52
4.5	Bound states	54
4.5.1	Pair tunneling	56
4.5.2	Binding energy	57
4.5.3	Motionally bound states	58
4.5.4	Bound state wave functions	59
4.6	Spectral analysis	61
4.6.1	The closed channel	61
4.6.2	The open channel	63
4.7	Inclusion of higher Bloch bands	63
4.7.1	Generalized coupling elements	63
4.7.2	Validity of the lowest band approximation	64
4.7.3	Corrections due to higher atomic Bloch bands	66
4.8	Conclusion	67
5	Heteronuclear atomic pairs	69
5.1	Introduction	69
5.2	Noninteracting atoms	70
5.2.1	Alternative coordinates	73
5.3	Green's functions	74
5.4	Scattering properties	74
5.4.1	Transmission profile	75
5.5	Bound states	76
5.5.1	Pair tunneling	76
5.5.2	Bound states wave functions	76
5.5.3	Experimental observation of T_K	78
5.5.4	Correlation function	78
5.6	Inclusion of a Feshbach resonance	80
5.6.1	Sweep experiment	80
5.6.2	Two-channel pair tunneling	80
5.7	Conclusion	81

6	Two-body dynamics beyond nearest-neighbor tunneling	83
6.1	Introduction	83
6.2	Noninteracting atoms	83
6.3	On-site versus off-site interaction	86
6.4	Green's functions	88
6.5	Scattering properties	88
6.6	Bound states	90
6.6.1	Bound state wave functions	90
6.7	Conclusion	92
7	Four-wave mixing	95
7.1	Introduction	95
7.2	Two-body description	98
7.3	Many-body dynamics	102
7.3.1	Condensate dynamics	102
7.4	The Bose-Hubbard model	103
7.5	The Gutzwiller approximation	107
7.6	The truncated Wigner method	108
7.7	Simulations	110
7.8	Conclusion	115
8	Conclusion and outlook	117
8.1	Outlook	118
A	Various useful calculations	121
A.1	Normalization of Bloch waves	121
A.1.1	Single-particle wave functions	121
A.1.2	Two-particle wave functions	122
A.2	Derivation of the noninteracting two-body Hamiltonian	122
A.3	Calculation of the noninteracting Green's function	123
A.3.1	Nearest-neighbor approximation	125
A.3.2	Next-nearest-neighbor tunneling	126
B	Stochastic Gutzwiller method	131
B.1	Error estimation in the Stochastic Gutzwiller Method	135
	Bibliography	139

Chapter 1

Introduction and thesis outline

1.1 Introduction

The field of trapped cold atoms and molecules has experienced growing interest over the last two decades. Several advanced cooling schemes have been developed, which have made physical systems with effectively zero temperature available. The ultracold atomic gases are held by magnetic and optical fields, and have shown to be excellent for testing fundamental theories of quantum physics: new states of matter have been explored and exotic quantum states realized. Moreover, several useful applications have been suggested, mostly for quantum computing and communication but also to perform high precision measurements.

In a standing electromagnetic wave created by counterpropagating lasers the atoms experience a periodic potential due to the regular intensity variation. This is because the internal energy levels will be shifted due to the presence of the field causing the atoms to seek towards either high or low intensity regions depending on the detuning of the laser with respect to the internal energy levels. This lattice structure is referred to as an optical lattice and almost any kind of lattice geometries are possible by the right choose of laser configuration [5–8].

An optical lattice is indeed a very versatile tool. A weak optical lattice can be used to change the effective mass of the trapped atoms, which influence how the atoms react to external forces and the interatomic interaction [9–11]. Whereas very deep lattices can prevent the atoms from moving along specific directions, which effectively reduces the dimensionality of a quantum gas to two, one or even zero dimensions [12–14]. In the intermediate regime the atomic gas is well characterized by the (Bose-)Hubbard model known from solid state physics. Many kinds of different Hubbard models can be realised with cold atoms in optical lattices, where both geometries and coupling parameters can be dynamical changed by adjusting the laser intensities and alignment. This has led to the suggestion that ultracold quantum gases may

be used as a quantum computer for simulating solid state physics, also referred to as a quantum simulator [15]. Moreover, the ability to create large lattices with only few atoms per lattice site has led to diverse proposals for quantum computing with atoms in periodic potentials as qubits [16]. For very low atomic densities in the lattice it is possible to probe two-body dynamics directly, which has revealed exotic features such as the formation of repulsively bound atom pairs [17–20].

The most notable hallmark of ultracold atom physics was the achievement of a Bose-Einstein condensate in 1995 [21, 22], for which C. E. Wieman, E. A. Cornell and W. Ketterle were awarded the Nobel Prize in 2001. In a Bose-Einstein condensate all atoms are condensed into the quantum mechanical ground state. Hence all atoms are in the same superposition of being everywhere inside the cloud, which makes the gas highly correlated. The interatomic interaction gives rise to a nonlinear term in the equation of motion reminiscent of the non-linear equation governing the dynamics of nonlinear optics. Therefore, many effects originally known from optics also have an atomic counterpart. This is the case with stimulated four-wave mixing, where two accelerated condensates, also called matter waves, because they consist of matter but behave as waves, are scattered into new matter waves in a stimulated process - stimulated in the sense that outgoing waves already present will be amplified. The outgoing atom beams will be number correlated and entangled [23–27], and this is useful in both precision measurements and quantum computing and communication.

If an optical lattice is applied to a Bose-Einstein condensate the atoms continue to be in the quantum mechanical ground state although the ground state changes provided that the lattice strength is increased sufficiently slowly. As long as the lattice is weak each atom is in the same superposition of being anywhere in the lattice as all the other atoms. But as the lattice strength increases, the ground state becomes an insulator state, where each atom is localized within a single lattice period [28–31]. Because the trapping potential is deepest in the middle of the trap the lattice site here will be occupied by more atoms than the lattice site at the edge of the trap. This results in a wedding cake structure with disks (in 2D) or spheres (in 3D) with an equal number of atoms in each lattice well and with highest filling in the center of the trap. This has been facilitated in many experiments to construct physical systems with specific number of particles in the lattices wells.

Furthermore, the interaction between atoms can be tuned by an external magnetic field due to the presence of a molecular resonance, a so-called Feshbach resonance. It is even possible to change from repulsive interaction to attractive or visa versa. The presence of a molecular resonance not only changes the interaction strength but it can also be used for controlled formation of molecules. The thus formed molecules are very weakly bound and hence lattices have been used to avoid collisions between molecules and free atoms, which would lead to collisional deexcitations with accompanying energy release that exceeds the trap depth. In addition atoms in a lattice can be more tightly confined which also may enhance conversion by increasing the

overlap between the atomic wave functions.

Our work is primarily focused on the two-body dynamics in one-dimensional optical lattices. In the literature [17, 18, 32] the method of Green's functions has been used to find and characterize the bound states of such systems in the special case of identical particles and a standard only-nearest-neighbor coupling Bose-Hubbard model. We extend this formalism to (i) include coupling to a Feshbach resonance, to (ii) mixtures of different atomic species and to (iii) go beyond the standard Bose-Hubbard model by including more than nearest-neighbor couplings. We also present both an analytical two-body and a numerical many-body analysis of the special case of non-degenerate four-wave mixing in quasi-one-dimensional lattices. The proposal was originally based on experience from fiber optics [24] and it was later demonstrated experimentally [25]. We will go beyond standard mean-field analysis, and instead use two very different approaches; the Gutzwiller approximation and the truncated-Wigner method.

1.2 Outline of the thesis

We will start out by giving an introduction to the basic concepts of an optical lattice in **chapter 2**. Most of this will be well known from introductory courses on solid state physics, but we will also provide a detailed discussion of the Wannier states and their tunneling properties, which will be important for understanding the rest of this thesis. In **chapter 3** we extend the single-particle analysis of chapter 2 to a discrete two-body model. The devised two-body model describes both the bound states and the scattering continuum analytically. This chapter will form the foundation for the following three chapters, where the model is generalized to more complicated physical systems.

In **chapter 4** we set up a two-channel framework, which allows us to incorporate a Feshbach resonance into the discrete two-body model. Based on this extended formalism we analyze the interplay between the dynamics of two asymptotically free atoms and a molecular bound state. This two-channel model is further generalized in **chapter 5** to also cover the case of different atomic species. Finally, we round off the two-body analysis by extending the model to go beyond the nearest-neighbor tunneling approximation in **chapter 6**. The latter extension will be of great importance when we study non-degenerate four-wave mixing in quasi-one-dimensional lattices, **chapter 7**. Before we can study the four-wave mixing process, we have to introduce the fundamentals of the many-body dynamics. Therefore, in this chapter we deduce the Bose-Hubbard model and two numerical techniques to solve the many-body dynamics. The numerical methods are the Gutzwiller approximation and the stochastic truncated-Wigner approach. In addition we present in **appendix B** a third method: the stochastic Gutzwiller model.

Finally, we conclude our work in **chapter 8**.

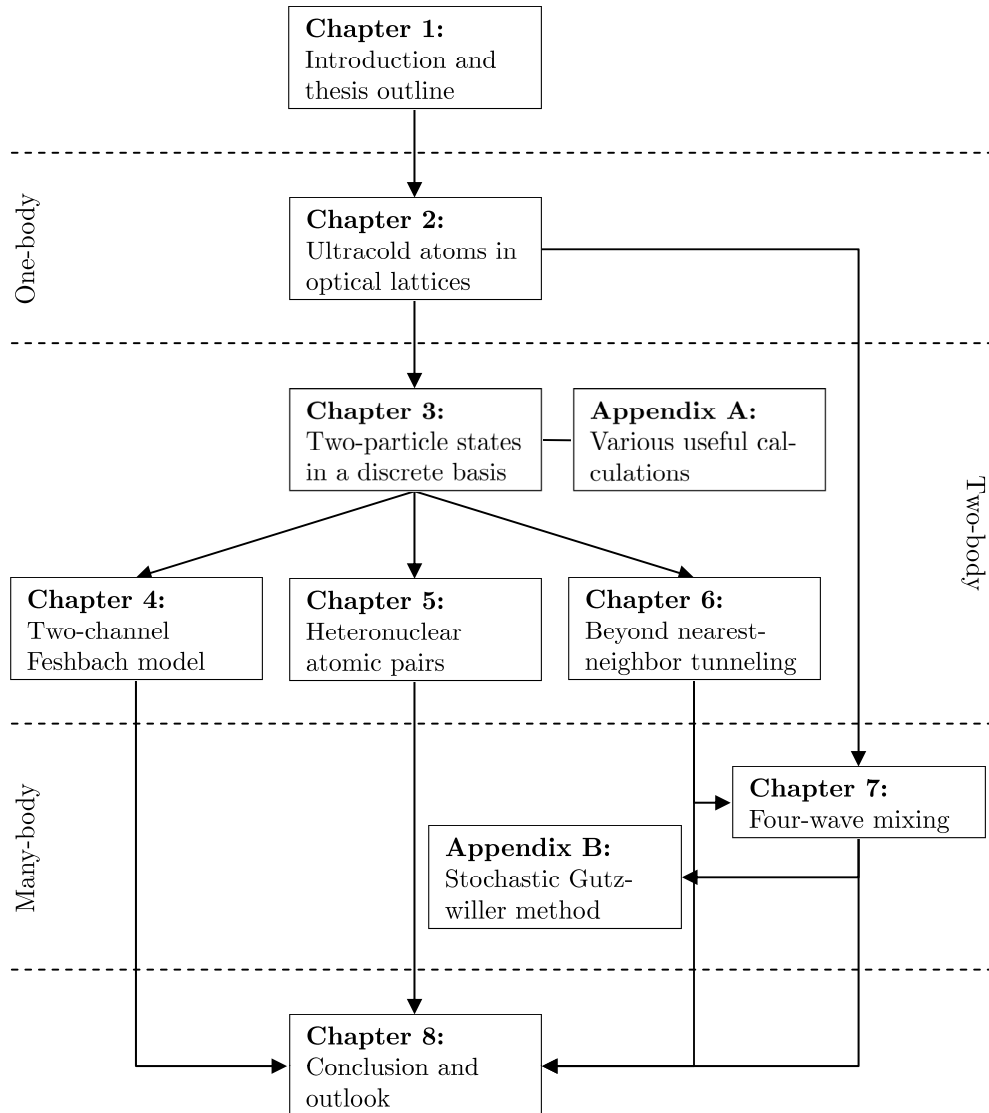


Figure 1.1: Reading guide to the thesis.

Chapter 2

Ultracold atoms in optical lattices

The ability to control almost any little detail in an optical lattice makes it a very powerful tool in cold gas experiments. In this chapter we give an introduction to periodic potentials, which will form the foundation for the rest of the thesis. A comprehensive review of cold atom physics in lattices can be found in [33, 34] and for a thorough discussion of the AC-stack shift we refer the reader to Ref. [35].

2.1 Introduction

An optical lattice is a diverse experimental device. An optical lattice is created by counterpropagating laser beams, and by aligning the lasers in various setups almost any desired geometry of the lattice can be realized [5–7]. Furthermore, the depth of a lattice along a given direction can be dynamically adjusted during an experiment simply by varying the intensity of the lasers along that direction. Furthermore, applying a deep lattice along a particular direction can prevent the atoms from moving along that direction at all, resulting in a reduce number of dimensions. In this way the dimensionality of the system can be reduced to two, one or even zero dimensions [12–14]. The results in this chapter are applicable to any cubic optical lattices, *i.e.*, lattices where the sets of lasers are aligned along the three standard axes, but in the rest of the thesis we will only consider (quasi-)one-dimensional systems with two directions “frozen out” by deep lattices and a weak lattice present along the last “free” direction.

With the advent of Bose-Einstein condensates (BEC) it has become possible to load a lattice with all atoms in the ground state. This is possible because all the atoms in a BEC are in the same quantum state, which for a condensate at rest will be the ground state, and if a lattice is adiabatically ramped up, the atoms stay in the ground state even though the ground state changes. This has, among many other things, led to the seminal demonstration of the Mott-superfluid transition: as the lattice is deepened, the atoms go

from being in the same delocalized “superfluid” state to a Mott insulator with consists of disks with equal (integer) occupation decreasing from the center to the edge of the trap. From the Mott insulator methods have been developed to remove specific regions such that one ends up with only single or double occupied lattice sites [17]. It is also possible to construct superlattices by overlaying lasers with different wavelengths. This has been used to pattern atoms into every second or third lattice site [19, 36].

Hence, it is possible not only to control the dimensionality but also where and how many atoms we have in the lattice wells. This has led to numerous suggestions for doing quantum computation in optical lattices [15, 16], but it also opens up for the study of for example the atomic two-body dynamics in reduced dimensions, as is the topic of Chapter 3–6.

Therefore, weak lattices can be used to control the dynamics of the atoms by engineering the energy dispersion. This amounts to adjusting the (effective) mass, which in the novel experiments by Paredes *et al.* [9] was used to achieve the one-dimensional Tonks-Girardeau gas, where the repulsive interaction in a Bose gas prevents the atoms from being on top of each other, forcing the bosons to act as fermions [11]. This is possible because, as the effective mass is increased, the ratio between interaction and the kinetic energy, $\gamma = I/K \propto m$, also increases. The Tonks-Girardeau gas has also been achieved by Kinoshita *et al.* [10], where they controlled the interaction strength by adjusting the transverse trapping potential, a deep 2D optical lattice. The band structure will play a key role when considering four-wave mixing in Chapter 7. It is not possible to have one-dimensional four-wave mixing in free space due to the requirement of simultaneous energy and momentum conservation, but by applying a weak periodic potential one can change the energy dispersion to allow this type of processes.

2.2 Optical lattices

An optical lattice can be created by a set of counterpropagating lasers. The lasers create a standing electromagnetic field, $\mathcal{E}(\mathbf{x}, t) = \mathcal{E}_L(\mathbf{x}) \cos(\omega_L t)$, where \mathcal{E}_L is the position dependent field strength and ω_L is the angular frequency. The time-varying field results in AC-stark shifts of the atomic energy levels, a second order perturbative effect, leading to a potential of the form

$$V(\mathbf{x}) = \frac{1}{4}\alpha_L|\mathcal{E}_L(\mathbf{x})|^2. \quad (2.1)$$

Here $\alpha_L \propto 1/(\Delta + i\Gamma)$ is the polarizability which depends on the detuning $\Delta = \omega_a - \omega_L$ of the lasers compared to the atomic transition frequency ω_a and a width parameter Γ , which can be ignored when the lasers are far off-resonant. For red detuned light ($\Delta < 0$) the potential minima are found where the laser intensity are maximal, and for blue detuned ($\Delta > 0$) the potential minima are at the intensity minima [8, 35].

We will restrict our analysis to simple cubic lattices, where three sets of counterpropagating lasers are arranged along the standard axes. In this case

an atom will experience the potential

$$V_{\text{lat}}(\mathbf{x}) = \sum_{i=1,2,3} V_0^i E_R \sin^2(\pi x_i/a). \quad (2.2)$$

Here the lattice constant $a = \lambda_L/2$ is half the laser wavelength λ_L and the lattice strength V_0^i along direction i is measured in units of the recoil energy $E_R = \hbar^2/2m\lambda_L^2$, which depends on the atomic mass m and the wavelength. The recoil energy is the kinetic energy an atom initially at rest acquires from absorption of one photon from the laser field. If A is the mass number of the atoms and k_B is the Boltzmann constant, then the recoil energy is of the order $E_R/k_B = \hbar^2\omega_L^2/2mk_Bc^2A \sim 6\mu\text{K} \cdot (\hbar\omega_L/1\text{eV})^2/A$. Therefore, we have to be in the μK regime if we want to trap the atoms in the optical lattice. In experiments V_0^i is usually varied from zero up to around 40 [17, 37].

2.3 Reduced dimensionality

For a cubic lattice the atomic motion separates along the three spatial directions and each direction can be analyzed separately. If the lattice along one direction is very deep, it can be approximated by a harmonic potential for low energies, $V_0 E_R \sin^2(\pi x/a) \sim V_0 E_R (\pi x/a)^2$. If this is the case, the eigenstates can be approximated by the harmonic oscillator states with energy $(n + \frac{1}{2})\hbar\omega$, where $n \in \mathbb{N}_0$ and $\omega = (\pi/a)\sqrt{2V_0 E_R/m}$. If the scattering energies are well below $\hbar\omega$ the atoms will be confined only to the lowest energy state, $w(x) = (m\omega/\pi\hbar)^{1/4} \exp(-m\omega x^2/2\hbar)$. In this way we can essentially “freeze out” a spacial dimension, since only the ground state of the Hamiltonian for that direction will be populated. By freezing out one, two or even three direction, one can construct two-, one- and zero-dimensional quantum gases [9, 10, 12–14].

We will now focus only on quasi-one-dimensional lattices, where also a weak lattice is present along the last direction. Weak in the sense that motion along this direction is still considerable. In this case the potential may be rewritten as

$$V_{\text{lat}}(\mathbf{x}) = \sum_{i=1,2} V_0^\perp E_R \sin^2(\pi x_i/a) + V_0^\parallel E_R \sin^2(\pi x_3/a), \quad (2.3)$$

where we will refer to $V_0^\parallel = V_0^3$ and $V_0^\perp = V_0^1 = V_0^2$ as the longitudinal and transverse lattice strength, respectively. Here $V_0^\parallel \ll V_0^\perp$. We have for simplicity assumed the lattice strength along the two transverse or “frozen out” directions to be identical. As the scattering energy is increased consecutive transverse channels open, but we shall only consider scattering at energies much smaller than the transverse level splitting, justifying the neglect of the transverse degrees of freedom as discussed above.

One has to be aware of the occurrence of confinement induced resonances. A confinement induced resonance occurs at the lower edge of the continuum

when the scattering length in free space a^{3D} and the width of the transverse confining potential $a_{\perp} = \sqrt{2}a(V_0^{\perp})^{-1/4}/\pi$ are related by $a_{\perp}/a^{3D} = 1.4603\dots$ [38–43]. The scattering length is the *one* parameter needed to characterize the atomic interactions in an ultracold atomic gas. The confinement induced resonance may, however, be avoided by not choosing the transverse confinement too tight, and for the quantitative results we present, it plays no role.

2.4 Single particle states in a periodic potential

The Hamiltonian, $\hat{\mathcal{H}} = -(\hbar^2/2m)\nabla^2 + V_{\text{lat}}(\mathbf{x})$, where $V_{\text{lat}}(\mathbf{x})$ is a three-dimensional periodic lattice like the ones in Eqs. (2.2) and (2.3), is separable with the Hamiltonian along direction i given by

$$\hat{\mathcal{H}}_0^{x_i} = -\frac{\hbar^2}{2m}\frac{\partial^2}{\partial x_i^2} + V_0^i E_R \sin^2(\pi x_i/a). \quad (2.4)$$

Bloch’s Theorem [44, 45] states that Eq. (2.4) is diagonalized by the product of a periodic function $u_{nq}(x)$ with the same periodicity as the lattice and a complex phase factor e^{iqx} . The wave functions $\phi_{nq}(x) = e^{iqx}u_{nq}(x)$ are called Bloch waves. They are indexed by the quasi-momentum q , which can be chosen in the first Brillouin zone, $(-\pi/a, \pi/a]$, and the band index $n \in \mathbb{N}$. In the absence of the lattice the energies $E_n(q)$ are the free-space energy parabola folded into the first Brillouin zone, Fig. 2.1(a), but as the lattice is ramped up, *i.e.*, V_0^i is increased, the parabola splits up into separate energy bands separated by energy gaps, Fig. 2.1(b)–(c), which arise due to the coupling of the free space momentum states by the periodic potential.

2.5 Wannier functions

The Bloch waves are delocalized, but can be unitarily transformed into orthonormal localized basis functions, the Wannier functions, which in the longitudinal direction take the form [46]

$$w_{nz_j}(x_3) = \left(\frac{a}{2\pi}\right)^{1/2} \int_{-\pi/a}^{\pi/a} dq e^{-iqz_j} \phi_{nq}(x_3). \quad (2.5)$$

In addition to the band index each Wannier function is labeled by a “quasi-position” $z_j = aj$ with $j \in \mathbb{Z}$ specifying at which lattice site the function is localized. Figure 2.2 shows Wannier functions for three different lattice strengths and the two first Bloch bands. The stronger the lattice the more localized the Wannier functions. Apart from being either even or odd functions they furthermore have the very convenient property that they are identical up to a displacement within each band:

$$w_{nz_j}(x_3) = w_{n0}(x_3 - z_j). \quad (2.6)$$

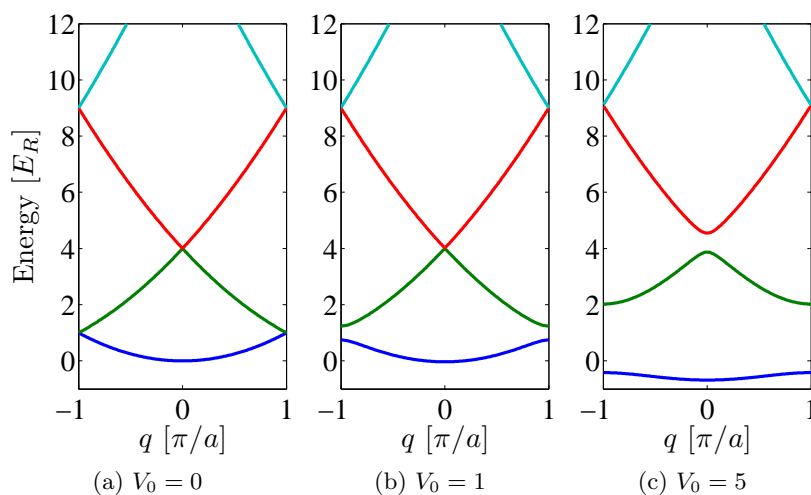


Figure 2.1: Band structure $E_n(q)$ for three different lattice strengths. From below the curves correspond to $n = 1, 2, 3$ and 4.

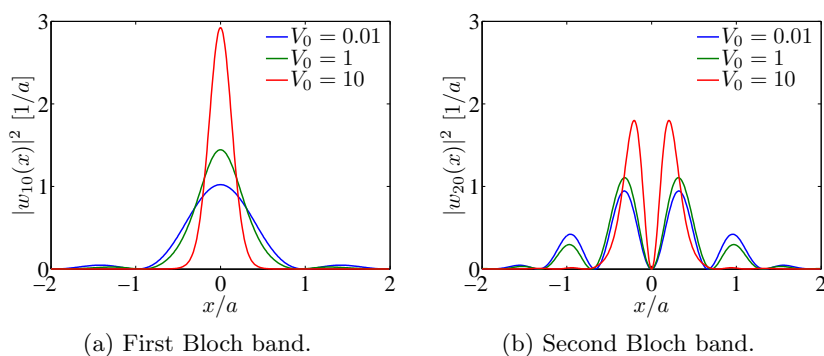


Figure 2.2: Wannier functions for different lattice strength with (a) $n = 1$ and (b) $n = 2$. Note that V_0 for the blue curve is two orders of magnitude less than the lattice strength of the green curve.

This follows directly from Eq. (2.5) and the properties of the Bloch waves.

To ensure constructive interference at the j^{th} well in Eq. (2.5), we need a phase convention on ϕ_{nq} . If n is even, we chose $\phi_{nq}(x=0)$ to be real and positive for all q and, if n is odd, we choose the gradient at $x=0$ to be real and positive. This is particularly important when constructing Wannier functions numerically.

A detailed analysis of the Wannier functions can be found in the work by Kohn [46] and He *et al.* [47]. Here it has been shown that Wannier functions asymptotically fall off as $w_{n0}(x) \sim |x|^{-3/4} \exp(-h_n|x|)$, where $h_n > 0$ is a band specific decay constant which depends on the lattice strength and decreases for higher bands. It is possible to construct more localized states, but then they are not orthogonal.

The transform in Eq. (2.5) is nothing but a Fourier transform in the q -index of the Bloch waves, and it is instructive to consider the inverse transform, $|\phi_{nq}\rangle = \sum_{z_j} \psi_q(z_j) |w_{nz_j}\rangle$, where the coefficients $\psi_q(z) = \sqrt{a/2\pi} e^{iqz}$ indeed resembles the spatial Bloch waves, but with the on-site details in $u_{nq}(x)$ absorbed into the Wannier functions. For a discussion of the normalization, see App. A.1. In the next section we proceed to describe the dynamics of the system in terms of the Wannier basis.

2.6 Tunneling amplitudes

The dynamics of a single atom in the lattice are fully characterized by the tunneling or hopping amplitudes,

$$J_{nd} \equiv -\langle w_{nz_{j+d}} | \hat{\mathcal{H}}_0 | w_{nz_j} \rangle, \quad (2.7)$$

which is minus the matrix elements of $\hat{\mathcal{H}}_0$ in the Wannier basis. This can be interpreted as the amplitude by which an atom located in the Wannier function w_{nz_j} at lattice site j is transferred to the Wannier function $w_{nz_{j+d}}$ located d sites away, as illustrated in Fig. 2.3. The amplitudes are independent of j due to the displacement property of the Wannier functions, Eq. (2.6). Note that there are no couplings between different Bloch bands, because the Wannier function w_{nz_j} is a transform of Bloch waves from the n th band only. Moreover, it should be noted that J_{nd} is a dynamical tunneling amplitude and not related to the usual concept of quantum mechanical tunneling, *i.e.*, $|J_{nd}|^2$ is not the probability of finding the atom at the neighboring lattice site.

To interpret J_{nd} in terms of the band structure, we insert the Bloch wave expansion for the Wannier functions (2.5) into the integral for J_{nd} ,

$$\begin{aligned} J_{nd} &= -\frac{a}{2\pi} \int_{-\pi/a}^{\pi/a} dq' \int_{-\pi/a}^{\pi/a} dq \int_{-\infty}^{\infty} dx \phi_{nq'}(x)^* \hat{\mathcal{H}}_0 \phi_{nq}(x) e^{iqad} \\ &= -\frac{a}{2\pi} \int_{-\pi/a}^{\pi/a} dq E_n(q) e^{iqad}. \end{aligned} \quad (2.8)$$

We observe that the J_{nd} amplitudes are the Fourier coefficients of the n th energy band. For an inversion symmetric lattice the band structure is an even

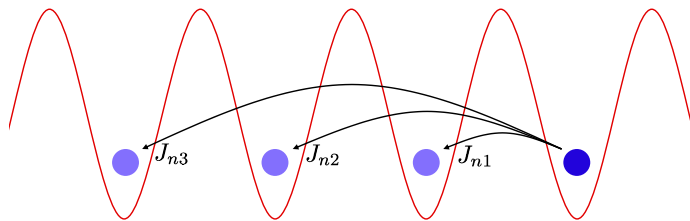


Figure 2.3: Illustration of tunneling amplitudes with $d = 1, 2,$ and 3 .

function of q , and therefore

$$E_n(q) = -J_{n0} - 2 \sum_{d>0} J_{nd} \cos(qad). \quad (2.9)$$

Note that $-J_{n0}$ is both the expectation value for $\hat{\mathcal{H}}_0$ of a Wannier state and at the same time the average energy of the n th Bloch band. As for the Wannier functions an asymptotic limit also exist for the tunneling amplitudes. It can be shown that they falls off according to $J_{nj} \sim j^{-3/2} \exp(-h_n j a)$, where h_n is the same decay constant as for the Wannier states [47].

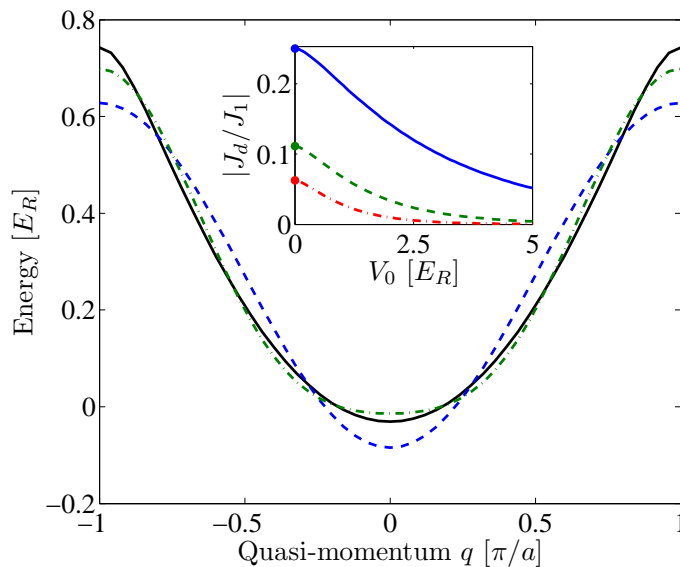


Figure 2.4: Energy spectrum of the first Bloch band for $V_0 = 1$ (black solid line). The dashed lines are the spectrum reproduced by (blue) only nearest-neighbor tunneling and (green) next-nearest neighbor tunneling. Insert: The importance of higher J_d coefficients as a function of the lattice strength V_0 . From the top it is J_2, J_3 and J_4 . The filled circles indicate the Fourier coefficients of the free-space (kinetic) energy spectrum folded into the first Brillouin zone.

In most of this thesis we restrict ourselves to the lowest band. This is reasonable, if the involved energies are well below the second energy band and that is the situation in many cold atom experiments. Under this assumption we drop the band index n and write the single-particle Hamiltonian as

$$\hat{\mathcal{H}}_0 = - \sum_j \sum_{d>0} J_d (|w_{z_j}\rangle \langle w_{z_{j+d}}| + |w_{z_{j+d}}\rangle \langle w_{z_j}|), \quad (2.10)$$

which has the energy spectrum [cf. Eq. (2.9)]:

$$E(q) = -2 \sum_{d>0} J_d \cos(qad). \quad (2.11)$$

Here J_0 is set to zero, which places zero energy in the middle of the first Bloch band. The size of the tunneling amplitudes compared to the nearest-neighbor tunneling are shown in Tab. 2.1 and Fig. 2.4. We observe that in the weak lattice limit, $V_0 \rightarrow 0$, J_d coincides with the Fourier transform of the free space energy dispersion parabola,

$$J_d = -\frac{a}{2\pi} \frac{\hbar^2}{2m} \int_{-\pi/a}^{\pi/a} dq q^2 e^{iqad} = -(-1)^d \frac{\hbar^2}{2m} \frac{1}{(ad)^2}. \quad (2.12)$$

This is indicated by filled circles in Fig. 2.4.

V_0	J_0/E_R	J_1/E_R	J_2/J_1	J_3/J_1	J_4/J_1	J_5/J_1	J_6/J_1
0	-	-	-0.25	0.11	-0.06	0.04	0.03
0.5	-0.32	0.19	-0.23	0.09	-0.05	0.03	-0.02
1.0	-0.27	0.18	-0.20	0.07	-0.03	0.01	-0.01
5.0	0.56	0.07	-0.05	0.00	-0.00	0.00	-0.00
10.0	2.12	0.02	-0.01	0.00	-0.00	0.00	-0.00

Table 2.1: Tunnel amplitudes for different lattice strengths. The first line shows the limiting values as V_0 goes to zero.

It is important to note that J_2 is not the same as making two steps with J_1 in a numerical simulation. J_2 is a proper matrix element of the lattice Hamiltonian, Eq. (2.4). We further note that in a two- or three-dimensional cubic lattice there is no diagonal tunnel amplitudes, because the Hamiltonian is separable:

$$\langle \omega_{z_{j+d_x}(x)} \omega_{z_{i+d_y}(y)} | \hat{\mathcal{H}}_0^x + \hat{\mathcal{H}}_0^y | \omega_{z_j(x)} \omega_{z_i(x)} \rangle = J_{d_x} \delta_{d_y,0} + J_{d_y} \delta_{d_x,0}. \quad (2.13)$$

Here $\hat{\mathcal{H}}_0^x$ and $\hat{\mathcal{H}}_0^y$ only involve the x and y coordinate, respectively. This is illustrated in Fig. 2.5.

The Hilbert space is now represented by a discrete basis of localized Wannier states, for which Eq. (2.10) is the discrete lattice Hamiltonian with spectrum Eq. (2.11). So far no approximations have been made except for the possible omission of the higher Bloch bands.

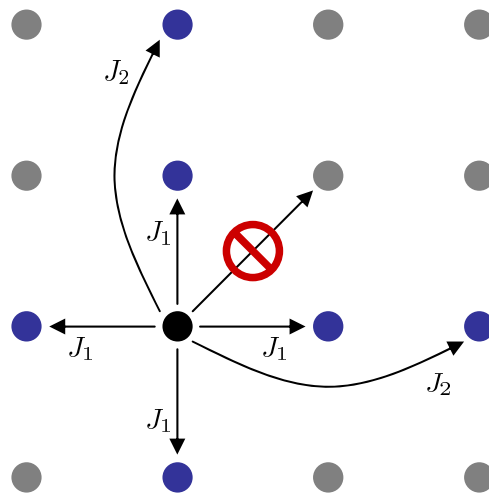


Figure 2.5: In a two-dimensional lattice there is no diagonal tunneling, see Eq. (2.13).

2.7 Nearest-neighbor approximation

It is customary to disregard tunneling between non-adjacent lattice sites assuming $|J_d| \ll J_1$ for all $d > 1$. In the basis of the Wannier states the single particle Hamiltonian for motion in the longitudinal direction then becomes

$$\hat{\mathcal{H}}_0 = - \sum_j J (|w_{1z_j}\rangle\langle w_{1z_{j+1}}| + |w_{1z_{j+1}}\rangle\langle w_{1z_j}|) \quad (2.14)$$

with $J \equiv J_1$, cf. Eq. (2.10). Equation (2.14) is for a quasi-one-dimensional problem, but it can be readily extended to situations where the transverse degrees of freedom are not frozen.

The single-particle energy spectrum, Eq. (2.11), is reduced to a simple cosine structure, $E(q) = -2J \cos(qa)$. This is not always sufficient to describe the dynamics of the system. We will show examples of this in Chap. 7. In Fig. 2.4 the true band structure is compared with the modelled dispersion when only nearest-neighbor tunneling and next-nearest-neighbor tunneling are included. Furthermore, the size of the tunneling amplitudes are shown as a function of the lattice depth. For J_2 to be less than 1% of J_1 , V_0 has to exceed $10.6E_R$ [48].

2.8 Energy dispersion derivatives

The tunneling amplitudes are related through the derivatives of the energy dispersion to the important notions of density of states, group velocity and effective mass. The connection becomes particular simple for quasi-one-dimensional lattices. The results of this section are valid for any Bloch band and for the

same reason we will omit the band index on energy dispersions and wave functions.

2.8.1 Group velocity

We start by inferring the notion of group velocity, which is the incline of the energy dispersion, $v_g(q) = E'(q)/\hbar$. It can be shown that this is nothing but the expectation value of the velocity operator \hat{p}/m (here \hat{p} is the momentum operator) for a Bloch state $|\phi_q\rangle$ [44]. It is always zero at $q = 0$ and at the zone edge $q = \pm\pi/a$, in which cases the Bloch waves are standing waves.

2.8.2 Effective mass

If we write up the acceleration as the time derivative of the group velocity, we find

$$a(q) = \frac{d}{dt}v_g(q) = \frac{1}{\hbar} \frac{d^2 E}{dq^2} \frac{dq}{dt}, \quad (2.15)$$

which indeed is reminiscent of Newton's 2nd law with $\hbar q$ playing the role of the momentum, if we define the effective mass as

$$\frac{1}{m^*} = \frac{1}{\hbar^2} \frac{d^2 E}{dq^2}. \quad (2.16)$$

The weight of the atom has not changed, but the effective mass takes the interaction with the lattice into account and is the inertia which gives the acceleration when an external force acts on the system [44, 45]. The effective mass is related to the curvature of $E(q)$ and can be both positive and negative. In the case of a negative effective mass the acceleration in (2.15) due to a force F will appear as if we acted with $-F$.

In terms of the tunneling amplitudes this quantity becomes

$$\frac{1}{m^*} = \frac{2a^2}{\hbar^2} \sum_{d>0} d^2 J_d \cos(qad). \quad (2.17)$$

For the first band it is negative near $q = \pi/a$ and positive near $q = 0$ and diverges in between, see Fig. 2.6. Furthermore, we observe that in the nearest-neighbor tunneling approximation it diverges and changes sign at $q = \pm\pi/2a$, whereas the true effective mass as given by Eq. (2.16) diverges closer to the zone boundary. As more J_d 's are included the precision of the divergence position is increased.

2.8.3 Density of states

The density of states is a measure of the number of quantum states in a given energy interval. Consider a finite one-dimensional lattice with N lattice periods, *i.e.*, of length $L = aN$, and with periodic boundary condition:

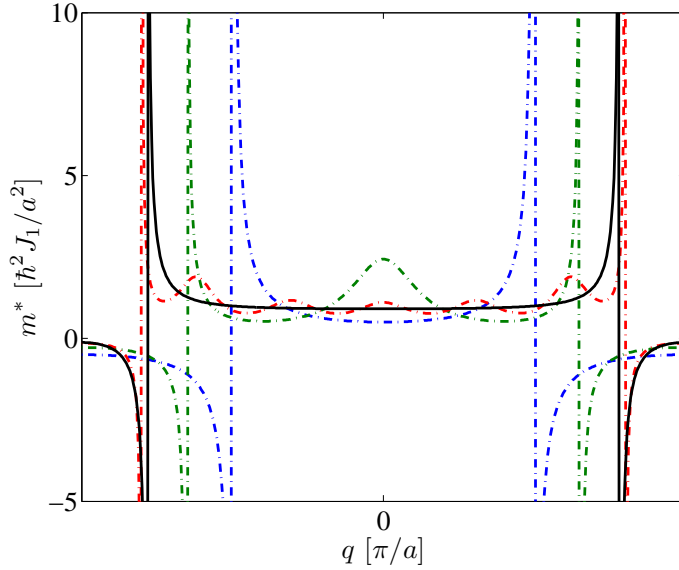


Figure 2.6: Effective mass for a single particle in the first Bloch band. The black curve is the true effective mass as given by Eq. (2.16), whereas the dot-dashed lines corresponds to inclusion of (blue) only J_1 , (green) J_1 and J_2 , and (red) J_d for $d \leq 6$.

$\phi_q(0) = \phi_q(L)$. The allowed quasi-momenta are

$$q = 0, \pm \frac{2\pi}{L}, \pm \frac{4\pi}{L}, \dots, \pm \frac{2\pi N}{L}. \quad (2.18)$$

We see that we have $\Delta q = \frac{2\pi}{L}$ length quasi-momentum space per state. From this we may determine the number of modes in the energy interval $(E, E+dE)$, which corresponds to two intervals of quasi-momentum, $(-q(E) - dq, -q(E))$ and $(q(E), q(E) + dq)$, both of length $dq = (dq/dE)dE$:

$$D_N(E)dE = 2 \frac{dq}{\Delta q} = 2 \frac{L}{2\pi} \left| \frac{dq}{dE} \right| dE. \quad (2.19)$$

Note that the front factor of two comes from the fact that $E(q)$ is symmetric and hence two-fold degenerate. Therefore, the density of states per lattice site becomes

$$D(E) = \frac{D_N(E)}{N} = \frac{a}{\pi} \frac{1}{|E'(q)|}. \quad (2.20)$$

In terms of the tunneling amplitudes this is

$$D(E) = \left| 2\pi \sum dJ_d \sin(qad) \right|^{-1} \quad (2.21)$$

or within the nearest-neighbor approximation:

$$D(E) \simeq \frac{1}{|2\pi J_1 \sin(qa)|}. \quad (2.22)$$

In both cases we note that the one-dimensional density of states diverges at the top and the bottom of the energy band. Finally, we observe that Eq. (2.20) is equivalent with the following definition of density of states

$$D(E) = \frac{a}{2\pi} \int_{-\pi/a}^{\pi/a} \delta(E - E(q)) dq. \quad (2.23)$$

2.9 Time-of-flight measurements

As already mentioned one of the great advantages of an optical lattice is the dynamical control of the depth. This can be employed to measure the wave function by means of a time-of-flight experiment. Here one turns off the lattice and let the constituents expand freely and after some time t an absorption picture is taken. In this absorption picture the particle density in the expanded gas is measured, and due to the tight confinement of the initial gas, the position of a particle is directly connected to the initial momentum via $\mathbf{x} = \mathbf{p}t/m$, where m is the mass of the particle and p is the momentum before release from the trap. Therefore, we have the relation

$$\langle \hat{n}(\mathbf{x}) \rangle_t \simeq \langle \hat{n}(\mathbf{p}) \rangle_{t=0} \quad (2.24)$$

between the expectation values of density operators \hat{n} for \mathbf{p} and \mathbf{x} before and after expansion, respectively. There will be a small deviation from Eq. (2.24) due to interactions between the particles and more importantly there will be an acceleration due to gravity along the vertical direction.

There are two schemes for time-of-flight measurements: A sudden turn off of the lattice and an adiabatic ramp down. In the adiabatic scheme each Bloch wave is mapped onto a single momentum component, *i.e.*, the energy dispersion is mapped over to the free particle dispersion. This makes it easy to measure the quasi-momentum composition of the gas. If we on the other hand turn off the lattice abruptly, we may observe a comb of momentum peaks. If we for example imagine a Bose-Einstein condensate with all atoms initially in the $q = 0$ quasi-momentum state, we will observe a comb of peaks with $p = 2\pi\hbar n/a$, $n \in \mathbb{Z}$.

If we have several atomic species or molecules in the trap, the absorption photos can be made species selective and we are granted separate information for each species. The disadvantage of the time-of-flight method is that it destroys the quantum state.

2.10 Conclusion

In this chapter we discussed how to reduce the dimensionality of a physical system by an optical lattice. We also constructed a localized basis, the Wannier functions, as a Fourier transform of eigenstates, the Bloch waves. In this new basis the dynamics of the lattice are governed by the hopping matrix elements J_{nd} and the result is a discrete model where the quantum states are

vectors with an amplitude representing each lattice site. We identified the tunneling amplitudes as both the amplitudes of being transferred between two lattice sites the distance ad apart and the Fourier amplitudes of the band dispersion $E_n(q)$. Moreover, we showed that the tunneling amplitudes are intimately connected with the effective mass and the density of states [Sec. 2.8]. The nearest-neighbor model, which will form the foundation of chapter 3–5, were discussed [Sec. 2.7] and finally, we sketched how the momentum states in the trap can be mapped out by an absorption measurement [Sec. 2.9].

Chapter 3

Two-particle states in a discrete basis

In ultracold gas physics densities are usually so low that three-body collisions can be ignored, this leaves two-body interactions as the governing mechanism for the dynamics. Furthermore, the broad palette of experimental tools available today has made experiments involving essentially only two atoms accessible [17, 19]. This is two very good reasons to investigate two-body dynamics. Moreover, the simplicity and elegance of the two-body world provides a comprehensive introduction to many-body concepts like Green's functions and spectral functions, in which almost everything can be obtained analytically.

3.1 Introduction

In this chapter we will extend the one-body dynamics of the previous chapter to two interacting particles. This is particularly interesting in the ultracold atom physics, because the densities encountered here are so low that simultaneous collisions between three and more constituents are very rare. This is because the density ρ is so low that $\rho^{-1/3}$ is much larger than the typical range of the interaction, say, the scattering length. When this is the case the interaction is mediated solely by two-body collisions, and hence the physics rely heavily on the two-body dynamics. Therefore, we will expect two-body dynamics to give important hints of where to look for interesting phenomena. This might be a prediction of a resonance or the outcome of a scattering experiment. Besides, in recent experiments two-body states have been measured in their own right. In Refs. [17, 49] a Bose-Einstein condensate is adiabatically loaded into a strong lattice to create a Mott insulator with integer filling at each lattice site. The particles at sites with more than two atoms are removed by a magnetic field sweep in which molecules are formed and particles in highly occupied sites are removed due to inelastic collisions between atoms and molecules. The singly occupied sites are blown away by a combination of a microwave and an optical field, which is off-resonant with the molecules.

Sweeping back leaves a lattice loaded with exactly zero or two atoms at each site.

We will emphasize the observation of one prominent two-body phenomenon: the formation of repulsively bound pairs. The two-body problem on a lattice features an exotic bound state in the case of repulsive interactions - as well as a less exotic bound state for attractive interaction - which was observed by measuring both the binding energy and the wave function in [17]. The tunneling properties of the bound pairs have also recently been measured [19, 50]. Repulsively bound states are expected to appear in as diverse areas as the outer electrons in benzene, interacting solitons in a periodic potential and many other places [18, 51], but in optical lattices these states have an extremely long lifetime, which means we can measure both the wave functions and the binding energy. The long lifetime of the repulsively bound pairs is intimately connected with the absence of dissipation channels, which is a distinct feature of optical lattices and in sharp contrast to solid state physics, where coupling to phonons is always possible.

Furthermore, the two-body dynamics can change the statistics by the formation of pairs, *e.g.*, if two fermions pair up to become a bosonic molecule [50]. In the case of indistinguishable fermions the formation of cooper pairs has been studied intensively, also in connection with the two-body approach followed in this work [52]. Finally, there is the interplay with Feshbach physics, where molecules may be formed by scanning an applied magnetic field. We will return to this subject in the next chapter.

We focus on quasi-one-dimensional lattices, where the two transverse degrees of freedom are “frozen out” by a deep lattice. This is a particularly interesting regime, because it is experimentally feasible and theoretically tractable, *i.e.*, we can give analytical predictions for almost everything. But also because many physical systems are naturally quasi-one-dimensional lattices, like a free electron on a polymer or in a nanowire [53, 54].

3.2 Noninteracting particles

We will assume that we have two identical particles in a quasi-one-dimensional cubic lattice, as in Eq. (2.3). The tunneling amplitudes and Wannier functions will be the same for both particles. We will think of the two particles as distinguishable, although most results are indeed still meaningful in the indistinguishable particle case [see Sec. 3.5.2 below].

If we label the atoms A and B , the two-body longitudinal wave function can be expanded on a complete basis of Wannier product wave functions as follows,

$$\Psi(x_A, x_B) = \sum_{z_A, z_B} \psi(z_A, z_B) w_{1z_A}(x_A) w_{1z_B}(x_B), \quad (3.1)$$

where $\psi(z_A, z_B)$ is the discrete wave function in the Wannier product basis. It is the amplitude of finding atom A and atom B in the Wannier functions centered at the discrete sites z_A and z_B , respectively.

In this basis the two-body noninteracting Hamiltonian becomes

$$H_0 = -J(\Delta_{z_A} + 2) - J(\Delta_{z_B} + 2), \quad (3.2)$$

where $\Delta_z f(z) = f(z+a) + f(z-a) - 2f(z)$ is the discrete Laplacian. This is seen by applying the Hamiltonian, Eq. (2.14), to Eq. (3.1) (a detailed calculation is provided in App. A.2). Here we have assumed that only nearest-neighbor tunneling is significant.

The eigenstates of H_0 are products of Bloch waves (for a discussion of the normalization, see App. A.1)

$$\psi(z_A, z_B) = \frac{a}{2\pi} \exp(iq_A z_A) \exp(iq_B z_B) \quad (3.3)$$

with quasi-momenta q_A and q_B , and energy spectrum

$$\epsilon(q_A, q_B) = E(q_A) + E(q_B). \quad (3.4)$$

Here $E(q_\beta) = -2J \cos(q_\beta a)$ is the single particle energy dispersion, where the zero of energy has been chosen to be in the middle of the first Bloch band. It should be emphasized that, while $z_{A,B}$ are discrete, the quasi-momentum $q_{A,B} \in]-\pi/a, \pi/a]$ is continuous.

To analyze the motion of the two particles in the lattice we change to center-of-mass, $Z = (z_A + z_B)/2$, and relative, $z = z_A - z_B$, coordinates and introduce the corresponding quasi-momenta $K = q_A + q_B$ and $k = (q_A - q_B)/2$, respectively. For the center-of-mass motion a plane-wave Ansatz,

$$\psi(z_A, z_B) = \sqrt{\frac{a}{2\pi}} e^{iKZ} \psi_K(z), \quad (3.5)$$

is possible, where the first Brillouin zone for the center-of-mass quasi-momentum, K , runs from $-\pi/a$ to π/a . For a discussion of the normalization, see App. A.1. Note that the problem of particles moving in the full periodic potential does not separate into center-of-mass and relative (continuous) coordinates, but in the discrete model, where both the potential and the kinetic energy are built into the tunneling coefficients and the Wannier functions, the separation *is* possible. By applying H_0 to the product Ansatz we get $H_0 e^{iKZ} \psi_K(z) = e^{iKZ} H_K^0 \psi_K(z)$, where H_K^0 is the action of the Hamiltonian H_0 on the relative coordinate wave function, ψ_K , given by

$$H_K^0 = \frac{1}{2} E_K (\Delta_z + 2), \quad (3.6)$$

where

$$E_K = -4J \cos(Ka/2) \quad (3.7)$$

is the center-of-mass energy. Hence, for each value of K we have to solve the one-body Schrödinger equation for the relative coordinate. For the eigenfunctions of H_0 , Eq. (3.3), the relative coordinate wave functions

$$\psi_K(z) = \langle z|k \rangle = \sqrt{a/2\pi} \exp(ikz) \quad (3.8)$$

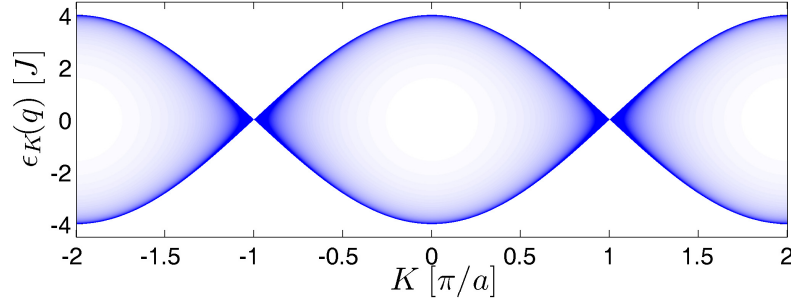


Figure 3.1: The continuum of first Bloch band in an extended zone scheme. The different shades of blue indicate the density of states with darker regions corresponding to a higher density of states. Note that the density of states diverges at the continuum boundaries.

are discrete plane waves. The corresponding energies, $H_K^0 \psi_K(z) = \epsilon_K(k) \psi_K(z)$,

$$\epsilon_K(k) = E_K \cos(ka) \quad (3.9)$$

are the sum of the single-particle energies $E(q_A)$ and $E(q_B)$:

$$\epsilon_K(k) = -2J[\cos(Ka/2 + ka) + \cos(Ka/2 - ka)].$$

It follows that the first Bloch band continuum lies between $\pm|E_K|$, where the bottom (top) corresponds to $k = 0$ ($k = \pm\pi/a$). Furthermore, the spectrum is completely degenerate at $K = \pm\pi/a$ where $E_K = 0$. We will see in Chap. 6 that this is an artifact of the nearest-neighbor approximation. The continuum is shown in Fig. 3.1, where the density of states are indicated by the different shades of blue. The density of states (per lattice site) can be obtained from Eq. (2.20) and is

$$D_K(E) = \frac{1}{\pi \sqrt{E_K^2 - E^2}}, \quad (|E| \leq |E_K|) \quad (3.10)$$

inside the continuum and zero elsewhere. This is the density of states for the Hamiltonian H_K , *i.e.*, for a fixed K , and is per lattice site as discussed in Sec. 2.8.3. We see from Eq. (3.10) that the density of states diverges at the continuum boundaries. This is a signature of the reduced dimensionality, whereas $D(E)$ is continuous and bounded in three-dimensional lattices [32]. We note that although singular the integral over the density of states per lattice site exist and is unity, $\int_{-\infty}^{\infty} dE D_K(E) = 1$. This agrees with the density of states in a finite lattice, where there is one state per lattice period (and per Bloch band).

3.3 Interaction potential

The interaction potential for neutral atoms depends only on the interatomic separation, r , and it is composed of a long range van der Waals attraction, $V(r) \sim -C_6 r^{-6}$ ($r \rightarrow \infty$), and a repulsive core. Here C_6 is the van der Waals coefficient, which depends on the atomic species. For low energy scattering the interaction is fully characterized by the s -wave scattering length $a_{\text{bg}}^{3\text{D}}$ (except for identical fermions where the s -wave scattering is suppressed and one needs the p -wave scattering length), and we can replace the interaction potential by a pseudopotential which only has to reproduce the correct scattering length. This is possible because the atoms never come close enough to feel the details of the repulsive core. The scattering length can be measured experimentally and is typical of the order of $100a_B \sim 10$ nm for alkali atoms. We will use the “zero-range” potential $V(r) = g_{\text{bg}}\delta(r)$ as our pseudopotential [55] with coupling strength $g_{\text{bg}} = 2\pi\hbar^2 a_{\text{bg}}^{3\text{D}}/\mu$, where $\mu = m_A m_B / (m_A + m_B)$ is the reduced mass, which in the case of equal masses is just half the atomic mass; $\mu = m/2$.

The range of the “real” potential (~ 10 nm) is small compared to the lattice spacing ($a \sim 400 - 500$ nm), therefore we neglect interaction between atoms located at different lattice sites and take the interaction \hat{U} to be purely “on-site” with matrix element

$$U = \langle w_{10}(\mathbf{x}'_A)w_{10}(\mathbf{x}'_B) | \hat{U} | w_{10}(\mathbf{x}_A)w_{10}(\mathbf{x}_B) \rangle \\ = g_{\text{bg}} \prod_{i=1,2} \int dx_i [w_{10}^\perp(x_i)]^4 \times \int dx_i [w_{10}^\perp(x_i)]^4. \quad (3.11)$$

Here $\mathbf{x} = (x_1, x_2, x_3)$ and $w_{10}(\mathbf{x}) = w_{10}^\perp(x_1)w_{10}^\perp(x_2)w_{10}^\parallel(x_3)$. This approximation relies on the Wannier functions being sufficiently localized, which depends on the lattice strength. A more detailed discussion of the validity will follow in Sec. 6.3.

Including the interaction the relative motion of two atoms is then described by the Hamiltonian,

$$H = H_0 + U\delta_{z,0}. \quad (3.12)$$

The separation, Eq. (3.5), in center-of-mass and relative coordinates is still pertinent, since the different K -states are not coupled by H .

As in normal scattering theory, the continuum part of H and H_0 are unitarily equivalent, therefore the continuum spectrum and density of states in the presence of interaction are identical to their noninteracting counterparts [56].

3.4 Green’s functions

We will now introduce the Green’s function formalism, from which we will extract information about both the scattering and bound states. The (retarded) Green’s function for noninteracting atoms on the lattice is defined as

$$\hat{G}_K^0(E) = [E - H_0 + i\eta]^{-1}, \quad (3.13)$$

where η is a positive infinitesimal added to enforce outgoing boundary conditions (see discussion of the Lippmann-Schwinger equation in Sec. 3.5). In momentum space it is diagonal

$$\mathcal{G}_K^0(E, k, k') \equiv \langle k | \hat{G}_K^0(E) | k' \rangle = \frac{\delta(k - k')}{E - \epsilon_K(k) + i\eta}, \quad (3.14)$$

while its coordinate space form, $G_K^0(E, z = z_2 - z_1) \equiv \langle z_2 | \hat{G}_K^0(E) | z_1 \rangle = \langle z | \hat{G}_K^0(E) | 0 \rangle$, may be found from the following integral

$$G_K^0(E, z) = \int_{-\pi/a}^{\pi/a} \frac{dk}{2\pi} \frac{ae^{ikz}}{E - \epsilon_K(k) + i\eta}. \quad (3.15)$$

It only depends on the difference, z , in the two relative coordinates z_1 and z_2 , because of the translation invariance of H_K . For energies inside the band ($|E| < |E_K|$) the solution is propagating

$$G_K^0(E, z) = -\frac{i \exp(ip|z|)}{\sqrt{E_K^2 - E^2}}, \quad (3.16)$$

with $pa = \cos^{-1}(E/E_K)$, while the solution outside the band ($|E| > |E_K|$) falls off exponentially:

$$G_K^0(E, z) = \text{sgn}(E) \frac{\exp(-\kappa|z|)}{\sqrt{E^2 - E_K^2}} [-\text{sgn}(E)]^{z/a}. \quad (3.17)$$

Here $\kappa a = \cosh^{-1} |E/E_K|$. Note that for energies above the band the sign of $G_K^0(E, z)$ alternates between lattice sites. The integral (3.15) has been solved by the method of contour integrals, see App. A.3.

3.4.1 Useful relations for the Green's function

It is instructive to apply the Sokhotsky-Weierstrass theorem

$$\int_{-\infty}^{\infty} dx \frac{f(x)}{x - x_0 \pm i\eta} = \mathcal{P} \int_{-\infty}^{\infty} dx \frac{f(x)}{x - x_0} \mp i\pi f(x_0), \quad (3.18)$$

where \mathcal{P} denotes the Cauchy principal value, to $G_K^0(E, z = 0)$:

$$G_K^0(E, 0) = \mathcal{P} \int_{-\infty}^{\infty} \frac{D_K(E')}{E - E'} dE' - i\pi D_K(E). \quad (3.19)$$

Here the integration variable has been changed from k to E . The integral in (3.19) is a Hilbert transform of the density of state. Because $D_K(E)$ is strictly positive and even for $|E| \leq |E_K|$, it hence follows that the Hilbert transform is real and continuous, except for the continuum edges, and is a decreasing function when $|E| \geq |E_K|$. It follows that the imaginary part of

the Green's is proportional to the density of states, $\text{Im } G_K^0(E, 0) = -\pi D_K(E)$, which is a general property of the trace of a single-particle Green's function. We can also derive the well known relations

$$\text{Re } G_K^0(E, 0) = -\frac{1}{\pi} \mathcal{P} \int_{-\infty}^{\infty} \frac{\text{Im } G_K^0(E', 0)}{E - E'} dE' \quad (3.20)$$

from Eq. (3.19).

Comparing Eqs. (3.19) and (3.16) we see that the Hilbert transform is zero for energies inside the continuum, and hence $G_K^0(E, 0) = -i\pi D_K(E)$. Outside the continuum the density of states is zero and therefore we are left with the Hilbert transform, which is odd in E and strictly decaying as $|E|$ increase - in agreement with the findings in Eq. (3.17).

3.4.2 Interacting pairs

The full Green's function including the interaction \hat{U} is found by explicitly solving the Dyson equation

$$\hat{G}_K^U(E) = \hat{G}_K^0(E) + \hat{G}_K^0(E) \hat{U} \hat{G}_K^U(E). \quad (3.21)$$

The result is

$$G_K^U(E; z, z') = G_K^0(E, z - z') + \frac{G_K^0(E, z) U G_K^0(E, -z')}{1 - U G_K^0(E, 0)}, \quad (3.22)$$

where we have used that the unperturbed Green's function is translationally invariant. It is the propagator from one relative coordinate in the lattice, z' , to another, z . The expression for $G_K^U(E, z, z')$ reduces to the simple result

$$G_K^U(E, z) = \frac{G_K^0(E, z)}{1 - U G_K^0(E, 0)}. \quad (3.23)$$

when either z or z' are equal to zero. Defining the diagonal elements of the noninteracting momentum space Green's function to be

$$\mathcal{G}_K^0(E, k) = [E - \epsilon_K(k)]^{-1} \quad (3.24)$$

the full Green's function has the momentum space form

$$G_K^U(E, k, k') = \mathcal{G}_K^0(E, k) \delta(k' - k') + \frac{a}{2\pi} \frac{U \mathcal{G}_K^0(E, k) \mathcal{G}_K^0(E, k')}{1 - U G_K^0(E, 0)}, \quad (3.25)$$

which follows from the matrix elements of Eq. (3.21) in the relative momentum eigenbasis, using that for an on-site interaction the matrix element, $\langle k | \hat{U} | k' \rangle = U a / 2\pi$, is constant for all (k, k') .

3.5 Scattering properties

With the expressions for the Green's functions the formal solution of the Schrödinger equation for the relative motion becomes explicit. This allows us to identify the transmission probability for collisions and analyze the near threshold scattering in terms of a generalized scattering length. This section introduces the concepts and quantities central to the ensuing discussion of two-channel scattering in Chapter 4. We first present results relevant to scattering of distinguishable particles, and then discuss how to treat the case of indistinguishable bosons or fermions.

3.5.1 Transmission profile

Choosing the situation with the incident wave entering from the left with quasi-momentum $pa = \cos^{-1}(E/E_K)$, the scattering state of two particles colliding under the influence of the interaction, \hat{U} , is given by the solution of the Lippmann-Schwinger equation

$$|\psi^\pm\rangle = |\phi\rangle + \frac{1}{E - H_0 \pm i\eta} \hat{U} |\psi^\pm\rangle, \quad (3.26)$$

where $\langle z|\phi\rangle = \exp(ipz)$ is the unperturbed incoming wave, Eq. (3.8), and the sign on the infinitesimal η determines the boundary conditions, *i.e.*, whether the scattered component is outgoing (+) or incoming (-). We will only be interested in the outgoing solution. Note that we have dropped the normalization factor $\sqrt{a/2\pi}$ on the unperturbed wave for simplicity, this means that all the scattering waves in this section is measured in units of $\sqrt{a/2\pi}$. In the z -basis Eq. (3.26) becomes

$$\psi_K^{\text{bg}}(E, z) = e^{ipz} + \sum_{z', z''} \langle z|\hat{G}_K^0(E)|z'\rangle \langle z'|\hat{U}|z''\rangle \psi_K^{\text{bg}}(E, z''). \quad (3.27)$$

For our on-site interaction of strength, U , the scattering wave function reduces to

$$\psi_K^{\text{bg}}(E, z) = e^{ipz} + UG_K^U(E, 0)e^{ip|z|}, \quad (3.28)$$

where we have used that $G_K^U(E, z) = G_K^U(E, 0)e^{ip|z|}$. We note that for the contact potential, $\psi_K^{\text{bg}}(E, z)$ equals its asymptotic form

$$\psi_E^{\text{bg}}(z) \xrightarrow{|z| \rightarrow \infty} e^{ipz} + f_{\text{bg}}^{\text{even}}(E, K)e^{ip|z|} + \text{sgn}(z)f_{\text{bg}}^{\text{odd}}(E, K)e^{ip|z|} \quad (3.29)$$

everywhere, hence we may readily identify the scattering amplitudes for the background interaction:

$$f_{\text{bg}}(E, K) \equiv f_{\text{bg}}^{\text{even}}(E, K) = \frac{UG_K^0(E, 0)}{1 - UG_K^0(E, 0)}, \quad f_{\text{bg}}^{\text{odd}}(E, K) = 0. \quad (3.30)$$

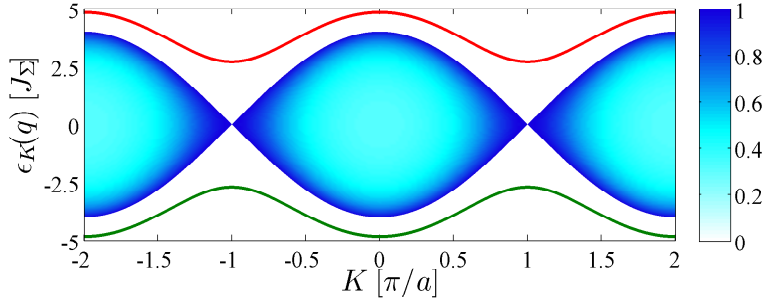


Figure 3.2: Reflection probability for $|U| = 2.7J$. The red and green curve are the bound state spectrum for $U = 2.7J$ and $U = -2.7J$, respectively (see Sec. 3.6).

They are unit-less in a one-dimensional system. The two partial waves correspond to even or odd parity, and for a delta-function interaction there is no coupling to the odd-parity partial wave, because it has no amplitude at $z = 0$. This is in agreement with the findings in Ref. [38]. For a one-dimensional problem with distinguishable particles it is natural to recast this in terms of transmission and reflection amplitudes. These are defined from the left and right asymptotic form of the wave function

$$\psi_K^{\text{bg}}(E, z) = \begin{cases} t_{\text{bg}}(E, K)e^{ipz} & z \rightarrow \infty \\ e^{ipz} + r_{\text{bg}}(E, K)e^{-ipz} & z \rightarrow -\infty \end{cases}. \quad (3.31)$$

By comparing with Eq. (3.29) it follows that the transmission amplitude is $t_{\text{bg}} = 1 + f_{\text{bg}}$, while the reflection amplitude coincides with the scattering amplitude, $r_{\text{bg}} = f_{\text{bg}}$. The resulting transmission probability is

$$T_{\text{bg}}(E, K) = |t_{\text{bg}}(E, K)|^2 = \frac{E_K^2 - E^2}{E_K^2 + U^2 - E^2}. \quad (3.32)$$

As one might expect, the transmission vanishes in the limit where $|U| \rightarrow \infty$, and approaches unity as the strength of the on-site interaction is diminished. As usual, the reflection coefficient is $R_{\text{bg}} = |r_{\text{bg}}|^2 = 1 - T_{\text{bg}}$, which is unity at the edges of the band, where propagation ceases. The minimum value of the reflection probability, $U^2/(E_K^2 + U^2)$, is attained in the middle of the band, $E = 0$. The reflection probability is plotted in Fig. 3.2 for $U = \pm 2.7J$. We emphasize that the transmission is independent of the sign of the interaction. This is a special property of the delta-function potential [57].

As usual the scattering amplitude may also be related to the phase shift, δ_{bg} , of the scattered wave. In one dimension the relation is [58]

$$f_{\text{bg}}(E, K) = \frac{1}{2} \left(e^{2i\delta_{\text{bg}}(E, K)} - 1 \right). \quad (3.33)$$

In general there will be both an even and an odd phase shift, but it follows from Eq. (3.29) that the odd partial wave is absent for the delta-function interaction. The reflection and transmission probabilities are given by

$$R_{\text{bg}} = \sin^2(\delta_{\text{bg}}) \quad \text{and} \quad T_{\text{bg}} = \cos^2(\delta_{\text{bg}}), \quad (3.34)$$

respectively. Since the reflection coefficient is one at the continuum boundary, it follows that $\delta_{\text{bg}}(E, K)$ has to be an odd multiple of $\pi/2$ both at the lower *and* at the upper edge of the continuum. For the lower edge this is in agreement with the findings in Ref. [59].

3.5.2 Identical particles

The preceding derivation of the one-dimensional scattering in the lattice assumed that the two colliding atoms are distinguishable. If the collision involves identical bosons or fermions the scattering state ψ_K^{bg} must be an even or an odd function of the separation z , respectively, to make the wave function either symmetric or anti-symmetric under interchange of the two atoms. For fermionic atoms in the same internal state this implies that the wave function vanishes for $z = 0$ and the contact interaction, $U(z) = U\delta z, 0$, does not produce any scattering. Even if it did, we would have to reconsider how to calculate the interaction strength, because the present method is built upon the s -wave scattering length.

For identical bosons the properly symmetrized scattering state may be written as

$$\psi_K^{\text{bg}}(E, z) = e^{-ip|z|} + e^{2i\delta_{\text{bg}}} e^{ip|z|}. \quad (3.35)$$

When identical particles collide in one dimension the transmission and reflection coefficients have no meaning, since the incoming and outgoing fluxes are identical, however the scattered wave still experiences a phase shift given by Eq. (3.33). Even though the transmission profile calculated above does not play a role in the scattering of identical bosons, it may nonetheless be mapped out spectroscopically. Consider transitions from a deeper bound state $|i\rangle$ in the molecule to an energy eigenstate inside the band induced by applied photodissociation fields, which are described by some transition operator \hat{T} . If the initial state is well localized with respect to the lattice spacing, such dissociative transitions to the state (3.35) occur with a probability

$$|\langle \psi_K^{\text{bg}}(E) | \hat{T} | i \rangle|^2 \propto |\psi_K^{\text{bg}}(E, z=0)|^2 = T(E, K). \quad (3.36)$$

This is a general result which is also valid for distinguishable particles.

3.5.3 Scattering length

When the relative quasi-momentum approaches the center or the edges of the Brillouin zone, the two-particle energies $\epsilon_K(k)$ tend to $\pm|E_K|$ and the scattering amplitude attains a limiting form

$$f_{\text{bg}}(E, K) \rightarrow -\frac{1}{1 - i\kappa a|E_K|/U} \quad \text{for } \kappa \rightarrow 0, \quad (3.37)$$

with $\kappa = k$ at the bottom of the band and $\kappa = \pm\pi/a - k$ at the top of the band. These limits allow a natural definition of a generalized *one-dimensional* scattering length in the lattice

$$a_{\text{bg}}(K) = -\frac{a|E_K|}{U}, \quad (3.38)$$

from the limit $f_{\text{bg}} \rightarrow -[1 + i\kappa a_{\text{bg}}]^{-1}$ of the scattering amplitude as $\kappa \rightarrow 0$ [38]. We can rewrite the scattering amplitude (3.33) as $f_{\text{bg}} = -[i \cot \delta_{\text{bg}} + 1]^{-1}$, where in the $k \rightarrow 0$ limit we have

$$\cot \delta_{\text{bg}}(k) \simeq \cot \delta_{\text{bg}}(0) - \frac{\delta'_{\text{bg}}(0)k}{\sin^2 \delta_{\text{bg}}(0)} = -\delta'_{\text{bg}}(0)k, \quad (3.39)$$

and likewise in the $k \rightarrow \pm\pi/2$ limit, $\cot \delta_{\text{bg}}(k) \simeq -\delta'_{\text{bg}}(\pm\pi/2)(k \mp \pi/2)$. In both cases we have used that δ_{bg} approaches an odd multiple of $\pi/2$ at the continuum boundaries. Therefore, an equivalent definition of the scattering length is through the derivative of the phase shift with respect to the relative momentum

$$a_{\text{bg}} = -\lim_{\kappa \rightarrow 0} \frac{\partial \delta_{\text{bg}}(k, K)}{\partial \kappa}, \quad (3.40)$$

in analogy with the usual free space scattering in three dimensions [60]. Our one-dimensional lattice scattering length is a generalization of the usual concept, in that it is defined for collision energies at both the lower *and* the upper edge of the continuum. The sign of a_{bg} at the upper edge of the continuum is a convention, which will be justified for the two-channel analysis in Chapter 4. Our generalized scattering length depends on the center-of-mass motion of the pair, which is a crucial feature in the lattice.

For $U < 0$ a bound state is situated below the continuum, making a_{bg} positive as expected. In this case the pole of the scattering amplitude, Eq. (3.37), lies along the positive imaginary axis, $k = i|U|/a|E_K|$, and the analytic continuation of the plane wave $\exp(ik|z|)$ is the dying exponential of the bound state. Conversely, for a repulsive pair of atoms, $U > 0$, the scattering length a_{bg} is negative. The pole of the scattering amplitude is then located at $k = \pm\pi/a + iU/a|E_K|$, corresponding to a wave function decaying exponentially with the separation between the two atoms and a phase factor $\exp(\pm i\pi|z|/a)$, which alternates between 1 and -1 from one lattice site to the next, in accordance with the behavior of the Green's function for the relative motion at $E > |E_K|$, Eq. (3.17).

As $|U| \rightarrow 0$ the scattering length diverges, and the bound state approaches the edge of the continuum (see Sec. 3.6). Our intuition from scattering theory in three dimensions about the relation between weakly bound states and the scattering length thus holds both below and above the continuum band. However, since U is proportional to the free space background scattering length, $a_{3\text{D}}$, the generalized one-dimensional scattering length and its three-dimensional equivalent are inversely related [38].

3.6 Bound states

The bound states of the system can be obtained as the poles of either the full Green's function (3.23) or the scattering amplitude (3.30), which amounts to the same:

$$1 = UG_K^0(E_b, z = 0). \quad (3.41)$$

It is easy to verify that

$$E_b = \text{sgn}(U)\sqrt{U^2 + E_K^2}. \quad (3.42)$$

It is a peculiar feature, that periodic potentials apparently support bound states even for *repulsive* interaction. We will address this subject in details in Sec.xx, but first we will discuss features common for both attractive and repulsive interactions. We start by noting that the bound state energies has the same sign as U , but besides that the bound state energies corresponding to $\pm U$ are symmetric around the continuum. As a special case the binding energy for $K = \pi/a$ is $E_b = U$. The binding energy is plotted in Fig. 3.2. Poles of Green's functions can in general be complex, giving rise to a so-called quasi-particle with finite lifetime, but we get only real poles, which means truly bound states.

In the limit of weak interaction the *binding* energy, *i.e.*, the separation of the bound state from the continuum band edge, $E_{\text{bind}} = E_b - \text{sgn}(E_b)|E_K|$, takes the limiting form

$$E_{\text{bind}} \sim \text{sgn}(U)\frac{U^2}{|E_K|} = -\frac{\hbar^2}{2\mu_K^*(a_{\text{bg}})^2}. \quad (3.43)$$

Here we have introduced the effective *reduced* mass of the relative motion

$$\mu_K^* \equiv \hbar^2 \left(\frac{\partial^2 \epsilon_K}{\partial k^2} \right)^{-1}, \quad (3.44)$$

for an atom pair with center-of-mass quasi-momentum K in the lattice. In Eq. (3.43) it is the limits of the effective reduced mass at the top and the bottom of the band $\mp \hbar^2/|E_K|a^2$, which is used, with the upper (lower) sign applying for $k \rightarrow \pm\pi/a$ ($k \rightarrow 0$). These limits are plotted in Fig. 3.3 as a function of K . As the center-of-mass quasi-momentum approaches the zone boundary the effective reduced mass diverges for both curves because $q_A, q_B \rightarrow \pi/2a$ and hence the effective mass of the individual atoms diverges, see Sec. 2.8.2. The approximate expression for the binding energy (3.43) is of the universal form for a bound state near continuum threshold and it approaches the correct value as $a_{\text{bg}} \rightarrow \pm\infty$.

3.6.1 Pair tunneling

The bound state pairs can tunnel together through the lattice with an effective tunneling rate, which depends on their binding energy. We now determine the tunneling matrix element of the pairs directly from their dispersion relation.

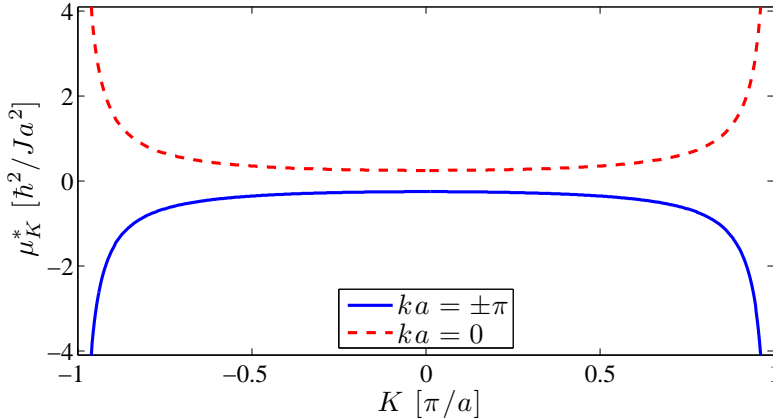


Figure 3.3: The effective mass at the upper band edge (solid line) and the lower band edge (dashed line) as a function of the center-of-mass quasi-momentum.

For weak tunneling rates the energies of the bound states are approximately given by

$$E_b \simeq U + \frac{4J^2}{U} \cos^2\left(\frac{Ka}{2}\right) \quad (3.45)$$

Comparing the momentum dependent part of the bound state energy with $E_{\text{pair}} = -2J_{\text{pair}} \cos(Ka)$, we can identify the effective tunneling rate

$$J_{\text{pair}} = -\frac{2J^2}{U}. \quad (3.46)$$

This is also what one would expect from arguments based on second order perturbation theory [61–65]. It is a peculiarity that the sign is determined by U instead of J . Recall that the sign of J_{pair} determines whether the bound pair dispersion looks as if it is “smiling” or “sad”, see Fig. 3.2. We emphasize that Eq. (3.46) only works when $|J| \ll |U|$; as U approaches zero $J_{\text{pair}} \simeq 2|J|\text{sgn}(U)$. The general expression for the tunneling amplitudes can be found as a Fourier expansion of E_b but is complicated and involves Elliptic integrals. Cooperative tunneling of atom pairs consistent with an effective pair hopping matrix element given by J_{pair} has been demonstrated experimentally by measurement of the frequency of population transfer in a double well [19] and by demonstrating that the transport properties of an attractive Fermi gas in an optical lattice depends strongly on the formation of local pairs [50].

3.6.2 Bound state wave functions

We recall that the Green’s function is defined as the resolvent of the Hamiltonian, Eq. (3.13), and therefore $(E - H_0)G_K^0(E, z) = \delta_{z,0}$. Using this and Eq. (3.41) we can rewrite the Schrödinger equation for the bound state

$$(E_b - H_0)G_K^0(E_b, z) = U\delta_{z,0}G_K^0(E_b, z). \quad (3.47)$$

This shows that $G_K^0(E_b, z)$, Eq. (3.23), is itself the solution to the Schrödinger equation with energy E_b , *i.e.*, it provides directly the bound-state wave function $\psi_K^b(z)$ except from the normalisation. Using the “geometric” series $\sum_{z \in \mathbb{Z}} e^{-2\kappa|z|} = E_b G_K^0(E_b, 0)$, the normalized states are easily computed

$$\psi_K^b(z) = \sqrt{\frac{U}{E_b}} e^{-\kappa|z|} [-\text{sgn}(E_b)]^{z/a}. \quad (3.48)$$

The solution in terms of the Green’s functions is only strictly valid for $K \neq \pi/a$ where $\kappa a = \cosh^{-1} |E_b/E_K|$ is well defined. However, the limit $K \rightarrow \pi/a$ converges to the correct solution, namely a delta-function, *i.e.*, $\psi_K^b(z) = \delta_{z,0}$. The wave function for both repulsively and attractively bound pairs is shown for different values of K in Fig. 3.4.

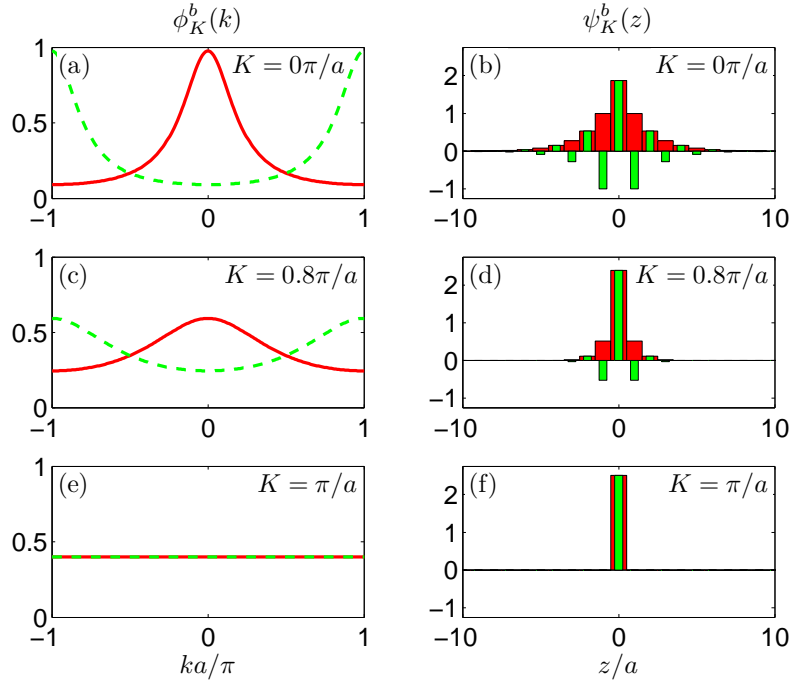


Figure 3.4: Repulsive (green) and attractive (red) bound state wave functions for $|U| = 2.7J$. The first column shows $\psi_K^b(k)$ in units of \sqrt{a} and the second $\psi_K^b(z)$ (dimensionless) obtained from Eqs. (3.50) and (3.48), respectively.

We note that the exponential factor in Eq. (3.48)

$$\kappa = \frac{1}{a} \cosh^{-1} \sqrt{1 + \frac{U^2}{E_K^2}} \simeq |U|/a |E_K| = |a_{\text{bg}}|^{-1} \quad (3.49)$$

in the limit where $U \rightarrow 0$ is precisely the decay constant found in Sec. 3.5.3. This together with the approximate formula for the binding energy (3.43) legitimize our definition of the scattering length.

In momentum space the normalized bound state wave function is given by

$$\phi_K^b(k) = \sqrt{\frac{a}{2\pi}} \frac{\mathcal{G}_K^0(E_b, k)}{\sqrt{E_b G(E_b, 0)^3}}, \quad (3.50)$$

which is peaked near the center of the Brillouin zone ($k = 0$) when the bound state energy is negative, and peaked near the edges of the Brillouin zone ($k = \pm\pi/a$) for $E_b > 0$, making it possible to discern the bound states with $E_b < 0$ from those with $E_b > 0$ in time-of-flight imaging [17]. This reflects that $\phi_K^{\text{op}}(k)$ is predominantly comprised of the *noninteracting* continuum states with energies, $\epsilon_K(k)$, in proximity of E_b . For $E_b > 0$ ($E_b < 0$) this corresponds to the states near the top (bottom) of the band. The height of the peaks is reduced as K approaches $\pm\pi/a$, where all scattering states become degenerate in our model. Here the quasi-momentum distribution of the bound state approaches a constant function, Fig. 3.4(e), and a delta function in the relative coordinate, Fig. 3.4(f).

3.6.3 Repulsively bound atom pairs

We observe from Fig. 3.4(a,c,e) that the quasi-momentum composition of the repulsively bound state is peaked around $k = \pi/a$ corresponding to the single-particle quasi-momenta $q_{A,B} = K/2 \pm \pi/a$, which in the first Brillouin zone always fall in the interval $(-\pi/a, -\pi/2a] \cup (\pi/2a, \pi/a]$. In this range the effective mass of the atoms are negative, and therefore a repulsive force causes attraction (see Sec. 2.8.2) [51]. The formation of repulsively bound pairs is thus explained by the induced band structure, which for certain quasi-momenta components result in an effective mass.

The reason why it is stable in an optical lattice, is that there are no dissipation channels available. Experimentally the binding energy of the bound pair states has been measured by modulation of the lattice depth. The bound pairs dissociate, when the modulation frequency are resonant with their binding energy. At resonance the dimers exchange energy with the undulating lattice and that is marked by the appearance of unbound atoms [17]. What this experiment does is to provide an externally controlled dissipation channel, a tunable phonon.

3.6.4 Investigating the bound state wave functions

If all the atoms initially are prepared in the $K = 0$ bound state. We can prepare the bound pairs in any K -state by exposing the system to a force field. This can be realized in practice by chirping the lattice lasers so that the lattice potential is accelerated in the laboratory frame [66]. To investigate the effect on the two-atom states, we make the new time dependent Ansatz

$$\Psi(x, y, t) = e^{iK(t)\frac{x+y}{2}} \psi(x - y, t) \quad (3.51)$$

with a time-dependent center-of-mass quasi-momentum, $K(t)$. Inserting this Ansatz into the time-dependent Schrödinger equation with a force field, $-F \cdot (x + y)$,

we obtain

$$i\hbar\frac{\partial}{\partial t}\psi(z,t) = \left(-2 \sum_{d>0} \cos(\frac{1}{2}K(t)da) J_d \left(\Delta_z^{(d)} + 2 \right) + U\delta_{z,0} \right) \psi(z,t) \quad (3.52)$$

if we choose

$$\dot{K}(t) = \frac{2F}{\hbar}. \quad (3.53)$$

Since there is an energy gap between the bound state and the scattering states, we may apply the adiabatic approximation to Eq. (3.52) and simply replace $\psi(x-y, t)$ by the eigenstate $\psi_K^b(x-y)$ of Eq. (6.2) with $K = K(t)$. Provided we accelerate the lattice slowly enough, it is thus possible to explore all the wave functions $\psi_K^b(x-y)$ of the system.

3.6.5 Symmetries

It is instructive to note the following symmetry in the continuum spectrum (3.9),

$$\epsilon_K(k) = -\epsilon_K(k + \pi/a). \quad (3.54)$$

This implies, according to Eq. (3.24),

$$\mathcal{G}_K^0(E, k) = -\mathcal{G}_K^0(-E, k + \pi/a), \quad (3.55)$$

and hence

$$1 = UG_K^0(E_{ab}(K), z=0) = (-U)G_K^0(-E_{ab}(K), z=0), \quad (3.56)$$

which relates the repulsively (rb) and attractively (ab) bound atom pair energies:

$$E_{rb}(K) = -E_{ab}(K). \quad (3.57)$$

In agreement with Eq. (3.42). Furthermore, Eq. (3.55) implies that the attractively and repulsively bound wave functions are related by [32]

$$\psi_K^{ab}(k) = \psi_K^{rb}(k + \pi/a). \quad (3.58)$$

This is seen from Fig. 3.4.

3.7 Spectral analysis

In this section we will perform a spectral analysis based on the full Green's functions. In general, given a retarded Green's operator, $\hat{G}(E)$, the corresponding spectral function is the imaginary part of the diagonal Green's function, $A(E, b) = -2\text{Im}\langle b|\hat{G}(E)|b\rangle$, in a basis $|b\rangle$ of orthonormal states.

3.7.1 Non-interaction particles

For the noninteracting system ($U = 0$) the spectral function is

$$A_K^0(E, z) = 2\pi D_K(E), \quad (3.59)$$

where $D_K(E)$ is the density of states (3.10). The unperturbed system has no bound states, and hence the spectral function is zero at all energies outside the continuum band. Inside the band the scattering states are equally distributed over the whole lattice, making the spectral function translationally invariant and directly proportional to the density of states, which diverges at the band edges, $E = \pm|E_K|$.

3.7.2 Interacting particles

For the spectral function of the interacting system we have to treat $|E| < |E_K|$ and $|E| > |E_K|$ separately. Outside the continuum $G_K^0(E, z)$ is real and we obtain the spectral function

$$\begin{aligned} A_K^U(E, z) &= 2\pi\delta(1 - UG_K^0(E, 0))UG_K^0(E, 0)^2e^{-2\kappa|z|} \\ &= 2\pi\frac{Ue^{-2\kappa_b|z|}}{E_b}\delta(E - E_b), \end{aligned} \quad (3.60)$$

where $\kappa_b a = \cosh^{-1} |E_b/E_K|$ is the decay constant for the bound state. This gives the probability distribution for finding a bound state atom pair with energy E_b and the atoms situated $|z|/a$ lattice sites apart in agreement with Eq. (3.48).

Inside the band we find

$$A_K^U(E, z) = \pi \left(|\psi_K^{\text{bg}}(E, z)|^2 + |\psi_K^{\text{bg}}(E, -z)|^2 \right) D_K(E), \quad (3.61)$$

where $\psi_K^{\text{bg}}(E, z)$ is the scattering wave defined in Eq. (3.28). Changing the sign of z is equivalent to changing the direction of the incoming wave in the scattering wave from k to $-k$. These two waves are degenerate and therefore it is natural to expect the average of the two for a given energy of the spectral function. We have used that the density of states is unchanged for elastic scattering, *i.e.*, $D_K(E)$ is also the density of states for atoms scattering under the influence of \hat{U} .

It is instructive to calculate the total spectral weight residing inside the continuum band:

$$\int_{-|E_K|}^{|E_K|} \frac{dE}{2\pi} A_K^U(E, z) = 1 - \frac{Ue^{-2\kappa_b|z|}}{E_b}. \quad (3.62)$$

With the addition of the bound state contribution, Eq. (3.60) the sum rule, $\int dE A_K^U(E, z)/2\pi = 1$, is then seen to be satisfied.

3.8 Conclusion

In this chapter we have derived all the basic ingredients used in the next three chapters. We assumed a delta-function interatomic interaction and only nearest-neighbor tunneling, which allowed us to do everything analytically. We derived the relative motion Green's functions and spectral densities for noninteracting atoms as well as for interacting atoms. We used the Green's functions to obtain the scattering waves and from them various scattering properties such as the scattering amplitude, the phase shift, a generalized scattering length [Sec. 3.5.3] and transmission coefficients [Sec. 3.5.1]. We showed that the delta-function interaction only support even partial waves, so that only $f_{\text{bg}} = f_{\text{even}}$ prevails. One-dimensional scattering is fully characterized by the reflection and transmission probability and we argued that even in the case of indistinguishable particles the transmission coefficient can be measured in photodissociation experiments [Sec. 3.5.2].

The Green's functions provided us with both the energies and wave functions of the bound states. Both quantities that can be measured in an experiment. The system features either a repulsive or an attractive bound state depending on whether the interaction constant U is positive or negative, where the repulsive state can be explained by a change in sign of the effective reduced mass of the atoms. Note that it is a unique feature of the 1D lattice that it features a bound state for any value of the interaction strength. In three-dimensional systems there is a cut off U_c such that there only exist a bound state for $|U| > U_c$ [32]. We showed that in the limit $U \rightarrow 0$, both the binding energy and the wave function are fully characterized by the generalized scattering length (3.38), which is inversely related to the 3D free space scattering length. Furthermore, we showed that the attractively and repulsively bound wave functions are related by a shift in relative quasi-momentum, $k \rightarrow k + \pi/a$ [Sec. 3.6.5]. The effective pair tunneling we found from the energy dispersion and it agreed with experimental findings [Sec. 3.6.1].

Another interesting approach to the two-body problem in a discrete lattice can be found in Ref. [67], where the two-body dynamics of a finite lattice with cyclic boundary condition is analyzed. The obtain bound states energies are identical to Eqs. (3.42) independently on the size of the lattice. Moreover, after the appearance of our paper [3], Valiente et al. [68] derived most of the results in this chapter by solving the Schrödinger equation without use of Green's functions.

Chapter 4

Two-channel Feshbach model

In this chapter we extend the discrete lattice description of atom pairs to a two-channel model, which will allow us to analyze the proximity of a Feshbach resonance. As we will see, the resonance alters the scattering properties and the bound states significantly. We also present several suggestions to experimentally measure our findings. Finally, we discuss the effect of higher Bloch bands on our model. Elaborate discussions of Feshbach physics in the context of cold atoms can be found in the reviews [34, 69, 70].

4.1 Introduction

Feshbach resonances arise in cold atomic collisions as a complex interplay between different molecular potentials and the hyperfine structure states. Here we will give a very short introduction to the origin of the Feshbach physics for ultracold alkali atoms. If exposed to a homogeneous applied magnetic field, the eigenstates of two atoms far apart are composed of each atom being in a definite hyperfine structure state, which is a combination of nuclear and electronic spin states. As the atoms approach, the interatomic interaction becomes important and in the case of alkali atoms with atomic spin $1/2$, the interaction is diagonalized by the singlet $S = 0$ and triplet $S = 1$ states, where S is the eigenvalue of the combined electronic spin $\mathbf{S} = \mathbf{S}_A + \mathbf{S}_B$. Here $\mathbf{S}_{A,B}$ is the spin operator of the individual atoms. Therefore, the interaction potential is of the form,

$$V(r) = V_s(r)\mathcal{P}_s + V_t(r)\mathcal{P}_t = \frac{V_s(r) + 3V_t(r)}{4} + (V_s(r) - V_t(r))\mathbf{S}_A \cdot \mathbf{S}_B \quad (4.1)$$

where $\mathcal{P}_s = 1/4 - \mathbf{S}_A \cdot \mathbf{S}_B$ and $\mathcal{P}_t = 3/4 + \mathbf{S}_A \cdot \mathbf{S}_B$ are the projection operator on the singlet and triplet state, respectively, and r is the interatomic separation. The $\mathbf{S}_A \cdot \mathbf{S}_B$ -term of (4.1) couples the different hyperfine structure states, but it is of inherently short range, since the singlet and the triplet potentials are asymptotically identical, *i.e.*, $V_{s,t}(r) \sim -C_6 r^{-6}$, and hence the difference $V_s(r) - V_t(r)$ vanish, unless the atoms are very close: $r < 1$ nm [70]. (The length scale of the singlet and triplet potentials are given by

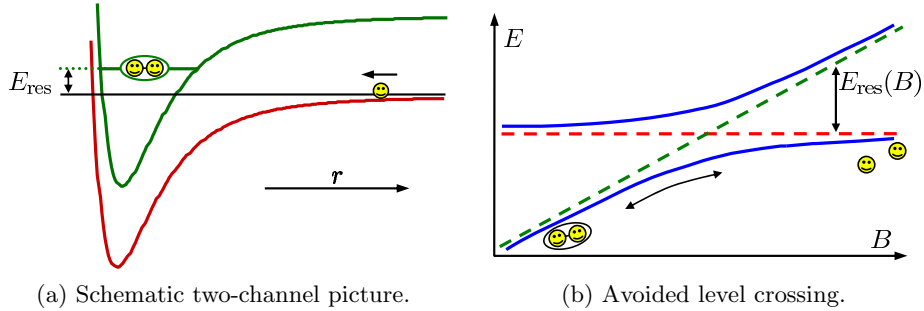


Figure 4.1: Schematic drawing of two coupled channels. (a) The red and green curve illustrate the open and closed channel, respectively, for a fixed externally applied magnetic field. The uncoupled closed channel features a bound state with energy $E_{\text{res}}(B)$ compared to the open-channel threshold (the horizontal black line). (b) The horizontal and inclined dashed lines show the energy of the state of the free atoms and the resonance state, respectively. The separation of the two uncoupled levels are $E_{\text{res}}(B)$, which depends on the external magnetic field. Because the two states couples, the true energy levels are the blue lines. In drawing this figure we have assumed that there is only one bound state in the closed channel and one scattering state in the open channel.) If we start out with high magnetic field and the atoms in the open channel, and *adiabatically* decrease the magnetic field, the atoms will end up in the resonance (molecular) state in the lower left corner of the figure.

$r_0 = (C_6 m/m_e)^{1/4} a_B$, which is of the order 10 nm for alkali atoms. Here m (m_e) is the atomic (electron) mass and a_B is the Bohr radius.) We refer to the different pairwise combinations of hyperfine structure levels for the asymptotically separated atoms as channels, and the dissociation threshold of a channel is the sum of the energies of the hyperfine structure states. A channel is referred to as open or closed depending on whether the energy of the relative motion of the two atoms is above or below the channel threshold, *i.e.*, whether the atoms are in the continuum and can escape each other or are trapped in a bound state. The difference in the magnetic moments of the channels allow external control of the relative position of the potentials by a magnetic field due to the linear Zeeman effect. In the basis of the eigenstates of the hyperfine Hamiltonian the interaction is not diagonal due to the $\mathbf{S}_A \cdot \mathbf{S}_B$ -term in (4.1), and hence the interaction potential couples different channels. However, due to rotational symmetry only channels with the same $m_F = m_{F_A} + m_{F_B}$ quantum number are coupled.

A Feshbach resonance arises when a bound state in a closed channel is embedded in the continuum of the open channel. This is illustrated in Fig. 4.1(a). We will restrict our analysis to an isolated resonance, that is, a system where only one bound state is present near the open channel threshold. In that case the physics can be described by a two-channel model based on very few ex-

perimental parameters [71]. From the scattering perspective, see Fig. 4.1(a), two atoms approach each other in the continuum of the open channel (red potential curve) from the infinitely far. As they come close they couple to the bound state of the closed channel (green potential curve), and they may stay there for some time before they are transferred back into the continuum and travel apart again. This will substantially modifies both the scattering dynamics and the bound states of the pair. This is most clearly seen from the scattering length, which for low energies completely characterizes the scattering dynamics. We encountered the scattering length in Sec. 3.3, where it was argued that the on-site interaction strength U is proportional to this number. As a bound state of the diagonalized coupled channel Hamiltonian enters the continuum, the scattering length diverges:

$$a(B) = a_{\text{bg}}^{3\text{D}} \left(1 - \frac{\Delta B}{B - B_0^{\text{free}}} \right), \quad (4.2)$$

where $a_{\text{bg}}^{3\text{D}}$ is the scattering length when the closed-channel states are far off-resonant, B_0^{free} is the magnetic field resonance position, and ΔB is the width of the resonance, see Fig. 4.2. Note that the magnetic field resonance position B_0^{free} is not the same as the magnetic field $B_{\text{res}}^{\text{free}}$, where the uncoupled resonance state is degenerate with the entrance channel threshold, see Fig. 4.3. The offset may be approximately evaluated by

$$B_0^{\text{free}} - B_{\text{res}}^{\text{free}} = \Delta B f(y). \quad (4.3)$$

Here $f(y) = y(1-y)/[1+(1-y)^2]$ is a dimensionless function of the ratio $y = a_{\text{bg}}^{3\text{D}}/\bar{a}$ between the background scattering length and the so-called mean scattering length $\bar{a} \approx 0.478(mC_6/\hbar^2)^{1/4}$, which is a characteristic length scale for the long range part of the molecular potential [70].

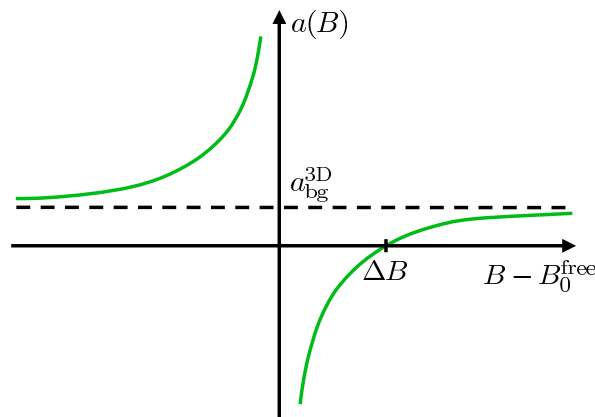


Figure 4.2: Schematic drawing of the magnetic field dependent scattering length in free space, Eq. (4.2). The dashed line indicates the background contribution to the scattering length, $a_{\text{bg}}^{3\text{D}}$.

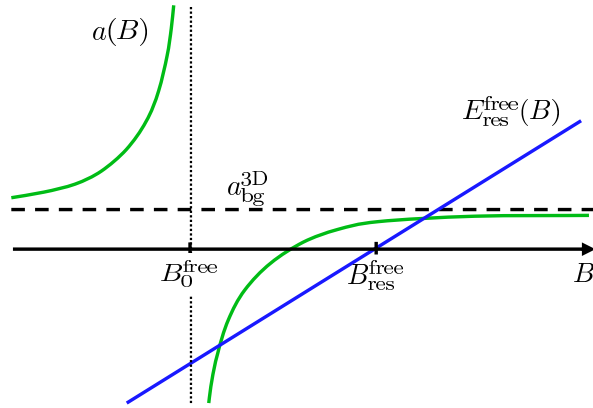


Figure 4.3: Schematic drawing of the magnetic field dependent scattering length $a(B)$ (green curve) and the energy of the uncoupled bound state with respect to the continuum threshold of the open channel $E_{\text{res}}^{\text{free}}(B)$ (blue line) both in free space without a lattice. The green curve has units of length, whereas the blue has units of energy. We observe that the position of the divergence in scattering length B_0^{free} , which may be observed in experiments, is displaced with respect to the zero crossing of the free space resonance energy $B_{\text{res}}^{\text{free}}$.

Feshbach physics is of great interest for many reasons. One is that the resonances can be detected with high precision (in some experiments within a few mG [72, 73]) for a large range of magnetic field values and from this, important knowledge about the details of the interatomic interaction can be extracted, such as for example the scattering lengths and the van der Waals coefficient C_6 - collisional properties of great importance in ultracold physics [73, 74]. Feshbach resonances also provide an efficient scheme for converting ultracold atoms into ultracold molecules - cooling molecules is in general a very difficult task due to the many internal rotational and vibrational levels. The principle of molecular formation is illustrated in Fig. 4.1(b). Here the dashed lines are the energy of an uncoupled bound state (green) and a scattering state (red) as function of the magnetic field B . When coupled an avoided crossing appears, *i.e.*, the energy of the eigenstates of the coupled Hamiltonian represented by the blue lines do not cross. If we start out with high magnetic field B and free atoms, and adiabatically decrease the magnetic field, the atoms will stay in the same (blue) state, and end up as molecules in the lower left corner of the figure.

This has facilitated the experimental production of cold molecular gases. One example is the creation of a molecular condensate from a degenerate Fermi gas of atoms, which is of great interest due to the crossover between the Bardeen-Cooper-Schrieffer superfluidity in an atomic Fermi gas (due to formation of cooper-pairs) and the BEC-type superfluidity in a condensate of molecular bosons [75–79]. Another novel achievement in this direction is the

coherent conversion of an atomic Bose-Einstein condensate into a ultracold molecular gas and back again [80].

Furthermore, a Feshbach resonance is a powerful tool together with an optical lattice. Recall, that a resonance can be used to fabricate atomic states with either zero or two atoms per lattice site. We argued in the previous chapter that this makes it possible to two-body systems in cold atomic physics, which is the motivation for the two-body analysis in this thesis. Furthermore, the lattice may also improve the molecular formation. The conversion efficiency is strongly dependent on the overlap of the atomic wave functions, due to the short range of the coupling. Moreover, the created molecules are very loosely bound, and therefore very sensitive to collisions. Both problems that can be addressed by an optical lattice, where the atoms can be confined to a single cell increasing the wave function overlap, and furthermore, if one starts out with exactly two atoms per site, there is no atoms left to collide with when a molecule is formed.

4.2 Two-channel picture

In Chap. 3 we only considered a single interatomic potential at energies above the continuum threshold, where the atoms are asymptotically free to move (in the lattice). We will refer to this as the open channel and denote its Hamiltonian $\hat{H}^{\text{op}} = \hat{H}_0 + U\delta_{z,0}$ [see Eq. (3.12)]. Furthermore, we now include a second channel with Hamiltonian \hat{H}^{cl} , which only features bound states at the energy range at consideration, and a coupling \hat{W} that mixes the two channels. We thus have a set of coupled equations for the relative motion

$$\hat{H}^{\text{op}}|\psi_K^{\text{op}}\rangle + \hat{W}|\psi_K^{\text{cl}}\rangle = E|\psi_K^{\text{op}}\rangle, \quad (4.4a)$$

$$\hat{H}^{\text{cl}}|\psi_K^{\text{cl}}\rangle + \hat{W}|\psi_K^{\text{op}}\rangle = E|\psi_K^{\text{cl}}\rangle. \quad (4.4b)$$

Due to the large splitting between the rotational and vibrational levels in the closed channel compared to the collision energies in ultracold atomic gases, the resonance physics is faithfully represented by considering only a single bound state $|\phi_{\text{res}}\rangle$ of \hat{H}^{cl} with energy $E_{\text{res}}(B, K)$ [81]. This amounts to a single-pole approximation for the closed-channel Green's function

$$\hat{G}_K^{\text{cl}}(E, B) \approx \frac{|\phi_{\text{res}}\rangle\langle\phi_{\text{res}}|}{E - E_{\text{res}}(B, K)}. \quad (4.5)$$

4.2.1 Energy of the resonance state

The energy of the resonance state $E_{\text{res}}(B, K)$ is composed (i) of the free space resonance energy

$$E_{\text{res}}^{\text{free}}(B) = \Delta\mu(B - B_{\text{res}}^{\text{free}}) \quad (4.6)$$

measured relative to the open-channel (free space) threshold, and (ii) the displacement of the closed and open channel Bloch bands caused by the applied

periodic potential. The first part is linearly tunable with the applied magnetic field, due to the difference $\Delta\mu$ between the open and closed channel magnetic moments. Here $B_{\text{res}}^{\text{free}}$ is the magnetic field position at which the uncoupled $|\phi_{\text{res}}\rangle$ state is degenerate with the entrance channel threshold. If we insert Eq. (4.3) into (4.6) we obtain

$$E_{\text{res}}^{\text{free}}(B) = \Delta\mu[B - B_{\text{res}}^{\text{free}}] = \Delta\mu[B - B_0^{\text{free}} + \Delta B f(y)], \quad (4.7)$$

which instead includes the observable resonance position B_0^{free} . The second contribution is a lattice feature which depends on the lattice strength and the center-of-mass quasi-momentum K .

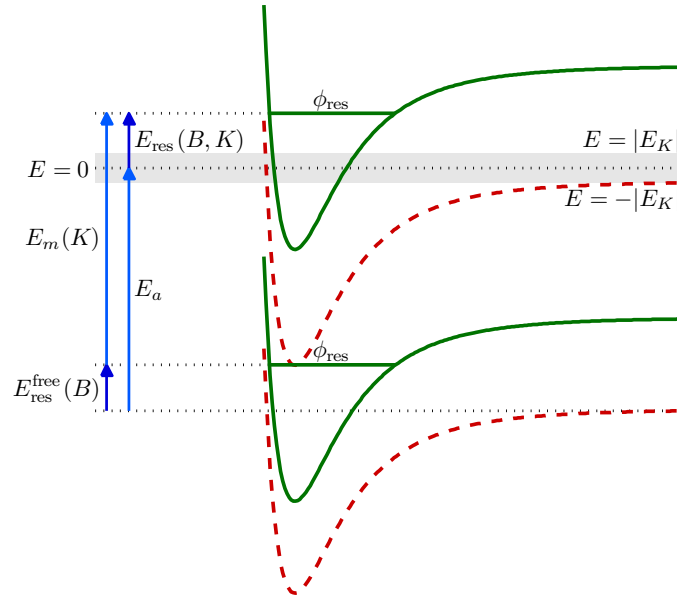


Figure 4.4: Schematic diagram illustrating the difference between two-channel scattering in free space and in an optical lattice. The dashed and solid curves are the open and closed channel potentials, respectively. For the lower pair of potential curves the lattice is absent, and $E_{\text{res}}^{\text{free}}(B)$ is the energy of ϕ_{res} relative to the open channel threshold. As an optical lattice is applied the atomic and molecular curves are displaced by E_a and $E_m(K)$, respectively, giving rise to a new resonance energy $E_{\text{res}}(B, K)$. The continuum in the open channel is indicated by the gray shadow, where the thresholds are $\pm E_K$.

4.2.2 Lattice part of the resonance shift

As a function of continuous position variables the longitudinal lattice potential for each atom is $V_0^{\parallel} E_R \sin^2(\pi x_{3i}/a)$ with $i = A, B$, and therefore the combined

lattice potential for a pair of atoms in the resonance state is

$$V_{\text{lat}}^{\parallel}(x_{31}, x_{32}) = 2V_0^{\parallel} E_{\text{R}} \sin^2\left(\frac{\pi X_3}{a}\right) \cos^2\left(\frac{\pi \delta x_3}{2a}\right) + 2V_0^{\parallel} E_{\text{R}} \cos^2\left(\frac{\pi X_3}{a}\right) \sin^2\left(\frac{\pi \delta x_3}{2a}\right), \quad (4.8)$$

where we have introduced the continuous center-of-mass, $X_3 = (x_{3A} + x_{3B})/2$, and relative, $\delta x_3 = x_{3A} - x_{3B}$, coordinates. Since the size of the closed channel bound state causing the resonance is much smaller than the lattice spacing, we may consider the limit of $\delta x_3 \ll a$ for this state. Consequently, the resonant state has a center-of-mass motion corresponding to a lattice potential twice as deep as that governing the motion of the individual atoms, while its mass is the sum of the two atomic masses. Therefore the Bloch bands for the atoms and molecules are different both in location and width.

Taking this into account, the position of the open and closed channel change by $E_a = 2(E_1^{\parallel} + 2E_1^{\perp})$ and $E_m(K) = E_1^{m\parallel} - 2J_m \cos(Ka) + 2E_1^{m\perp}$, respectively, when an optical lattice is applied, as illustrated in Fig. 4.4. Here E_1^i and E_1^{mi} is the average energy of the first Bloch band (*i.e.* the zero-order tunneling $-J_0$) along direction i for atoms and a molecules, respectively, and J_m is the longitudinal tunnel rate of the bare molecule, which is small compared with the atomic tunnel rate, *i.e.*, $|J_m| \ll |J|$, because the molecules experience twice as deep a lattice potential. Note that the position of the open channel threshold also depends on the center-of-mass quasi-momentum, but we choose $E = 0$ to be the center of the open-channel band, therefore E_a is independent on K . As a consequence the true thresholds are now located at $\pm|E_K|$. Hence, the difference in energy between the closed-channel bound state and the center of the open-channel band in the presence of the lattice is

$$E_{\text{res}}(B, K) = E_{\text{res}}^{\text{free}}(B) + E_m(K) - E_a = \bar{E}_{\text{res}}(B) - 2J_m \cos(Ka), \quad (4.9)$$

where the band-averaged resonance energy $\bar{E}_{\text{res}}(B)$ incorporates the energy shifts of the atomic and molecular bands in the lattice.

4.3 The coupling matrix

The coupling to the closed channel is of inherently short range, as already argued, and in addition, the closed-channel bound state has a size (typically tens of Å), which is small compared with the lattice spacing (hundreds of nm). We thus assume a purely on-site coupling, which in free space couple molecular and atomic plane wave states with a strength $g_{\text{res}} = \sqrt{4\pi\hbar^2 a_{\text{bg}}^{3\text{D}} \Delta\mu\Delta B/m}$. In the discrete lattice model this results in the matrix element

$$\begin{aligned} \mathcal{W} &= g_{\text{res}} \prod_{i=1,2} \int dx_i w_{10}^{\text{cl},\perp}(x_i) w_{10}^{\perp}(x_i)^2 \\ &\quad \times \int dx_3 w_{10}^{\text{cl},\parallel}(x_3) w_{10}^{\parallel}(x_3) w_{10}^{\parallel}(x_3) \end{aligned} \quad (4.10)$$

for the coupling of a pair of atoms and a bare molecule all in the first Bloch band. With the exception of Sec. 4.7 we will consider exclusively the lowest Bloch band for both the atoms and the molecule.

We emphasize that our model only depends on three parameters to characterize the dynamics in the lattice: J , U and \mathcal{W} . In terms of the relative motion formalism the latter corresponds to the following matrix representation of \hat{W}

$$\langle z, \text{op} | \hat{W} | \phi_{\text{res}} \rangle = \mathcal{W} \delta_{z,0}, \quad (4.11)$$

where z is the open channel relative coordinate.

As will be discussed in Sec. 4.7, our discrete two-channel model is valid for narrow Feshbach resonances. To illustrate our analytical results we use the resonance in ^{87}Rb near 414 G [82], for which $\Delta B = 18$ mG, $\Delta\mu = 111$ kHz/G and the background scattering length is 100.8 Bohr radii. For all the plots in this chapter we consider a lattice with $V_0^\perp = 30$ and $V_0^\parallel = 1$. This results in interaction parameter $U = 1.4J$ and coupling strength $\mathcal{W} = 2.2J$. Table 4.1 gives the relevant model parameters for this resonance and a range of lattice depths.

V_0^\parallel	V_0^\perp	J/E_R	J_m/E_R	U/J	\mathcal{W}/J
1	15	0.18	0.043	0.9	1.8
2	15	0.14	0.015	1.4	2.5
3	15	0.11	0.006	2.1	3.4
4	15	0.085	0.003	3.0	4.6
5	15	0.066	0.001	4.2	6.2
1	30	0.18	0.043	1.4	2.2
2	30	0.14	0.015	2.1	3.0
3	30	0.11	0.006	3.1	4.1
4	30	0.085	0.003	4.5	5.6
5	30	0.066	0.001	6.3	7.6

Table 4.1: Discrete lattice parameters for the ^{87}Rb Feshbach resonance near 414 G. The recoil energy is $E_R = 3.5$ kHz.

4.4 Scattering properties

With the explicit single-pole expression for the closed-channel Green's function (4.5) the closed-channel part of the scattering problem (4.4b) may be solved formally:

$$|\psi_K^{\text{cl}}(E)\rangle = \hat{G}_K^{\text{cl}}(E, B) \hat{W} |\psi_K^{\text{op}}\rangle = \frac{|\phi_{\text{res}}\rangle \mathcal{W} \psi_K^{\text{op}}(0)}{E - E_{\text{res}}(B, K)}. \quad (4.12)$$

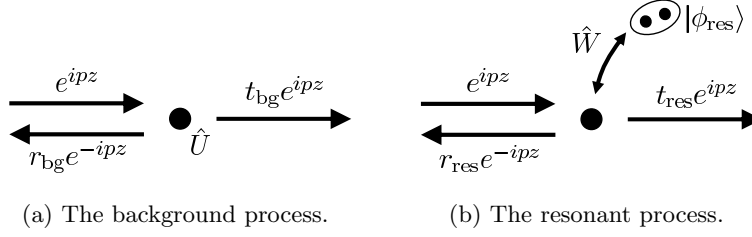


Figure 4.5: Schematic drawing of the scattering process.

The general solution to the open-channel component will be

$$\begin{aligned}\psi_K^{\text{op}}(E, z) &= \psi_K^{\text{bg}}(z) + \hat{G}_K^U(E)\hat{W}|\psi_K^{\text{cl}}(E)\rangle \\ &= \psi_K^{\text{bg}}(z) + \psi_K^{\text{bg}}(0)e^{ip|z|}\frac{\Sigma_M(E, K)}{E - E_{\text{res}}(B, K) - \Sigma_M(E, K)}\end{aligned}\quad (4.13)$$

Like in the previous chapter relative quasi-momentum of the scattering atoms is $pa = \cos^{-1}(E/E_K)$. Here we have introduced the molecular self-energy $\Sigma_M(E, K) = \langle \phi_{\text{res}} | \hat{W} \hat{G}_K^U(E) \hat{W} | \phi_{\text{res}} \rangle$, which for the on-site coupling may be written as $\Sigma_M(E, K) = \mathcal{W}^2 G_K^U(E, 0)$.

When $z \geq 0$ we can rewrite the above wave function in the convenient form

$$\psi_K^{\text{op}}(E, z) = t_{\text{bg}} e^{ipz} \left[1 + \frac{\Sigma_M(E, K)}{E - E_{\text{res}}(B, K) - \Sigma_M(E, K)} \right]. \quad (4.14)$$

4.4.1 Transmission profile

From the form of the scattered wave (4.14) the transmission amplitude, $t(E, K)$, is readily identified. It is divided into two parts, $t(E, K) = t_{\text{bg}}(E, K) + t_{\text{res}}(E, K)$, where the first is the transmission amplitude in the absence of the resonance and the latter is the resonant transmission amplitude, as illustrated in Fig. 4.5. The two contribution can interfere both constructively and destructively depending on the scattering energy E giving rise to a total transmission coefficient of the Fano form [83]

$$T(E, K) = T_{\text{bg}}(E, K) \frac{(\epsilon + q)^2}{\epsilon^2 + 1}. \quad (4.15)$$

The Fano parameters $\epsilon = 2(E - E_{\text{res}} - \Delta)/(\hbar\Gamma)$ and $q = 2\Delta/\hbar\Gamma$ depend on the resonance shift and width functions, which are related to the real and imaginary parts of the molecular self-energy,

$$\Sigma_M(E, K) = \Delta(E, K) - i\hbar\Gamma(E, K)/2, \quad (4.16)$$

where the real part

$$\Delta(E, K) = -\frac{U\mathcal{W}^2}{E_K^2 + U^2 - E^2} \quad (|E| < |E_K|) \quad (4.17)$$

describes the self consistently determined shift of the resonance position from E_{res} to $E_{\text{res}}^* = E_{\text{res}} + \Delta(E_{\text{res}}^*, K)$, and

$$\hbar\Gamma(E, K) = \frac{2\mathcal{W}^2\sqrt{E_K^2 - E^2}}{E_K^2 + U^2 - E^2} \quad (|E| < |E_K|) \quad (4.18)$$

is the decay width of the resonance state due to the coupling to the continuum. Outside the continuum $\Gamma(E, K) = 0$, and the molecules are stable against dissociation. The real part of the molecular self-energy outside the band

$$\Delta(E, K) = \frac{\text{sgn}(E)\mathcal{W}^2}{\sqrt{E^2 - E_K^2} - U\text{sgn}(E)} \quad (|E| > |E_K|) \quad (4.19)$$

determines the energies of the bound states for a given resonance energy as described in Section 4.5. The width and shift of the resonance are illustrated in Fig. 4.6 along with the Fano parameters for $K = 0$.

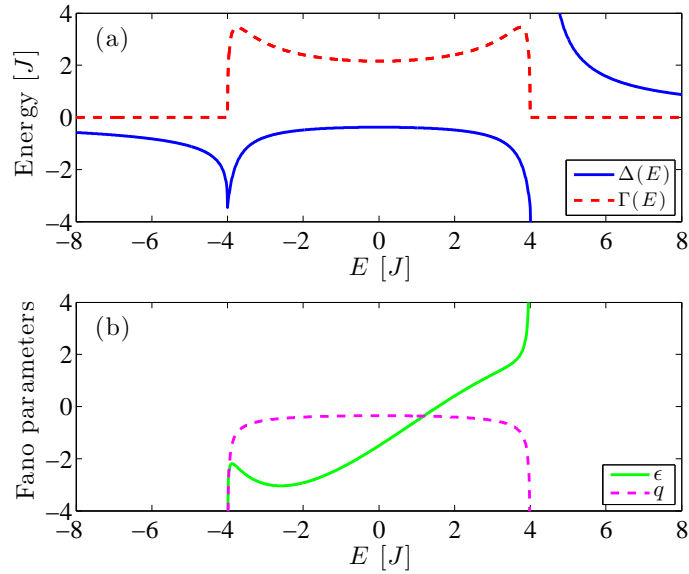


Figure 4.6: (a) The shift $\Delta(E, K)$ and width $\Gamma(E, K)$ of the resonance for $K = 0$ where the band edges are at $E = \pm 4J$. The real part of the molecular self-energy is continuous across the band edges and has a pole at the uncoupled bound state energy, E_b^0 (see Sec. 4.5). (b) The Fano parameters, ϵ and q , parametrize the shape of the transmission resonance. In both plots: $\bar{E}_{\text{res}} = 2J$.

The Fano profile is shown for various q -values in Fig. 4.7. We note that the asymmetry parameter $q = -U/\sqrt{E_K^2 - E^2}$ is independent of the coupling strength \mathcal{W} and it is related to the background transmission probability

through the relation $T_{\text{bg}} = 1/(1 + q^2)$. This is a consequence of the inversion symmetry [84] and it ensures us that there will be a point of total transmission, whenever the Fano profile attains its maximum value, $(1 + q^2)$, in the continuum.

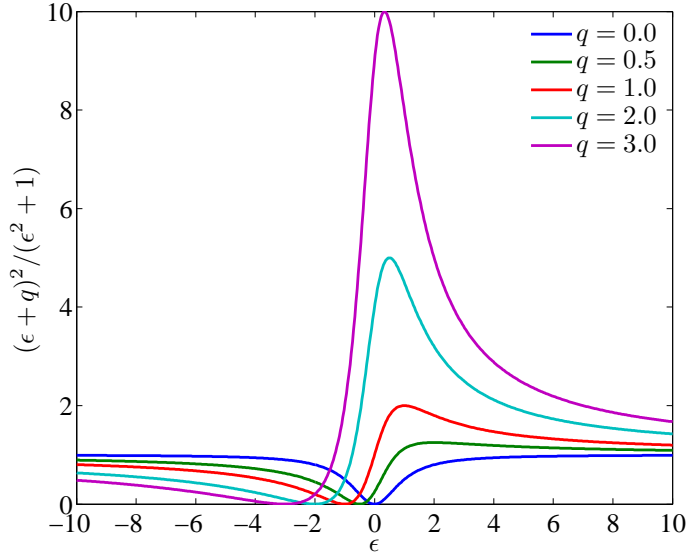


Figure 4.7: Fano profiles for different values of the asymmetry parameter q . The Fano profile has minimum at $-q$ and maximum at $1/q$, where it reaches 0 and $q^2 + 1$, respectively. The profile approach unity as $\epsilon \rightarrow \pm\infty$.

The reflection maximum of the Fano profile occurs at $\epsilon = -q$, which happens at $E = E_{\text{res}}(B, K)$. This is nearly independent of the center-of-mass motion, due to the weak tunneling of the closed-channel molecules. This point of total reflection only occurs, when the bare resonance state lies inside the continuum. Just as in the non-resonant case the reflection probability is unity at the band edges. Hence the reflection profile has two minima, whenever $|E_{\text{res}}| < |E_K|$. When the bare resonance state lies outside the band, $R(E, K)$ has a single minimum. The two-channel reflection profiles are plotted in Figs. 4.8(a)-(d) and 4.9(a) as colormaps and in Figs. 4.8(e)-(h) and 4.9(b) as solid lines. For the parameters used in the quantitative calculations throughout this paper $J_m/J \approx 0.2$, and hence the resonance energy appears nearly independent of K in Figs. 4.8(a)-(d).

The condition for total transmission is $\epsilon q = 1$, corresponding to $E = E_{\text{res}}(B, K) - \mathcal{W}^2/U$. As E_{res} is ramped upwards (downwards) starting below (above) the band, this point of destructive interference between the direct and resonant scattering amplitudes first appears at the magnetic field, where a bound state of the coupled channels system enters the continuum to become a scattering resonance. As we shall see below, this occurs at two critical values where

$$E_{\text{res}} = \pm|E_K| + \mathcal{W}^2/U. \quad (4.20)$$

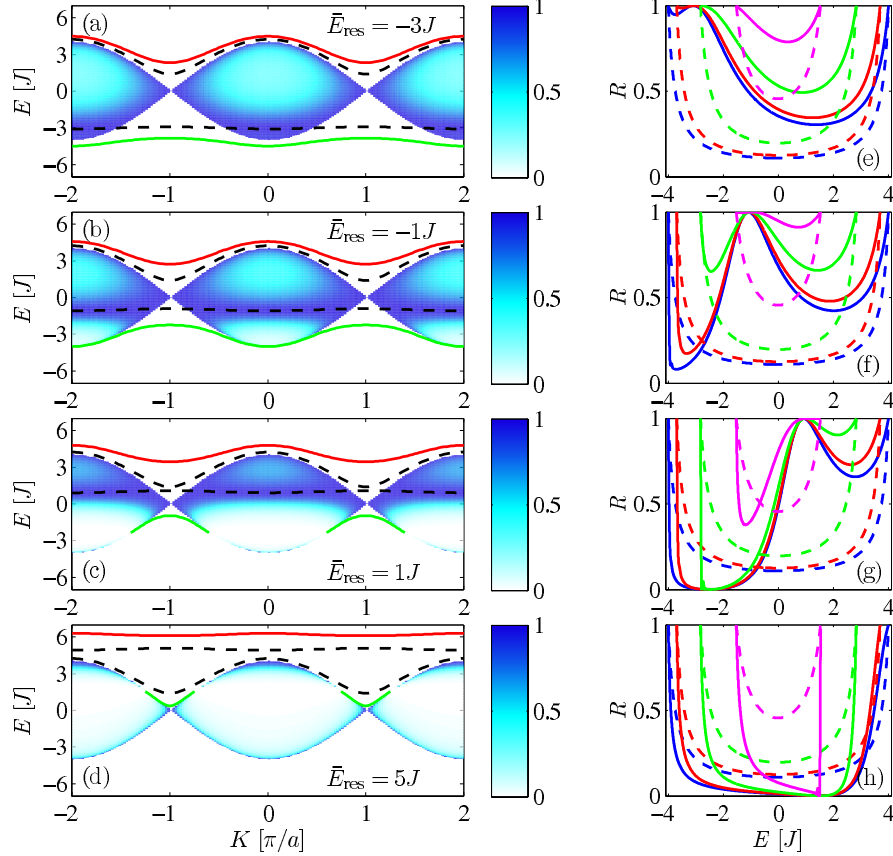


Figure 4.8: (a)-(d) Scattering properties and bound states in an extended zone scheme at different values of the resonance energy. The colormap inside the band illustrates the reflection probability, $R(E, K)$, ranging from 0 (white) to 1 (dark blue). The solid lines are the bound state energies of the coupled system, while the dashed curves indicate the diabatic, uncoupled bound states with the nearly horizontal line giving E_{res} and the other corresponding to the uncoupled dimer state E_b^0 , Eq. (3.42). (e)-(h) Reflection coefficient (solid lines) and the background reflection probability, R_{bg} (dashed lines) for $K=0, 0.25, 0.5, 0.75 \pi/a$ (from the bottom to the top at $E=0$). Plots are shown for resonance energies $\bar{E}_{\text{res}} = -3J$ (a,e), $-J$ (b,f), J (c,g), and $5J$ (d,h).

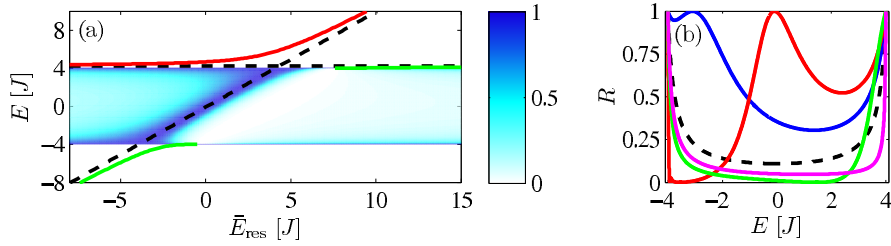


Figure 4.9: (a) Bound state energies (solid lines) and reflection coefficient across the continuum band (colormap) as a function of \bar{E}_{res} for a fixed $K = 0$. The horizontal dashed line is the repulsively bound pair state existing above the band for $\mathcal{W} = 0$, while the diagonal dashed curve is the band averaged resonance energy, \bar{E}_{res} . (b) Cuts showing the reflection probability at $\bar{E}_{\text{res}} = 0, -3, 10, \text{ and } 5J$ (solid lines from top to bottom at $E = 0$). The dashed black curve indicate the reflection profile in the absence of the coupling.

This is exactly the points delineating the region, where the condition $\epsilon q = 1$ can be satisfied. The reflection profile will thus only have both a Fano maximum and a Fano minimum if the conditions $|E_{\text{res}}| < |E_K|$ and $|E_{\text{res}} - \mathcal{W}^2/U| < |E_K|$ are simultaneously met.

Neglecting the background interaction corresponds to the limit $T_{\text{bg}} \rightarrow 1$, or equivalently $U, q \rightarrow 0$. In this case the resonance shift vanishes and the reflection probability assumes a simple Breit-Wigner-like profile [84]

$$R(E, K) \xrightarrow{U \rightarrow 0} \frac{\hbar^2 \Gamma_0^2(E, K)/4}{[E - E_{\text{res}}(B, K)]^2 + \frac{\hbar^2 \Gamma_0^2(E, K)}{4}}, \quad (4.21)$$

where $\hbar \Gamma_0(E, K) = 2\mathcal{W}^2/\sqrt{E_K^2 - E^2}$. The opposite limit of $|U| \rightarrow \infty$ on the other hand corresponds to $T_{\text{bg}} \rightarrow 0$ and $q \rightarrow \infty$, giving rise to a Breit-Wigner-like form of the transmission coefficient [84]

$$T(E, K) \xrightarrow{|U| \rightarrow \infty} \frac{\hbar^2 \Gamma_\infty^2(E, K)/4}{[E - E_{\text{res}}(B, K) - \Delta_\infty]^2 + \frac{\hbar^2 \Gamma_\infty^2(E, K)}{4}}, \quad (4.22)$$

corresponding to a dip in the reflection probability at the resonance, which now occurs at $E = E_{\text{res}}(B, K) + \Delta_\infty$. The resonance shift, $\Delta_\infty = -\mathcal{W}^2/U$, is independent of energy and momentum, while the width is given by $\hbar \Gamma_\infty(E, K) = 2\mathcal{W}^2\sqrt{E_K^2 - E^2}/U^2$. Both the shift and the width approach zero as the strength of the on-site interaction is increased.

4.4.2 Spectroscopic probing of the Fano profile

The observations regarding indistinguishable particles in section 3.5.2 can be directly carried over to the situation with more than one channel. Again, the transmission coefficient $T(E, K)$ has no straightforward meaning in the

scattering of identical bosons. But it is clear that the transition probability from an initial state $|i\rangle$ to the stationary scattering state ψ_K^{op} under the action of some transition operator \hat{T} is

$$|\langle \psi_K^{\text{op}} | \hat{T} | i \rangle|^2 \propto |\psi_K^{\text{op}}(z=0)|^2 = T(E, K). \quad (4.23)$$

Therefore, the resonance profile is accessible spectroscopically by scanning the energy of the final state across the continuum. Starting from a deeper bound state of the system the dissociated atom signal will have the same energy variation as $T(E, K)$.

4.4.3 Scattering length

The scattering amplitude in the coupled channels case consists of a background and a resonant contribution, $f(E, K) = f_{\text{bg}}(E, K) + f_{\text{res}}(E, K)$, where the resonant part

$$f_{\text{res}}(E, K) = \frac{\mathcal{W}^2 G_K^0(E, 0) / [1 - U G_K^0(E, 0)]^2}{E - E_{\text{res}}(B, K) - \Sigma_M(E, K)} \quad (4.24)$$

is obtained by comparing (4.14) with $e^{ipz}(1 + f_{\text{bg}} + f_{\text{res}})$ for $z \rightarrow \infty$, and the background part, f_{bg} , was derived in Eq. (3.30). The phase shift is related to the scattering amplitude in the same way as in the single-channel case, see Eq. (3.33).

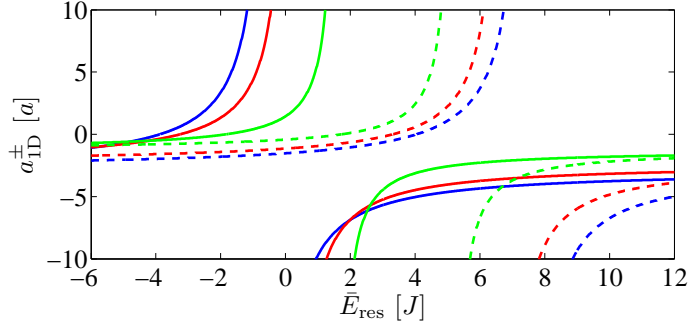


Figure 4.10: Generalized one-dimensional scattering length in the lattice, Eq. (4.25). Solid lines show a_{1D}^{-} at $K = 0, 0.4,$ and $0.7 \pi/a$ (from the left to the right), while the dashed lines correspond to a_{1D}^{+} at the same K -values (increasing from the right to the left).

As in the case of single-channel scattering we define a generalized one-dimensional lattice scattering length, $a_{1D}^{\pm}(K)$, from the limit of the scattering amplitude, $f \rightarrow -[1 + i\kappa a_{1D}^{\pm}]^{-1}$, at the extrema of the relative energy, $\kappa \rightarrow 0$. We remind the reader that $\kappa = k$ ($\kappa = \pm\pi - k$) at the lower (upper) continuum threshold (see Sec. 3.5.3). After some algebra we arrive at the

simple expression

$$a_{1D}^{\pm}(B, K) = a_{\text{bg}}(K) \left[1 + \frac{\mathcal{W}^2/U}{E_{\text{res}}(B, K) - \mathcal{W}^2/U \mp |E_K|} \right] \quad (4.25)$$

for the generalized one-dimensional scattering length, with the upper and lower sign corresponding to the top and the bottom edge of the continuum, respectively. The scattering length is displayed in Fig. 4.10. It reduces to the non-resonant scattering length $a_{\text{bg}}(K)$, Eq. (3.38), when the coupling \mathcal{W} approaches zero. The lattice scattering length is of the standard Feshbach form [85],

$$a_{\text{bg}} [1 + \Delta B / \Delta\mu (B - B_0)],$$

except that it does not diverge at the same value of the magnetic field at the top and the bottom of the continuum. The motivation for the chosen sign convention of the scattering length at the upper band edge is guided by the rationale that the two scattering lengths, a_{1D}^- and a_{1D}^+ , then become equal in the limit of a deep lattice, where $|E_K|$ goes to zero.

It is convenient to define a pair of detunings

$$\delta^{\pm}(B, K) \equiv E_{\text{res}}(B, K) - \mathcal{W}^2/U \mp |E_K|, \quad (4.26)$$

such that the one-dimensional scattering length diverges at the magnetic field strengths, B_0^{\pm} , where $\delta^{\pm}(B_0^{\pm}, K) = 0$. We thus get two resonance positions, one for scattering near the upper band edge, and one for scattering near the lower band edge, as shown in Fig. 4.10(a). We caution that the relative position of B_0^+ and B_0^- depends on the sign of the magnetic moment difference, $\Delta\mu$. If $\Delta\mu > 0$ ($\Delta\mu < 0$), then B_0^+ lies above (below) B_0^- . The lattice resonance positions B_0^+ and B_0^- are shown in Fig. 4.11 as function of the lattice depth, V_0^{\parallel} . They are separated by $2|E_K|/\Delta\mu$ and approach each other as V_0^{\parallel} is increased, since $|E_K|$ decreases. Furthermore, in the limit where both the transverse and the longitudinal lattice depths are large, *i.e.*, $V_0^{\perp}, V_0^{\parallel} \gg 1$, the Wannier orbitals approach harmonic oscillator states, and we have that

$$\mathcal{W}^2/U \rightarrow g_{\text{res}}^2/g_{\text{bg}} = \Delta\mu\Delta B, \quad (4.27a)$$

$$E_a \rightarrow 2\sqrt{V_0^{\parallel}}E_R + 4\sqrt{V_0^{\perp}}E_R, \quad (4.27b)$$

$$E_m(K) \rightarrow \sqrt{V_0^{\parallel}}E_R + 2\sqrt{V_0^{\perp}}E_R. \quad (4.27c)$$

This gives the following asymptotic behavior of the magnetic field resonance position

$$B_0^{\pm} \rightarrow B_0^{\text{free}} + \Delta B[1 - f(y)] + \frac{E_R}{\Delta\mu}\sqrt{V_0^{\parallel}} + \frac{2E_R}{\Delta\mu}\sqrt{V_0^{\perp}} \quad (4.28)$$

where B_0^{free} is the Feshbach resonance position in the absence of the lattice, and the dimensionless function $f(y)$ is defined below Eq. (4.3). The asymptotic behavior is indicated by the black dash-dotted curves in Fig. 4.11. The resonance position were measured in [82, see Fig. 3].

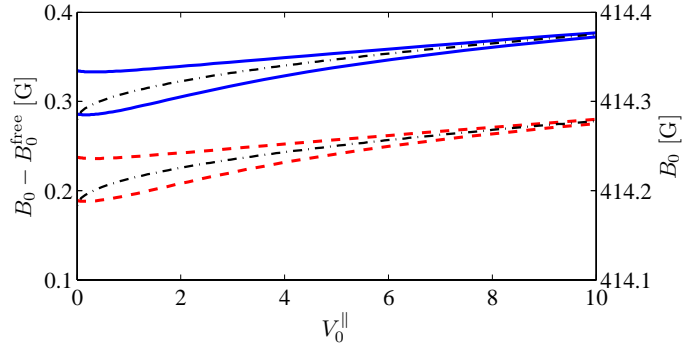


Figure 4.11: Magnetic field position of the scattering length divergences as a function of the longitudinal lattice depth for $K = 0$. B_0^+ and B_0^- are plotted for $V_0^\perp = 15$ (dashed curves) and $V_0^\perp = 30$ (solid curves). In the example $\Delta\mu$ is positive so both B_0^\pm -curves lie above their respective B_0^- -curves. The left axis shows B_0^\pm relative to the Feshbach resonance position in the absence of the lattice, and the right axis shows the actual magnetic field position for the specific Feshbach resonance considered [82]. The black dash-dotted curves are given by Eq. (4.28).

As shown in Sec. 4.5.2 the divergence of the lattice scattering length is associated with a bound state entering or leaving the continuum. Hence the lattice gives rise to a K -dependent shift of the magnetic field threshold for the formation of two-body bound states away from the resonance position in free space. This fact, illustrated in Fig. 4.16, was also observed by Orso *et al.* [86] who solved the two-body physics in a one-dimensional optical lattice within a single-channel model. The zero-crossing of the scattering length occurs for $E_{\text{res}} = \pm|E_K|$, which corresponds to magnetic field values, $B_0^\pm - \mathcal{W}^2/(U\Delta\mu)$.

4.4.4 Sweep experiment

At a given energy inside the band the Feshbach molecules are unstable with dissociative decay width $\hbar\Gamma(E, K)$ given above. For a diabatic sweep of the magnetic field across resonance, starting with the resonance energy tuned below the band, the molecular population follows a simple rate equation,

$$dm/dt = -\Gamma(E(t))m(t), \quad (4.29)$$

provided the sweep is fast enough that recombination may be neglected. For a linear sweep, where $dE/dt = \Delta\mu\dot{B}$, the remaining molecular fraction can be

found analytically as a function of the energy inside the band:

$$m(E) = \exp \left\{ -2\alpha \left[\sin^{-1} E/|E_K| + \pi/2 - C \left(\tan^{-1} \frac{CE/|E_K|}{\sqrt{1-(E/E_K)^2}} + \pi/2 \right) \right] \right\}, \quad (4.30)$$

where $\alpha = \mathcal{W}^2/\Delta\mu\dot{B}\hbar$ and $C = \sqrt{\beta_K^2/(1+\beta_K^2)}$ with $\beta_K = U/E_K$. A unique feature of the lattice system, is that the continuum has an upper edge, and above that edge the molecules are again stable. The fraction of stable molecules after a magnetic field sweep of E_{res} from below to above the continuum band has the simple form

$$\chi \equiv m(|E_K|) = \exp \left[-2\pi\alpha \left(1 - \sqrt{\frac{\beta_K^2}{1+\beta_K^2}} \right) \right], \quad (4.31)$$

depending only on the two constants α and β_K . This expression is plotted in the left hand panel of Fig. 4.12 for $U = 1.4J$.

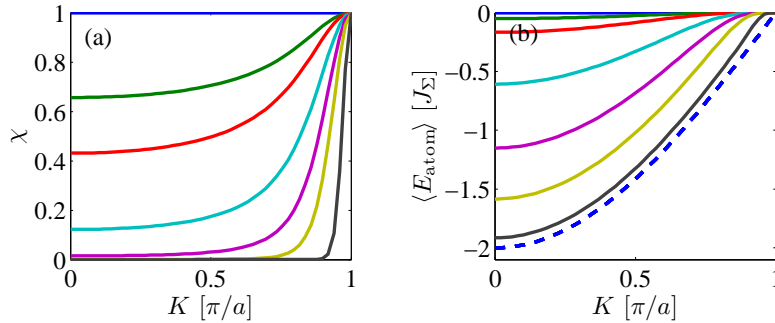


Figure 4.12: Remaining molecule fraction after a linear sweep through the band (left) and average dissociation energy per atom (right) for $\alpha=0, 0.1, 0.2, 0.5, 1, 2, 10$ (from above). For fast ramps all molecules survive, but as the ramp speed is decreased more molecules decay and the dissociation energy approaches half the lower band edge (dashed line).

We first observe that in the limit $\alpha \rightarrow 0$, corresponding to sweeps instantaneous on the time scale set by the coupling, the molecules are left intact. We note that the molecules are also left intact when the parameter β_K diverges. This happens in (i) the limit $U \rightarrow \pm\infty$, where the scattering states are repealed from $z = 0$, *i.e.*, $|\psi_K(0)| \rightarrow 0$, or (ii) in the limit of $K \rightarrow \pm\pi/a$ in which case the continuum width $|E_K|$ vanishes. However, the latter is an artifact of omitting tunneling beyond nearest neighbor. As more distant tunneling amplitudes are incorporated the band widens at the zone boundary, as we will see in Chap 6. Furthermore, we note that Eq. (4.31) is of the Landau-Zener

form with $\tilde{\alpha} = \alpha(1 - \sqrt{\beta_K^2/(1 + \beta_K^2)})$ playing the role of the adiabaticity parameter [87]. Finally, we see that χ is *independent* of the sign of U . This is a property inherited from $|\psi_K^{\text{op}}(0)|$.

The average energy of the dissociated atoms can be found as

$$\langle E_{\text{atom}} \rangle = -\frac{1}{2} \int_{-|E_K|}^{|E_K|} E \, d[m(E)]. \quad (4.32)$$

This integral has in general to be computed numerically and the result is shown in the right panel of Fig. 4.12. As a smaller fraction of the molecules survive the passage through the band the dissociation energy per atom approaches half the lower band edge, $-|E_K|/2 = -2J \cos(Ka/2)$. Molecule dissociation energies have been measured in free space [72, 88], and the energy distribution after the sweep through the energy band may be identified by studying the ballistic expansion of the gas after the atoms are released from the lattice on a time scale, admitting adiabatic mapping of the quasi-momentum states to plane wave momentum states.

It is instructing to have a closer look at the case of vanishing background interaction, $U = 0$. Here the survival probability assumes the Landau-Zener form, $\chi \equiv \exp(-2\pi\alpha)$, in which α plays the role of the adiabaticity parameter [87], and the average dissociation energy can in this case be calculated analytically; $\langle E_{\text{atom}} \rangle = -f(\alpha)E_K/2$, where $f(\alpha) = 4\alpha^2(1 + e^{-2\alpha\pi})/(1 + 4\alpha^2)$ only depends on the adiabaticity parameter. We observe that $\langle E_{\text{atom}} \rangle \rightarrow 0$ in the limit $\alpha \rightarrow 0$ as should be expected, since almost all molecules survives, and therefore, both Γ and $m(E)$ in Eq. (4.29) is constant across the continuum. In the opposite limit, $\alpha \rightarrow \infty$, almost all molecules disintegrate at the continuum boundary, *i.e.*, $\langle E_{\text{atom}} \rangle \rightarrow -|E_K|/2$, in agreement with the above findings.

4.5 Bound states

The bound state solutions of the coupled-channels problem have energies, E_b , coinciding with the poles of the scattering amplitude $f(E, K)$. The pole locations satisfy the equation

$$\left[\sqrt{E_b^2 - E_K^2} - U \text{sgn}(E_b) \right] = \frac{\mathcal{W}^2 \text{sgn}(E_b)}{E_b - E_{\text{res}}(B, K)}, \quad (4.33)$$

and can be determined as a subset of the roots of a quartic polynomial. The bound state energies are plotted as the solid lines in Figs. 4.13(a)-(d) and 4.14(a)-(b). If $\mathcal{W} = 0$, E_b reduces to the entrance channel bound state energy, $E_b^0 = \text{sgn}(U) \sqrt{U^2 + E_K^2}$. This single-channel bound state is indicated for reference by the sinusoidal dashed lines in Fig 4.13(a)-(d) and the horizontal dashed line in Fig. 4.14(a)-(b).

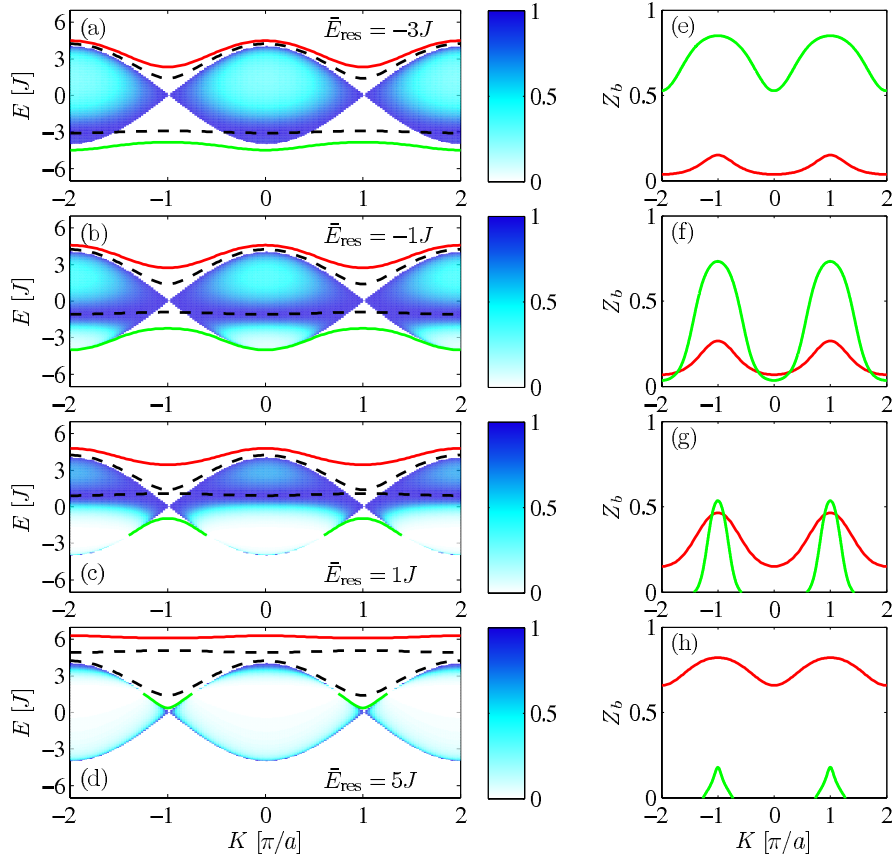


Figure 4.13: (a)-(d) Scattering properties and bound states in an extended zone scheme at different values of the resonance energy. The colormap inside the band illustrates the reflection probability, $R(E, K)$, ranging from 0 (white) to 1 (dark blue). The solid lines are the bound state energies of the coupled system, while the dashed curves indicate the diabatic, uncoupled bound states with the nearly horizontal line giving E_{res} and the other corresponding to the uncoupled dimer state E_b^0 , Eq. (3.42). (e)-(h) Closed channel population of the bound states, Eq. (4.43). Plots are shown for resonance energies $\bar{E}_{\text{res}} = -3J$ (a,e), $-J$ (b,f), J (c,g), and $5J$ (d,h).

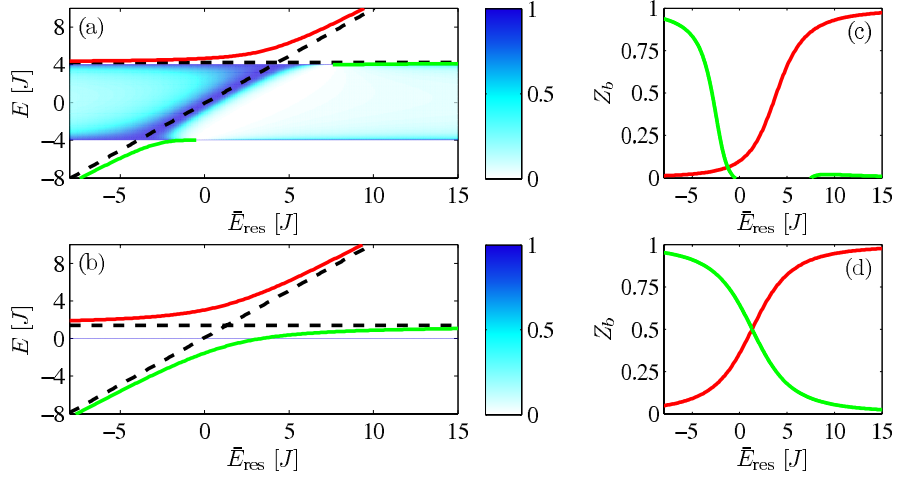


Figure 4.14: (a)-(b) Bound state energies (solid lines) and reflection coefficient across the continuum band (colormap) as a function of \bar{E}_{res} for $K = 0$ (a) and $K = \pm\pi/a$ (b). The horizontal dashed line is the repulsively bound pair state existing above the band for $\mathcal{W} = 0$, while the diagonal dashed curve is the band-averaged resonance energy, \bar{E}_{res} . (c)-(d) Closed channel population of the bound states.

4.5.1 Pair tunneling

Like in the single-channel case we can determine an effective tunnel amplitude for the dimers directly from the dispersion of their binding energy, when the atomic tunneling is small compared to the bound state energy.

In the absence of the atomic tunneling process, *i.e.*, $J = 0$ and $E_K = 0$ for all K , the energies of the bound states are given by

$$E_b^{[E_K=0]} = \frac{\bar{E}_{\text{res}}(B) + U}{2} \pm \sqrt{\frac{[\bar{E}_{\text{res}}(B) - U]^2}{4} + \mathcal{W}^2}. \quad (4.34)$$

With the inter-channel coupling turned off these zero-tunneling bound state energies reduce to the uncoupled pair state energies; \bar{E}_{res} and U . With a small non-vanishing single-particle tunneling amplitude we may expand (4.33) to lowest order in $|E_K|$ and find

$$E_b \approx E_b^{[E_K=0]} + \frac{E_K^2}{2E_b^{[E_K=0]}} \quad (|E_K| \ll |E_b|). \quad (4.35)$$

If we compare the quasi-momentum dependent part of the binding energy with the single particle dispersion, $E_{\text{pair}} = -2J_{\text{pair}} \cos(Ka)$, we find the effective tunneling rate

$$J_{\text{pair}} = -\frac{2J^2}{E_b^{[E_K=0]}}. \quad (4.36)$$

Note that we have neglected the molecular tunneling rate J_m , because it is much smaller than J . Depending on the resonance energy, Eq. (4.34) features one or two solutions, which gives rise to two different effective tunneling amplitudes. In the far detuned limit, $\bar{E}_{\text{res}}(B) \rightarrow \pm\infty$, J_{pair} vanishes for the state dominated by the bare resonance state, *i.e.*, the state with $Z_b \simeq 1$, because the atoms cannot move independently and J_m will dominate, meanwhile the effective pair tunneling of the other state with $Z_b \simeq 0$ approach the single-channel value, $J_{\text{pair}} = -2J^2/U$.

The pair tunneling was measured in Ref. [19], where two atoms were prepared on the same site in a double well and the oscillation frequency of the average atomic positions in the double well were measured. Our calculations suggest that tuning E_{res} will give two competing (three if we count the bare atomic oscillations given by J/h) and with magnetic field tunable oscillation frequencies, J_{pair}/h , in such an experiment.

4.5.2 Binding energy

Instead of the bound state energy it is often instructive to consider the *binding energy*, defined as the distance of the bound state energy from the (upper or lower) band edge:

$$E_{\text{bind}} = E_b - \text{sgn}(E_b)|E_K|. \quad (4.37)$$

The binding energy is indicated by black arrows in Fig. 4.15. It is positive for a bound state lying above the band and negative for a bound pair below the continuum. From Fig. 4.13(a)-(d) we observe that the binding energy increases with increasing $|K|$ in agreement with the single-channel calculation in Ref. [86], which only discussed bound states with negative binding energy as no transverse confinement was included.

As E_b approaches either of the band edges, the binding energy vanishes in a particularly simple way. To see this we observe that $E_b^2 - E_K^2 \approx 2 \text{sgn}(E_b)|E_K|E_{\text{bind}}$ for $E_{\text{bind}} \rightarrow 0$. Inserting this and replacing E_b with $\text{sgn}(E_b)|E_K|$ in the denominator on the right hand side of Eq. (4.33), it then follows that

$$E_{\text{bind}} \approx \frac{\text{sgn}(E_b)U^2/2|E_K|}{\left[1 + \frac{\mathcal{W}^2/U}{E_{\text{res}}(B,K) - \mathcal{W}^2/U - \text{sgn}(E_b)|E_K|}\right]^2}, \quad (4.38)$$

as the bound state energy approaches $\text{sgn}(E_b)|E_K|$. The denominator is exactly the resonance shape of the generalized scattering length (4.25), and the binding energy therefore approaches the universal form

$$E_{\text{bind}} = -\frac{\hbar^2}{2\mu_K^*(a_{\text{1D}}^\pm)^2}, \quad (4.39)$$

when the scattering length is tuned to be large with respect to the lattice spacing a in the vicinity of the Feshbach resonance. The effective reduced mass μ_K^* , introduced in Eq. (3.44), is evaluated at $k = \pm\pi/a$ and $k = 0$ for the repulsively and attractively bound states, respectively. The criteria of applicability for the quadratic approximation is $|E_{\text{bind}}| \ll \min(|E_K|, \mathcal{W}^2/U)$, or

$|\delta^\pm| \ll \sqrt{2|E_K|}\mathcal{W}^3/|U|^{5/2}$. The universal expression (4.39) is compared with the exact binding energies in Fig. 4.16 both above and below the continuum. Due to the proximity of the zero crossing of a_{1D}^- , where (4.39) diverges, the agreement below the band is limited to a smaller region.

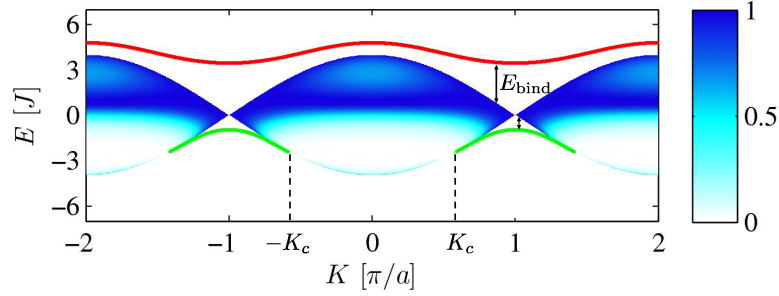


Figure 4.15: Bound states and scattering continuum for $\bar{E}_{\text{res}} = 1J$. The arrows indicate the binding energies for the bound states and the dashed lines mark $K = \pm K_c$, which delineate the region with only one bound state, see text for details.

4.5.3 Motionally bound states

An important consequence of the structured continuum in the lattice potential is that the stability of a molecular bound state may depend on its center-of-mass momentum. For a range of magnetic field values, the resonance state only exists in an interval of center-of-mass quasi-momentum states, as shown in Fig. 4.13(c)-(d) [89]. Outside this range there is instead a true bound state of the system. Such *motionally* bound states are stabilized by their kinetic energy, which displaces the pair state into the band gap for the relative motion, where the pair cannot disintegrate. Hence, for a fixed magnetic field, where

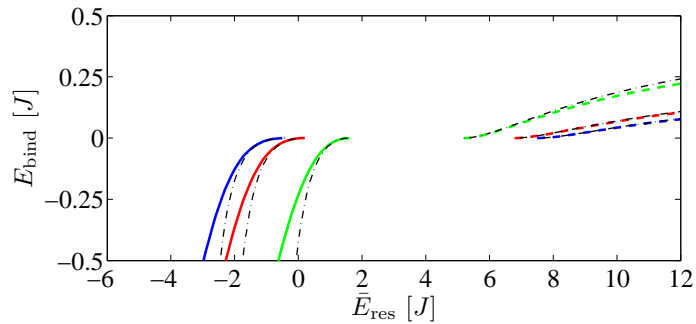


Figure 4.16: The binding energies below the band (solid lines) and above the band (dashed lines) and the limiting form (4.39), valid near the Feshbach resonances in a_{1D}^\pm (thin dot-dashed lines).

a molecule at rest is unstable, accelerating the lattice provides a new avenue for tuning a Feshbach resonance.

From Eqs. (4.25) and (4.39) it is clear that the binding energy vanishes when $E_{\text{res}} = \mathcal{W}^2/U \pm |E_K|$. We note that this condition for the disappearance of the Feshbach bound state coincides with the critical resonance energy at which the Fano profile develops a point of total transmission, Eq. (4.20).

Ignoring the small modulation of the resonance energy due to tunneling of the bare molecules, the Feshbach molecules are stable bound states of the system if their center-of-mass quasi-momentum in the first Brillouin zone satisfies $|K| > K_c$, where

$$K_c = \frac{2}{a} \cos^{-1} \left(\frac{|\bar{E}_{\text{res}}(B) - \mathcal{W}^2/U|}{4J} \right). \quad (4.40)$$

If $|K| < K_c$ the pair state lies inside the continuum and decays with a rate $\Gamma(E, K)$, which we have determined analytically above. For magnetic fields such that $|\bar{E}_{\text{res}}(B) - \mathcal{W}^2/U| > 4J$ the Feshbach molecules are stable for all K . In Fig. 4.15 $\pm K_c$ is indicated by dashed lines marking the region with only a single bound state.

Given the existence of motionally bound states, an alternative experiment to investigate the passage of a molecule through the continuum may then be conducted by starting with the applied magnetic field held at a value such that $4J < |E_{\text{res}} - \mathcal{W}^2/U|$, and molecules at rest prepared in the bound state with energy below \bar{E}_{res} (represented by the the lower branch of bound states in Figs. 4.13 and 4.14). Accelerating the lattice imparts momentum K_i to the molecules. If the magnetic field is then ramped adiabatically to a new value, where $|E_{K_i}| < |E_{\text{res}} - \mathcal{W}^2/U| < 4J$ the moving molecules remain stable, while molecules at rest are now subject to dissociative decay. With a further acceleration of the lattice, either in the opposite direction, or in the same direction, but letting K cross one or several Brillouin zones, the molecules may be swept through the continuum to a final state with center-of-mass momentum K_f , where the molecules are stable provided $|E_{K_f}| < |E_{\text{res}} - \mathcal{W}^2/U|$. The probability of a molecule surviving the center-of-mass momentum ramp through the continuum depends on the rate of lattice acceleration and the strength of the coupling to the continuum states.

4.5.4 Bound state wave functions

The formal solution of the bound state problem consistent with the single-pole approximation for the closed channel Green's function is

$$\begin{pmatrix} |\psi_b^{\text{op}}\rangle \\ |\psi_b^{\text{cl}}\rangle \end{pmatrix} = \sqrt{Z_b} \begin{pmatrix} \hat{G}_K^U(E_b, z) \hat{W} |\phi_{\text{res}}\rangle \\ |\phi_{\text{res}}\rangle \end{pmatrix}, \quad (4.41)$$

where the closed channel population, Z_b , is determined by the normalization condition: $\langle \psi_b^{\text{op}} | \psi_b^{\text{op}} \rangle + \langle \psi_b^{\text{cl}} | \psi_b^{\text{cl}} \rangle = 1$. In coordinate space the open channel component of the bound state wave function therefore becomes

$$\psi_b^{\text{op}}(z) = \sqrt{Z_b} \mathcal{W} G_K^U(E_b, z). \quad (4.42)$$

The closed-channel weight of a bound atom pair with energy E_b is

$$Z_b = \left[1 + \frac{\mathcal{W}^2}{[1 - UG_K^0(E_b, 0)]^2} \frac{|E_b|}{(E_b^2 - E_K^2)^{3/2}} \right]^{-1}, \quad (4.43)$$

which is plotted in Figs 4.13(e)-(g) and 4.14(c)-(d). As the bound state approaches the upper or the lower band edge, it follows from the limiting form of the binding energy that $E_b^2 - E_K^2 \approx E_K^2 (a/a_{1D}^\pm)^2$, and consequently Z_b vanishes as $(U/\mathcal{W})^2 |a/a_{1D}^\pm|$ in the limit where $|a_{1D}^\pm/a| \gg 1$.

In momentum space the open channel part of the bound state wave function is given by

$$\phi_b^{\text{op}}(k) = \sqrt{\frac{aZ_b}{2\pi}} \mathcal{W} \frac{\mathcal{G}_K^0(E_b, k)}{1 - UG_K^0(E_b, z=0)}. \quad (4.44)$$

We observe that the open channel part of the wave functions have the same characteristics as in the single channel case, *i.e.*, we can discern states below and above the continuum on account of the quasi-momentum spectrum, which is peaked at either the center or the boundaries of the Brillouin zone, respectively.

The size of the bound state

$$\langle |z| \rangle = \frac{a}{2} \frac{Z_b \mathcal{W}^2}{[1 - UG_K^0(E_b, 0)]^2} \frac{E_K^2}{(E_b^2 - E_K^2)^2}, \quad (4.45)$$

reflects the magnitude of the binding energy of atom pairs. In particular, it diverges when the bound state enters the continuum from above or from below:

$$\langle |z| \rangle \rightarrow \frac{|a_{1D}^\pm|}{2} \quad \text{for } |a_{1D}^\pm| \rightarrow \infty. \quad (4.46)$$

In this limit the open-channel part of the bound state wave function assumes a universal form

$$\psi_b^{\text{op}}(z) \rightarrow \sqrt{\left| \frac{a}{a_{1D}^\pm} \right|} e^{-|z/a_{1D}^\pm|} [-\text{sgn}(E_b)]^{z/a}. \quad (4.47)$$

The bound state wave functions are shown in Fig. 4.17 in both coordinate and momentum space for $\bar{E}_{\text{res}} = -J$. At this resonance energy a bound molecular state exists just below the band for $K = 0$ (lower bound state branch in Fig. 4.13(b)). With a small binding energy, this state extends over several lattice sites as shown in Fig 4.17. For the repulsively bound pair state lying above the band (upper bound state branch in Fig. 4.13(b)) the sign of the coordinate space wave function alternates between lattice sites. This is a feature inherited from the entrance-channel Green's function for energies above the continuum, Eq. (3.17), as was also discussed for the single-channel bound state in Chap. 3.

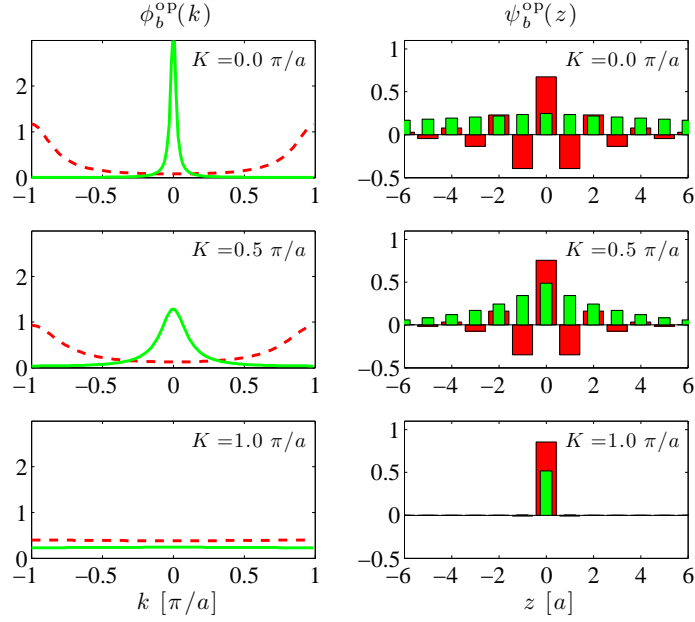


Figure 4.17: Open channel components of bound state wave functions for $\bar{E}_{\text{res}} = -J$, where a weakly bound molecular state (solid line, narrow bars) at rest is situated just below the band. The repulsively bound pair state lying above the band (dashed line, thick bars) is peaked at the edge of the Brillouin zone, and its sign alternates from one site to the next [cf. Fig. 3.4]. The first column shows the momentum space wave function (4.44) in units of $\sqrt{a/2\pi}$, the second column $\psi_b^{\text{op}}(z)$.

4.6 Spectral analysis

When we have two coupled channels there is a spectral density for both the open channel atoms and the closed channel molecules. We start by addressing the latter.

4.6.1 The closed channel

The dressed Green's function for the closed channel is found by summing all the terms in the Dyson series based on the bare propagator (4.5). The result is

$$G_M(E, K) = \frac{1}{E - E_{\text{res}}(B, K) - \Sigma_M(E, K)}, \quad (4.48)$$

where $\Sigma_M(E, K) = \mathcal{W}^2 G_K^U(E, 0)$ is the molecular self-energy [Eq. (4.16)]. If E is outside the continuum, $\Sigma_M(E, K)$ is real, and the spectral function is only non-zero at the poles of G_M , which coincide with those of the scattering amplitudes, *i.e.*, the bound states of the coupled channels problem, Eq. (4.33). The spectral weight at the poles is given by the corresponding residues, which

are just the probability of finding the bound state pair in the closed channel, Z_b :

$$A_M(E, K) = 2\pi Z_b \delta(E - E_b). \quad (4.49)$$

For energies inside the continuum, we obtain the usual structure,

$$A_M(E, K) = \frac{\hbar\Gamma(E, K)}{[E - E_{\text{res}}(B, K) - \Delta(E, K)]^2 + \frac{\hbar^2\Gamma^2(E, K)}{4}}, \quad (4.50)$$

where the energy dependent shift, Δ , and decay rate, Γ , are defined in Eqs. (4.17) and (4.18), respectively. In the middle of the band the shift and width are slowly varying functions of energy, and the molecular spectral function has an approximately Lorentzian shape with a peak position given approximately by the resonance energy E_{res} . However, near the band edges significant deviations from this simple form arise due to the strong interference with the continuum threshold. This leads to a double peak structure of A_M , when the bound state is about to enter the continuum from below, as is evident from Fig. 4.18, which shows A_M as a function of the energy and E_{res} for a molecule at rest.

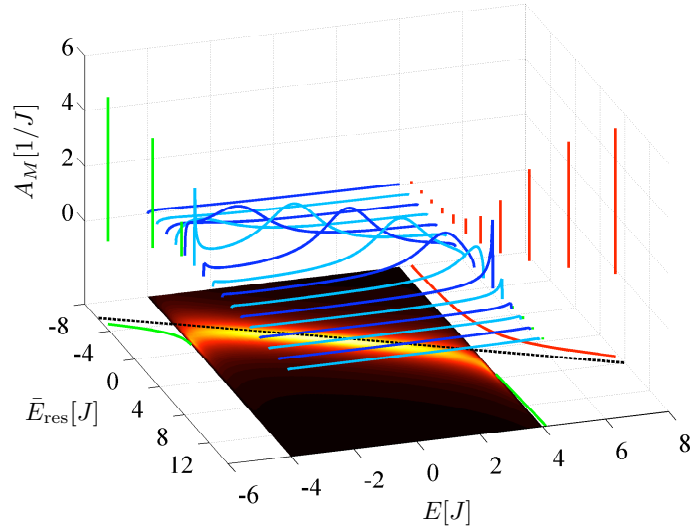


Figure 4.18: Molecular spectral function as a function of the resonance energy for $K = 0$. Inside the band A_M is a continuous function given by Eq. (4.50). Outside the band the delta function peaks at the bound state poles of the propagator, G_M , are indicated by vertical lines with a height of $2\pi Z_b/J$. Offset below is a contour plot of A_M inside the band, with bright colors indicating high spectral density. The solid lines in this plane are the bound state energies, while \bar{E}_{res} is indicated by the dashed line.

We remind ourselves that the molecule lifetime also follows from Fermi's golden rule,

$$\Gamma(E) = 2\pi |\langle \phi_{\text{res}} | \hat{W} | \psi_K^{\text{bg}} \rangle|^2 D_K(E) = 2\pi \mathcal{W}^2 |\psi_K^{\text{bg}}(0)|^2 D_K(E), \quad (4.51)$$

Though the density of states diverges at the edges of the continuum (van Hove singularities) the decay rate goes to zero at both thresholds, due to vanishing overlap of the background scattering state with the bare resonance state when $E = \pm|E_K|$.

4.6.2 The open channel

For the open channel the full Green's function in the two-channel case reads

$$G_K(E; z, z') = G_K^0(E, z - z') + \frac{G_K^0(E, z)\Sigma_K(E, B)G_K^0(E, -z')}{1 - \Sigma_K(E, B)G_K^0(E, 0)}, \quad (4.52)$$

where $\Sigma_K(E, B) = U + \mathcal{W}^2/[E - E_{\text{res}}(B, K)]$ is the self-energy for the relative motion of an atom pair in the open channel. This gives the spectral function

$$A_K^{\text{op}}(E, z) = 2\pi Z_b [\mathcal{W}G_K^U(E, z)]^2 \delta(E - E_b) \quad (4.53)$$

for energies outside the band. The open channel Green's functions has exactly the same poles as the molecular propagator (4.48), but the residues at the atomic poles depend on the separation between the atoms in the pair. However, using the identity $\sum_{z \in \mathbb{Z}} e^{-2\kappa|z|} = EG_K^0(E, 0)$ one may show that

$$\sum_{z \in \mathbb{Z}} A_K^{\text{op}}(E, z) = 2\pi (1 - Z_b) \delta(E - E_b), \quad (4.54)$$

such that the combined spectral weight of the open channel and closed channel at a pole is unity. We must sum over all possible separations for the open-channel weight, since the component of the bound state wave function in the open channel is distributed over the lattice, according to (4.42).

4.7 Inclusion of higher Bloch bands

Thus far we have only investigated the dynamics in the lowest Bloch band of the lattice potential. In this section we analyze the neglected coupling to higher bands. First we estimate the size of the second order energy shift from the excluded higher bands and derive a criterion for the validity of our theoretical model. Next, in Sec. 4.7.3 we discuss how a modest coupling to higher atomic bands is expected to modify the central conclusions of this work.

4.7.1 Generalized coupling elements

In Sec. 3.3 and 4.3 we only considered the matrix elements for the first Bloch band of the interactions \hat{W} and \hat{U} . To investigate the effect of higher Bloch bands we will need to generalize this to the matrix elements between atomic bands n and m and a molecule in band l . The generalization is, however, straightforward.

The on-site interaction between a pair of atoms in bands n and m becomes

$$U_{nm} = g_{\text{bg}} \prod_{i=1,2} \int dx_i [w_{10}^\perp(x_i)]^4 \times \int dx_3 [w_{n0}^\parallel(x_3)w_{m0}^\parallel(x_3)]^2, \quad (4.55)$$

and the on-site coupling of the same pair of atoms to a bare molecular state in band l is

$$\mathcal{W}_{lnm} = g \prod_{i=1,2} \int dx_i w_{10}^{\text{cl},\perp}(x_i)w_{10}^\perp(x_i)^2 \times \int dx_3 w_{10}^{\text{cl},\parallel}(x_3)w_{n0}^\parallel(x_3)w_{m0}^\parallel(x_3). \quad (4.56)$$

The latter is zero whenever $l + n + m$ is even due to parity of the Wannier functions. We still assume that only the lowest band in the transverse lattice is occupied.

From a simple norm argument we can estimate the significance of the coupling to higher molecular bands. We start by observing that the molecular Wannier states, $\prod_{i=1,2,3} w_{n_i j_i}^{\text{cl},i}(x_i)$, where n_i and j_i refers to the molecular Bloch band index and lattice site index along direction i , respectively, constitute a complete set on which we can expand the ‘‘atomic pair’’ function $f(\mathbf{x}) = \prod_{i=1,2} [w_{10}^\perp(x_i)]^2 \times w_{n0}^\parallel(x_3)w_{m0}^\parallel(x_3)$. Denoting the expansion coefficients by $c_{n_1 n_2 n_3}^{j_1 j_2 j_3}$, the coupling is $\mathcal{W}_{lnm} = g c_{111}^{000}$, whereas the inter-band interaction is $U_{nm} = g_{\text{bg}} \|f\|^2$, where $\|\cdot\|^2$ is the L^2 -norm. From the L^2 -norm we now get the following identity for the neglected molecular couplings to higher bands

$$g^2 \sum_{\substack{j_1 j_2 j_3 \\ (n_1 n_2 n_3) \neq (111)}} |c_{n_1 n_2 n_3}^{j_1 j_2 j_3}|^2 = \frac{g^2 U_{nm}}{g_{\text{bg}}} - |\mathcal{W}_{1nm}|^2, \quad (4.57)$$

where $g^2/g_{\text{bg}} = \Delta\mu\Delta B = 0.6E_R$ for the 414 G resonance in ^{87}Rb . For a lattice with $V_0^\parallel = 1$ and $V_0^\perp = 30$ this results in the estimate $\sum_{l \neq 1} |\mathcal{W}_{l11}|^2 \leq 0.0059 \mathcal{W}_{111}^2$ for an atom pair in the lowest band ($n = m = 1$).

4.7.2 Validity of the lowest band approximation

We now set up a criterion for using our discrete two-channel theory by comparing the second order energy shift from the omitted atomic and molecular excited Bloch bands to the relevant energy scales. The dominant contribution to the energy shift comes from the bare resonance state coupling to atom pairs in higher bands, while the shift from open-channel atoms coupling to higher molecular Bloch bands are several orders of magnitude smaller for two reasons. Firstly, the coupling matrix elements between an atom pair in the lowest band and an excited band bare molecule are much smaller than the coupling to a molecule in the lowest band as discussed above. Secondly, the energy splitting between the ground and excited molecular bands is larger than the atomic band gaps, since the molecules experience a deeper lattice potential, as discussed in Sec. 2.4. Therefore we approximate the unperturbed wave function

by $|\phi_{\text{res}}\rangle$, the resonance state in the lowest molecular band. For simplicity we will furthermore assume the width of the Bloch bands to be small compared to the separation from the lowest band, so that the energy can be approximated by the average energy of the band.

Under these assumptions the second order energy shift is

$$\Delta E^{(2)} = - \sum_{(n,m) \neq (1,1)} \frac{|\mathcal{W}_{1nm}|^2}{E_n + E_m - 2E_1}, \quad (4.58)$$

where the sum is over pairs of atoms in the n 'th and m 'th Bloch band, and E_n is the average energy of the n 'th band. If the atoms are indistinguishable bosons, we can take the sum to be over $n \leq m$ to avoid double counting.

We will require the shift to be small compared to the relevant energy scales. If $\Delta E^{(2)}$ is comparable to the gap between the ground and first excited band $2(E_2 - E_1)$, the higher bands will become populated, and the lowest band approximation of our model will break down [90]. On the other hand a stronger condition can be derived by requiring the energy shift to be small compared with the width of the ground band, $8J$, which sets the relevant energy scale for the dynamics in our model. By fitting the respective energies from numerical band structure calculations at different lattice depths we arrive at the condition

$$\left(\frac{a_{\text{bg}}}{100 a_B} \right) \left(\frac{\Delta\mu}{\mu_B} \right) \left(\frac{\Delta B}{1\text{G}} \right) \left(\frac{m}{\text{amu}} \right) \left(\frac{\lambda_L}{1000\text{nm}} \right) \ll \frac{Q(V_0^{\parallel})}{(V_0^{\perp})^{0.6}}, \quad (4.59)$$

where $Q(V_0^{\parallel}) = 30(V_0^{\parallel} + 4)$ when comparing $\Delta E^{(2)}$ with the band gap, and $Q(V_0^{\parallel}) = 60 \exp(-0.2V_0^{\parallel})$ when requiring the energy shift to be much smaller than the width of the lowest band¹. The scaling factors are the Bohr radius, a_B , the Bohr magneton, μ_B , Gauss (G), the atomic mass unit (amu), and nanometers. If both criteria are met, coupling to higher bands can be safely neglected. Otherwise, if the energy shift incurred from the coupling to atoms in higher Bloch bands is significant with respect to the band width yet negligible with regards to the band gap, we might expect quantitative changes to our results, but as we discuss below, the qualitative features of our model will remain. In the case where the lowest band approximation fails, coupling to higher bands can be systematically accounted for in the tight binding limit [91–93], leading to an effective single-band Hamiltonian with a non-local coupling between dressed molecules and unbound atom pairs [94].

Both conditions above are fulfilled for the 414 G resonance in ^{87}Rb used in our examples [82]. In the entrance channel both atoms are in the $|F = 1, m_F = 0\rangle$ hyperfine state. The resonance is narrow, with $\Delta B = 18$ mG, and has a very small difference in magnetic moments between the two channels, $\Delta\mu = 111$ kHz/G, which is preferable if Eq. (4.59) is to hold.

¹The fit was performed for $1 \leq V_0^{\parallel} \leq 15$ and $10 \leq V_0^{\perp} \leq 35$, and the sum in (4.58) was taken over the lowest 35 bands.

A final condition for our results to be experimentally relevant is that the variation of the resonance energy due to magnetic field noise δB_{rms} is much smaller than the bandwidth $8J$. With a lattice wavelength of 830.44 nm [82] the recoil energy is $E_R = 3.5$ kHz (equivalent to $0.16 \mu\text{K}$) and for the particular resonance considered here $E_R/\Delta\mu = 32$ mG. For a longitudinal lattice depth of $1E_R$ we therefore require $\delta B_{\text{rms}} \ll 46$ mG according to Table 4.1. In Ref. [72] the magnetic field noise was found to be less than 4 mG.

4.7.3 Corrections due to higher atomic Bloch bands

As discussed in the previous subsection the major correction to our model comes from the coupling to higher atomic bands. We now include these couplings into our model. For each atomic band we apply the analysis of Sec. 3.4 to obtain a set of band specific Green's functions $G_{K,n,m}^0(E, z)$ and $G_{K,n,m}^U(E, z)$ for the relative motion of one atom in Bloch band n and the other in band m . As for the first band, $\hat{G}_{K,n,m}^0(E)$ is the Green's function for noninteracting particles and $\hat{G}_{K,n,m}^U(E)$ is the Green's function for particles with an on-site interaction, $U_{nm}\delta_{z,0}$. We determine $G_{K,n,m}^0(E, z)$ and $G_{K,n,m}^U(E, z)$ by replacing $\epsilon_K(k)$ by $[-2J_{n1}\cos(Ka/2 + ka) - 2J_{m1}\cos(Ka/2 - ka) + E_n + E_m - 2E_1]$ in Eq. (3.14), and replacing U by the band specific interaction strength U_{nm} in Eq. (3.23).

We now introduce the coupling \hat{W} between the first molecular band and all the atomic bands. This gives the molecular self-energy

$$\begin{aligned}\Sigma'_M(E, K) &= \sum_{n,m} \langle \phi_{\text{res}} | \hat{W} \hat{G}_{K,n,m}^U(E) \hat{W} | \phi_{\text{res}} \rangle \\ &= \sum_{n,m} |\mathcal{W}_{1nm}|^2 G_{K,n,m}^U(E, 0),\end{aligned}\quad (4.60)$$

which reduces to (4.16), when we exclude contributions from higher bands. Because we only consider energies well outside the excited bands, $G_{K,n,m}^U$ is real and slowly varying with energy for $n, m \neq 1$. Therefore we conclude that the decay width Γ of the molecules is unchanged and that the change in the resonance shift $\Delta' = \text{Re}(\Sigma'_M - \Sigma_M)$ must vary slowly. Assuming that the change Δ' is constant we can incorporate this by replacing E_{res} by $E_{\text{res}} + \Delta'$, a renormalized resonance energy.

When $E = 0$ and $K = 0$ we obtain for the 414 G ^{87}Rb resonance an approximate relationship for the change in resonance shift

$$\Delta' \simeq -0.004 E_R (V_0^{\parallel})^{-0.1} (V_0^{\perp})^{0.6} \quad (4.61)$$

due to the higher atomic bands². For the lattice depth used throughout this paper Δ' is only 2% of the bandwidth $8J$, and it is reasonable to neglect higher bands.

²This fit was performed for $1 \leq V_0^{\parallel} \leq 35$ and $14 \leq V_0^{\perp} \leq 35$, and the contribution from the first 35 bands were included in (4.60).

We have assumed on-site interactions and only nearest-neighbor tunneling in all atomic bands which is a questionable assumption for the higher bands, but Eq. (4.61) still provides an estimate of the magnitude of the correction to the real part of the molecular self-energy.

Following Ref. [95] a direct coupling between ground and excited atomic bands may be included by renormalizing the local interactions to include the effect of virtual transitions to excited levels through band changing collisions. This leads to an energy dependent correction to the coupling parameters. But since the correction is inversely proportional to the gap separating the ground and excited bands, it is also expected to be small.

4.8 Conclusion

In this chapter, we have extended the discrete two-body model developed in Chap. 3 to include a resonance state in a closed-channel potential. We found that the transmission probability, which can be measured spectroscopically by a photodissociation experiment [Sec. 4.4.2], features a Fano profile [Eq. (4.15)]. The appearance of total transmission, we found, is limited to magnetic fields and center-of-mass quasi-momenta, for which the bare resonance state is inside the continuum. Furthermore, we found that in the extreme cases where either $U \rightarrow 0$ or $U \rightarrow \pm\infty$ the transmission or the reflection coefficient assumes a symmetric Breit-Wigner-like profile, respectively [Eqs. (4.21) and (4.22)].

In analogy with chapter 3 we derived a generalized scattering length, which diverges to plus and minus infinity when a bound state disappears into or emerges from the continuum, respectively [Sec. 4.4.3]. We further showed that in agreement with our free space intuition both the binding energy and the wave function of the resonance state are fully characterized by the generalized scattering length in the usual way, when the bound state is about to enter the continuum [Eqs. (4.39) and (4.47)].

We suggested a sweep experiment in which the molecules are scanned through the continuum by tuning the magnetic background field [Sec. 4.4.4]. The structured continuum offers the interesting possibility of scanning the molecules through the continuum to a stable region *above* the continuum. We found analytical expression for the survival probability, whereas the average energy of the dissociated atoms had to be found numerically, except for the special case of $U = 0$.

The energy of the bound states is no longer given by an explicit formula like in the single channel case, but instead by a quartic polynomial with at most two physically relevant roots [Eq. (4.33)]. The open-channel part of the wave function is, however, still proportional to $G_K^0(E, z)$ or $\mathcal{G}_K^0(E, k)$ in position and quasi-momentum representation, respectively. We obtained an effective pair tunneling J_{pair} for the bound states in analogy with the single-channel calculation, except we now find one for each bound state.

It is an interesting finding that the resonance state does not enter the continuum for the same resonance energy for all K . This led us to introduce the notion of motionally bound pairs, since for certain values of E_{res} the resonance

state may only be stable for $|K| > K_c$, where the critical center-of-mass quasi-momentum K_c is defined in Eq. (4.40). This opens up a new area for doing Feshbach physics, where molecules are created or dissociated by accelerating the lattice. One could also imagine a sweep through the continuum from one stable K -region to another.

The spectral analysis from Chap. 3 was extended to the two-channel situation, in which we get a spectral weight for each channel separately [Sec. 4.6]. We found that when the resonance state is inside the continuum the molecular spectral weight approached a structure reminiscent of a Lorentzian, whereas it shows a double peak structure when the resonance is just about to enter the continuum. Outside the continuum the weight vanishes except for divergences at the bound state energies. Here the spectral weight of the bound states is shared between the open and the closed channel reflecting the mixing induced by the coupling between the channels.

Finally, we generalized the on-site coupling \hat{W} and interaction \hat{U} to include matrix elements between arbitrary Bloch bands. This allowed us to (i) calculate a second order energy shift due to coupling to higher molecular and atomic Bloch bands, which we used to derive an equation for validity of the lowest band approximation [Eq. (4.59)], and (ii) include all the higher atomic bands in our model. The latter came down to introducing a renormalized resonance shift. The change in resonance shift were only 2% for the rubidium resonance we used in this chapter. The result rely on the assumption of on-site interaction and on the assumption of no coupling between atomic bands, which is questionable for the higher bands. Nonetheless, the simple method of Sec. 4.7.3 provides justification of the lowest band approximation.

Chapter 5

Heteronuclear atomic pairs

In recent years some of the focus has changed from experiments with a single atomic species to mixtures of different species [37, 96–103]. In this chapter, we accommodate this trend by extending the analysis of the previous chapters to cover atomic mixtures.

5.1 Introduction

Atomic mixtures add a new dimension to the Feshbach physics. First of all heteronuclear molecules can have permanent dipole moments, which gives rise to a long-range interaction ($V(r) \sim r^{-3}$) very different from the inherently short-ranged van der Waals interaction ($V(r) \sim r^{-6}$) between homonuclear molecules. This may have interesting consequences for Bose-Einstein condensates, but it may also be of importance in relation to quantum computing [104]. When aligned in an optical lattice the dipole force may act as a CNOT-gate between two particles in adjacent cells, *i.e.*, the particle acquires a phase shift which depends on the state of the atom in the neighboring lattice site. In Tab. 5.1 we list some of the recent experiments with heteronuclear Feshbach resonances.

Mixture	Ref.
${}^6\text{Li}$ and ${}^{23}\text{Na}$	[96]
${}^6\text{Li}$ and ${}^{40}\text{K}$	[97]
${}^6\text{Li}$ and ${}^{87}\text{Rb}$	[98, 99]
${}^{40}\text{K}$ and ${}^{87}\text{Rb}$	[37, 100, 101]
${}^{85}\text{Rb}$ and ${}^{87}\text{Rb}$	[99, 102]
${}^{87}\text{Rb}$, ${}^{174}\text{Yb}$ and ${}^{176}\text{Yb}$.	[103]

Table 5.1: List of atomic mixtures in recent experiments.

As will very soon become clear, the analysis of the previous chapters is readily generalized to account for heteronuclear pairs. For most of this chap-

ter we consider the single channel case, but at the end we briefly discuss the modification to the Feshbach problem for heteronuclear atom pairs. We will need to rephrase some of the formulas with slightly changed notation. However, the two-species atomic mixtures does show puzzling new features even in the absence of interactions.

5.2 Noninteracting atoms

The atoms will be labeled A and B and in general they will experience different lattice strengths so the optical lattice [Eq. (2.3)] is now species dependent:

$$V_{\text{lat},\beta}(\mathbf{x}) = \sum_{i=1,2} V_{\beta}^{\perp} E_{\text{R}} \sin^2(\pi x_i/a) + V_{\beta}^{\parallel} E_{\text{R}} \sin^2(\pi x_3/a). \quad (5.1)$$

Here $\beta = A, B$ is the atomic label. The difference in lattice strength can either come from different polarizability of the atoms or because the atoms are held in different, but aligned, laser fields. We apply the physical parameters relevant to the ^{40}K and ^{87}Rb mixture of Ref. [37], where the species are held by the same lattice, in our numerical examples. We take A to be ^{87}Rb and B to be ^{40}K with lattice strengths $V_{\text{A}}^{\parallel} = 3E_{\text{R,Rb}}$, $V_{\text{A}}^{\perp} = 40E_{\text{R,Rb}}$, and $V_{\text{B}}^i = 0.86V_{\text{A}}^i$, where $E_{\text{R,Rb}} = \hbar^2/2m_{\text{Rb}}\lambda_{\text{L}}^2$ is the recoil energy for rubidium.

The motion of each species is governed by the Hamiltonian

$$\mathcal{H}_0^{\beta} = -(\hbar^2/2m_{\beta})\nabla^2 + V_{\text{lat},\beta}(\mathbf{x}) \quad (5.2)$$

which separates. In this chapter, the transverse ground states have been approximated with the harmonic oscillator wave function

$$w(x) = (m\omega_{\beta}/\pi\hbar)^{1/4} \exp(-m\omega_{\beta}x^2/2\hbar) \quad (5.3)$$

with $\omega_{\beta} = (\pi/a)\sqrt{2V_{\beta}^3/m_{\beta}}$. This is only of relevance when obtaining the on-site interaction strength U and on-site coupling \mathcal{W} . Along the longitudinal direction, the dynamical tunneling amplitudes now depend on the species, *i.e.*, $J_{\beta} = \langle w_{nz_j}^{\beta} | \mathcal{H}_0^{\beta} | w_{nz_{j+1}}^{\beta} \rangle$, where $w_{nz_j}^{\beta}(x)$ is the Wannier functions, and again we only include nearest-neighbor tunneling and a single Bloch band ($n = 1$). In analogy with the previous two chapters, we model the two-body system by the wave function,

$$\Psi(x_A, x_B) = \sum_{z_A, z_B} \psi(z_A, z_B) w_{nz_A}^A(x_A) w_{nz_B}^B(x_B). \quad (5.4)$$

In this basis the two-body noninteracting Hamiltonian becomes

$$H_0 = -J_A(\Delta_{z_A} + 2) - J_B(\Delta_{z_B} + 2). \quad (5.5)$$

Still the eigenstates of H_0 are products of Bloch states

$$\psi(z_A, z_B) = \frac{a}{2\pi} \exp(iq_A z_A) \exp(iq_B z_B) \quad (5.6)$$

with energy

$$\epsilon(q_A, q_B) = E_A(q_A) + E_B(q_B), \quad (5.7)$$

where $E_\beta(q_\beta) = -2J_\beta \cos(q_\beta a)$ is the species dependent single particle energy dispersion.

We now change coordinates in the exact same way as in the previous chapters, except $Z = (z_A + z_B)/2$ and $K = q_A + q_B$ are no longer related to the center-of-mass motion and therefore we will refer to them as collective coordinate and collective quasi-momentum instead. The relative coordinate $z = z_A - z_B$ and quasi-momentum $k = (q_A - q_B)/2$ are unchanged.

The Hamiltonian still separates into a collective and a relative coordinate part via the Ansatz $\psi(z_A, z_B) = \sqrt{a/2\pi} e^{iKZ} \psi_K(z)$, due to the discrete nature of the model. The action of the Hamiltonian H_0 on the relative coordinate part ψ_K is given by

$$\begin{aligned} H_K^0 \psi_K(z) = & -J_A \left(e^{iKa/2} \psi_K(z+a) + e^{-iKa/2} \psi_K(z-a) \right) \\ & -J_B \left(e^{-iKa/2} \psi_K(z+a) + e^{iKa/2} \psi_K(z-a) \right). \end{aligned} \quad (5.8)$$

This should be compared to the simple expression for the identical particle case, $H_K^0 = \frac{1}{2} E_K(\Delta_z + 2)$, in Eq. (3.6). Unlike for identical atoms, where $J_A = J_B$, H_K^0 is not invariant under complex conjugation and hence is not time-reversal invariant, whenever $K \neq 0$. The collective quasi-momentum is here playing a role similar to that of a classical magnetic field on the motion of electrons in an atom or a solid. As a consequence of the breaking of the time-reversal symmetry, we cannot expect the bound state wave functions to be real, but in further analogy with the magnetic interactions we note that time reversal of the full two-body dynamics is accompanied by a change of sign of K . Therefore we have $H_K^0 = (H_{-K}^0)^*$, *i.e.*, if ψ_{-K} is an eigenstate of H_{-K}^0 then the complex conjugate, and hence time-reversed, wave function ψ_{-K}^* is an eigenfunction of H_K^0 with the same eigenvalue.

Introducing the average and half-difference tunneling amplitudes, $J_{\Sigma, \Delta} = (J_A \pm J_B)/2$, with values $J_\Sigma = J_A = J_B$ and $J_\Delta = 0$ in the case of identical particles, the energies (5.7) can be written in the convenient form

$$\begin{aligned} \epsilon_K(k) = & -2J_A \cos[(K/2 + k)a] - 2J_B \cos[(K/2 - k)a] \\ = & -4J_\Sigma \cos(Ka/2) \cos(ka) + 4J_\Delta \sin(Ka/2) \sin(ka) \\ = & E_K \cos[(T_K + k)a], \end{aligned} \quad (5.9)$$

which is parametrized by the collective energy

$$E_K = -4\sqrt{J_\Sigma^2 \cos^2(Ka/2) + J_\Delta^2 \sin^2(Ka/2)} \quad (5.10)$$

and by the quasi-momentum shift

$$\tan(T_K a) = \frac{J_\Delta}{J_\Sigma} \tan(Ka/2), \quad (5.11)$$

where $T_K a$ is taken in the interval $]-\pi/2, \pi/2]$ for $K a \in]-\pi, \pi]$. The collective energy plays the same role as the center-of-mass energy for the identical particle case. It determines the extremal values of the energy band for a fixed K when varying q , and therefore the total width of the band is $2|E_K|$. The continuum band is shown as the colored region in Fig. 5.1(a). For the Rb-K mixture and our choice of optical lattice parameters the tunneling amplitudes have the values $J_\Sigma = 0.5$ kHz and $J_\Delta = 0.5J_\Sigma$.

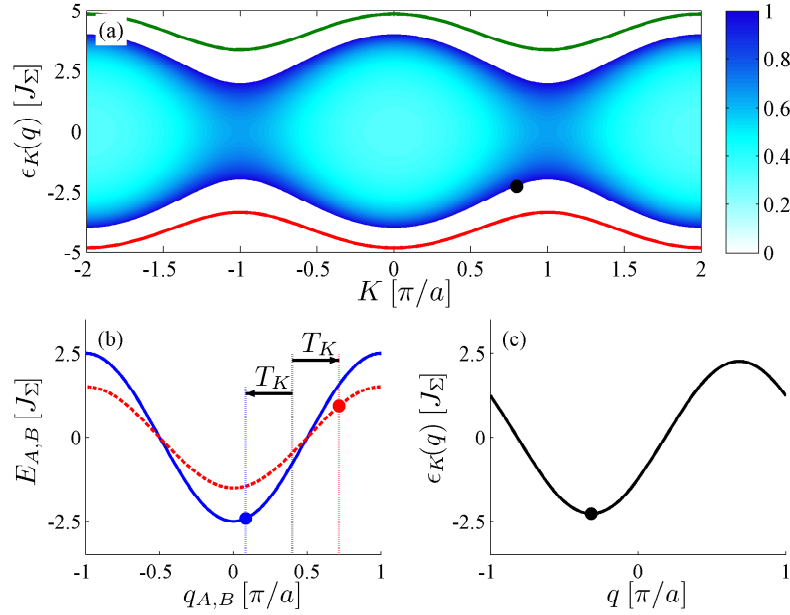


Figure 5.1: (a) Energy band spanned by $\epsilon_K(q)$ for the ratio $J_\Delta = 0.5J_\Sigma$, (b) the single atom spectra $E_\beta(q_\beta)$, and (c) the two-body spectrum $\epsilon_K(k) = E_A(K/2 + k) + E_B(K/2 - k)$ for $K = 0.8\pi/a$. The corresponding energy minimum $(K, q) = (0.8\pi/a, -T_K)$ is marked by dots in all three figures and the vertical lines in (b) indicate from left to right q_A , $K/2$ and q_B . The lower and upper curve in (a) show the bound state energy for $U = -2.7J_\Sigma$ and $U = 2.7J_\Sigma$, respectively, while the shading shows the reflection coefficient for $|U| = 2.7J_\Sigma$, see Eq. (5.20).

There are two significant differences from the identical particle case: (i) the width of the continuum band does not vanish for $K = \pi/a$, but maintains a finite width of $8|J_\Delta|$. For atom pairs with $K = 0$ the width of the band is $8|J_\Sigma|$. (ii) The minimum and maximum energies of the continuum are obtained for relative quasi-momenta $k = -T_K$ and $k = \pm\pi/a - T_K$, respectively, and not, as for identical particles, at relative quasi-momenta 0 and $\pm\pi/a$.

The finite quasi-momentum difference at the band edges, $q_A - q_B = -2T_K \pmod{2\pi/a}$, appears because the energy dispersions of the atoms have different amplitudes, $2J_\beta$. This is illustrated in Fig. 5.1(a)-(c), where the lowest energy state for $Ka/\pi = 0.8$ is marked by dots. The quasi-momenta of the

individual atoms are displaced by $\pm T_K$ from $K/2$.

The value of T_K is depicted in Fig. 5.2. T_K is an odd function of both K and J_Δ . In Fig. 5.2(a) the lower curve $J_\Delta/J_\Sigma = 0$ corresponds to $J_A = J_B$, the identical particle case, where $T_K = 0$ for all K because both atoms have the same energy dispersion, and the upper curve $J_\Delta/J_\Sigma = 1$ corresponds to $J_B = 0$, where only atom A is allowed to move, and therefore $q_A = K$, $q_B = 0$ and $T_K = K/2$. From Fig. 5.2(b) we note that $T_{K=0}$ is always zero, and whenever $J_A \neq J_B$, we have $T_{K=\pi/a} = \pi/2a$ due to the symmetry of the single particle dispersions.

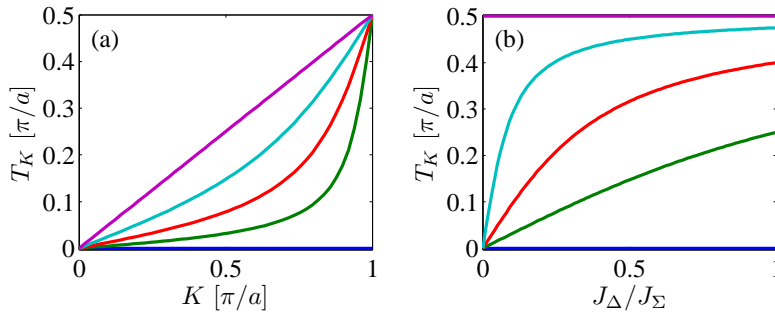


Figure 5.2: The quasi-momentum shift T_K . (a) From below $J_\Delta/J_\Sigma = 0, 0.1, 0.25, 0.5, 1$. (b) From below $Ka/\pi = 0, 0.5, 0.8, 0.95, 1$.

5.2.1 Alternative coordinates

In the above derivation we used a collective coordinate, K , which were defined in analogy with the center-of-mass coordinate for identical particles. However, we could also have chosen any coordinate set of the type: $\tilde{Z} = cz_A + (1-c)z_B$ and $\tilde{z} = z_A - z_B$ with $0 \leq c \leq 1$. Note that our choice of coordinates corresponds to $c = 0.5$. A product Ansatz $\psi(z_A, z_B) = \sqrt{a/2\pi} e^{i\tilde{K}\tilde{Z}} \psi_{\tilde{K}}(\tilde{z})$ is still possible, where the relative motion wave function can be expanded on $e^{i\tilde{k}\tilde{z}}$. Applying this Ansatz to the Bloch waves (5.6) we can identify $\tilde{K} = q_A + q_B = K$ in agreement with our previous definition, whereas the relative quasi-momenta are related as $k = \tilde{k} + (c - \frac{1}{2})K$.

If we insist on $\tilde{k} = 0$ being the ground state, we must require

$$0 = \frac{\partial}{\partial \tilde{k}} \left\{ E_A \left(cK + \tilde{k} \right) - E_B \left((1-c)K - \tilde{k} \right) \right\} \Big|_{\tilde{k}=0}. \quad (5.12)$$

It follows that [52]

$$\frac{J_A}{J_B} = \frac{\sin K(1-c)}{\sin Kc}. \quad (5.13)$$

Note that the parameter c has to be calculated for each K . Although the bound state solutions for $\psi_{\tilde{K}}(\tilde{z})$ may look simpler due to the missing T_K -phase, it has only been hidden in the \tilde{Z} -coordinate, and as we will discuss in

Sec. 5.5.3 the phase shift T_K is a real and measurable quantity. Finally, we note that one can link c and T_K through the relation

$$T_K = \left(\frac{1}{2} - c\right)K. \quad (5.14)$$

5.3 Green's functions

So far, our analysis has only accounted for the separable state (5.6) of non-interacting atoms in a new, collective set of coordinates. Before we can start analyzing the scattering and bound state properties of an interacting pair, we need to address the Green's functions. Fortunately, all the hard work has already been done. The relative motion Green's function for the noninteracting particles is obtained by the Fourier transform

$$G_K^0(E, z) = \int_{-\pi/a}^{\pi/a} \frac{dk}{2\pi} \frac{ae^{ikz}}{E - E_K \cos((T_K + k)a) + i\eta} \quad (5.15)$$

of the relative quasi-momentum Green's function, $\mathcal{G}_K(E; k, k') = \delta(k - k') / (E - \epsilon_K(k))$. By a change of coordinate $k \rightarrow k - T_K$ the integral is identical, except for a front factor, $\exp(-iT_K z)$, to the one studied previously for identical particles, Eq. (3.15). Hence, for energies inside the continuum band we have

$$G_K^0(E, z) = -\frac{ie^{-iT_K z} e^{ik|z|}}{\sqrt{E_K^2 - E^2}}, \quad (5.16)$$

where $ka = \cos^{-1}(E/E_K)$, and outside the continuum we find

$$G_K^0(E, z) = \text{sgn}(E) \frac{e^{-iT_K z} e^{-\kappa|z|}}{\sqrt{E^2 - E_K^2}} [-\text{sgn}(E)]^{z/a} \quad (5.17)$$

with $\kappa a = \cosh^{-1}|E/E_K|$. It is important to note that the Green's function is similar to the identical species case, except for a complex factor $e^{-iT_K z}$ and a modified expression for E_K , Eq. (5.10). All the results of the previous chapters were derived from $G_K^0(E, z)$, so replacing the identical particle $G_K^0(E, z)$ by the appropriate Eqs. (5.16) and (5.17) allows us to directly carry over the results to mixtures of different species.

This is also the case with the interacting Green's function, which still derives from the Dyson equation: $G_K^U(E, z) = G_K^0(E, z) / (1 - U G_K^0(E, z))$, where $G_K^0(E, z)$ now is the different species Green's function and U the appropriate interatomic interaction strength (like in the previous chapters we have assumed on-site interactions).

5.4 Scattering properties

The scattering wave function follows from the Lippmann-Schwinger equation and still has the form

$$\psi_K(E, z) = e^{ipz} + U G_K^U(E, z) \quad (5.18)$$

as derived for the identical particles in Sec. 3.5.1. However, in the heteronuclear case $G_K^U(E, z)$ and $\epsilon_K(k)$ are modified and the scattering state can be written as

$$\psi_K(E, z) = e^{i(k-T_K)z} + UG_K^U(E, 0)e^{-iT_Kz}e^{ik|z|} \quad (5.19)$$

with $ka = \cos^{-1}(E/E_K)$. Note that the relative quasi-momenta of the incoming, $p = k - T_K$, and reflected, $p' = -k - T_K$, waves are not related in the usual way, *i.e.*, $p' \neq -p$, unless $K = 0$. This is explained by the degeneracy of p and p' due to the symmetry of the $\epsilon_K(k)$ around the minimum energy state $k = -T_K$, as shown in Fig. 5.3. It is instructive to note, that except from the spatial variation of the wave function the scattering properties considered in the previous chapters simply depend on the Green's functions evaluated at $z = 0$; therefore all scattering properties can be generalized only by changing E_K .

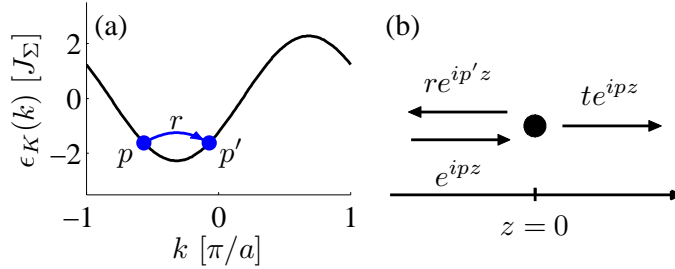


Figure 5.3: Schematic drawing of the scattering process. In (a) the change in relative quasi-momentum under reflection is shown on the relative quasi-momentum spectrum $\epsilon_K(k)$ for $Ka/\pi = 0.8$. In both figures r and t stand for the reflection and transmission amplitudes.

5.4.1 Transmission profile

From the scattered wave in Eq. (5.19) we identify the scattering amplitude $f(E, K) = UG_K^U(E, 0)$ and thereby the reflection coefficient

$$R(E, K) = |f(E, K)|^2 = \frac{U^2}{E_K^2 - E^2 + U^2}, \quad (5.20)$$

which is indicated by the shading in Fig. 5.1(a). In accordance with the identical particle case, it reaches unity at the continuum boundaries, where the density of states diverges, and it has one minimum at the center of the energy band. The transmission coefficient $T(E, K) = 1 - R(E, K)$ can still be probed in scattering experiments or measured spectroscopically by radiative coupling of a bound molecular state to the continuum, see Secs. 3.5.2 and 4.4.2. However, we do not have to consider symmetry for distinguishable particles, so the obtained reflection and transmission coefficients are always meaningful as reflection and transmission probabilities, contrary to the case of indistinguishable particles, see Sec. 3.5.2.

5.5 Bound states

As for identical particles, we determine the bound state energies from the poles of the scattering amplitude. We find a bound state below the continuum in the case of attractive interactions and a repulsively bound state above the continuum in the case of $U > 0$. The energies are the same as for the identical particles,

$$E_b^0 = \text{sgn}(U)\sqrt{E_K^2 + U^2}, \quad (5.21)$$

except that the K dependence of E_K has changed.

5.5.1 Pair tunneling

Following the procedure outlined in Sec 3.6.1, we can, in the limit where $|E_K| \ll |U|$, identify an effective tunneling rate for bound pairs

$$J_{\text{pair}} = -\frac{2J_A J_B}{U}. \quad (5.22)$$

It trivially reduces to $J_{\text{pair}} = -2J^2/U$ [Eq. (3.46)], if $J_A = J_B$. Note that the sign now depends not only on U but also on the sign of the product $J_A J_B$, *i.e.*, whether the two tunneling amplitudes have same or opposite sign.

5.5.2 Bound states wave functions

The bound state wave function for the relative motion is given by $G_K^0(E_b^0, z)$, Eq. (5.17), up to a normalization factor. These functions are exponentially decaying with $|z|$ and the repulsively and attractively bound states differ only by a $\pi z/a$ -phase, *i.e.*, $G_K^0(E_b^0, z)/G_K^0(-E_b^0, z) = (-1)^{z/a}$, in analogy with the single-channel identical atom case, cf. Eq. (3.17). The wave functions are shown in Fig. 5.4.

The bound state wave functions are complex with a spatial phase variation of the relative motion. This is in agreement with our earlier discussion of the lack of time-reversal invariance of the relative motion Hamiltonian restricted to fixed values of K . While such a complex phase variation may give the impression that one particle is passing by the other over and over again within the exponential envelope of their relative motional state, the two atoms are actually moving with the same group velocity. To see this, we recall that the bound states above (below) the continuum have predominantly the quasi-momentum components of the noninteracting continuum states close to the upper (lower) band edge. This implies that the quasi-momentum distribution of the attractively and repulsively bound states are peaked around $k = -T_K$ and $k = \pm\pi/a - T_K$, respectively. For these eigenstates of H_0 a simple calculation

$$\frac{\partial \epsilon_K(k)}{\partial k} = \frac{dE_A}{dq_A} \frac{dq_A}{dq} + \frac{dE_B}{dq_B} \frac{dq_B}{dq} = \hbar(v_A - v_B) \quad (5.23)$$

relates the group velocities v_β of species β to the derivative of the energy dispersion $\epsilon_K(k)$. At the band edges $\epsilon_K(k)$ reaches its extrema, *i.e.*, $\partial \epsilon_K(k)/\partial k =$

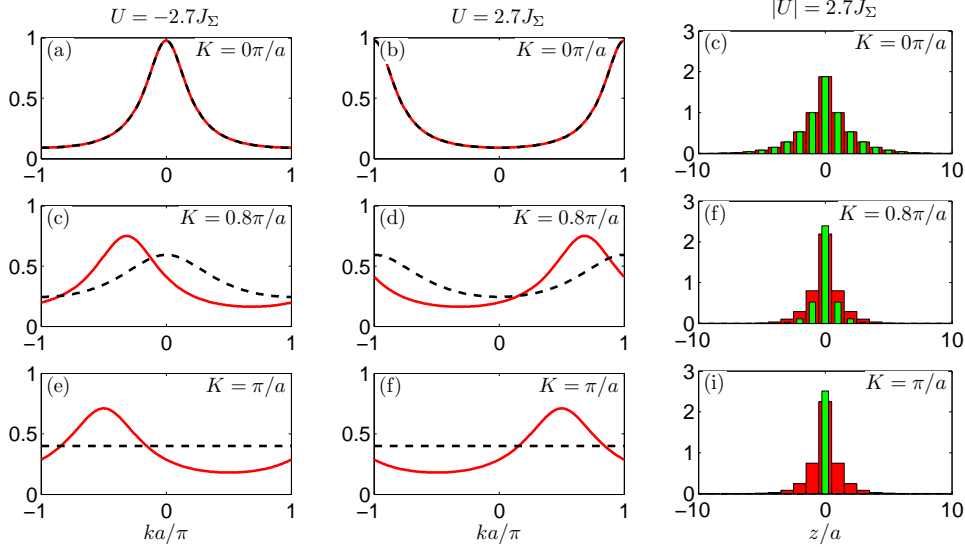


Figure 5.4: The relative motion quasi-momentum wave function of the attractively and repulsively bound atom pairs. First and second column show the relative quasi-momentum wave function $\phi_K^b(k)$ for $U < 0$ and $U > 0$, respectively. The last column shows $|\psi_K^b(z)|$, which is identical for the attractive and repulsive bound dimers. The solid lines and the wide bars correspond to $J_\Delta = 0.5$, whereas the dashed lines and narrow bars correspond to the identical atom model, $J_\Delta = 0$.

0, exactly when $k = -T_K$ or $k = \pm\pi/a - T_K$, and the group velocities of the atoms agree for these relative quasi-momentum components. Furthermore, since $\epsilon_K(k)$ is an even function around $k = -T_K$, the derivative and hence the difference in group velocity $v_A - v_B$ is odd. If we return to the scattering state in Eq. (5.19), we therefore observe that the difference in relative group velocity always changes sign when the wave is reflected.

In Fig. 5.5 we show the quasi-momentum distribution of the two components A and B for both a repulsively (a) and attractively (b) bound atom pair. We have assumed a Gaussian distribution in K with center $\bar{K} = 0.8\pi/a$ and standard deviation $\sigma_K = 0.1\pi/a$. Clear peaks appear at $q_A + q_B = \bar{K}$ and $q_A - q_B = -2T_{\bar{K}}$ as marked by crosses. Here $T_{\bar{K}} = 0.32\pi/a$, corresponding to $(q_A, q_B) = (0.08\pi/a, 0.72\pi/a)$ in the attractive case (a), while $(q_A, q_B) = (-0.92\pi/a, -0.28\pi/a)$ in the case of repulsion (b). The Brillouin zone plotted in Fig. 5.5, *i.e.*, $(q_A, q_B) \in (-\pi/a, \pi/a]^2$, is rotated by 45° compared to the Brillouin zone $(K, k) \in (-\pi/a, \pi/a]^2$. Therefore we need to *continuously* extend Eq. (5.11) for T_K to higher K -Brillouin zones.

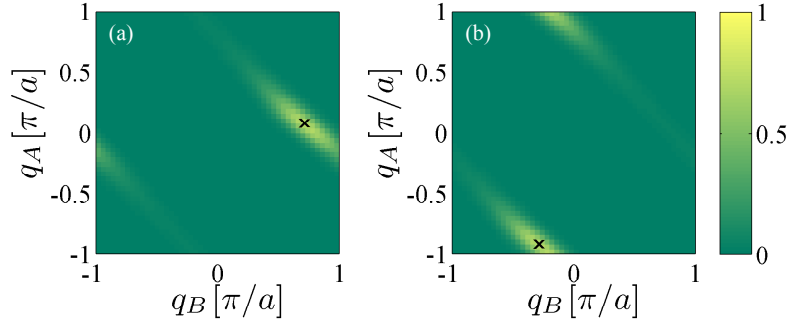


Figure 5.5: Quasi-momentum probability distribution in units of $(a/2\pi)^2$ for the species A and B in a bound state with (a) $U = -2.7J_\Sigma$ and (b) $U = +2.7J_\Sigma$.

5.5.3 Experimental observation of T_K

We suggest to measure the wave number shift T_K by rapid ramp down of the lattice potential, because, if adiabatic, J_Δ and thereby T_K will also change adiabatically. The main peak in the momentum distribution of each individual species is then shifted by $K/2 \rightarrow K/2 \pm T_K$ for $U < 0$ and $K/2 \rightarrow K/2 \pm T_K \pm \pi/a$ for $U > 0$ compared to $J_\Delta = 0$. The case with attractive interaction is shown in Fig. 5.6(a) with the same spread in K as in Fig. 5.5. In an experiment the difference between the main momentum peaks of the two species is $2T_K$, which can easily be measured from a time-of-flight experiment. After expansion time t the spacial separation between the main peaks are $Kt/2(m_A^{-1} - m_B^{-1}) + T_K t/\mu$, where μ is the reduced mass. The case with repulsive interaction is shown in Fig. 5.6(b).

If the species are held by different lasers, the lattice may be turned off adiabatically in a controlled fashion that keeps the difference in the tunneling amplitudes J_Δ , and hence T_K , fixed.

5.5.4 Correlation function

Finally, the quasi-momentum shift T_K may also be measured from the correlation function

$$C(k) = \int_{-\infty}^{\infty} dk_B |\Psi(k + k_B, k_B)|^2. \quad (5.24)$$

Here $\Psi(k_A, k_B)$ is the Fourier transform of the continuous-coordinate wave function, Eq. (5.4). The correlation function for the bound states has peaks at $k = 2T_K + 2\pi m/a$, $m \in \mathbb{Z}$, as seen from Fig. 5.7. Note that the peak locations are identical for the repulsively and attractively bound states, because replacing T_K with $T_K \pm \pi/a$ only changes m . The correlation functions for a pair of repulsively bound atoms are shown in Fig. 5.7 for three values of K_0 . The main peak is slightly shifted towards $k = 0$ because of the Bloch wave structure, where components close to the zone boundary are depleted

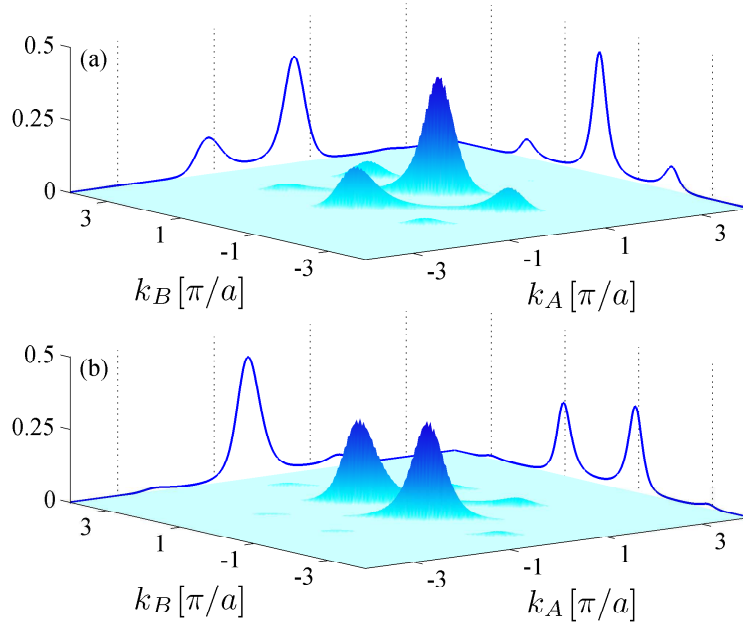


Figure 5.6: Momentum probability distribution in units of $(a/2\pi)^2$ for a pair of (a) attractively bound and (b) repulsively bound atoms with the same parameters as in Fig. 5.5. The solid lines show the projected probability of each species $P(k_\beta)$ in units $a/2\pi$.

due to strong coupling to other zones. We do not believe this method has any advantages compared to the suggestion in the previous section, but it is instructive to visualize the correlation function.

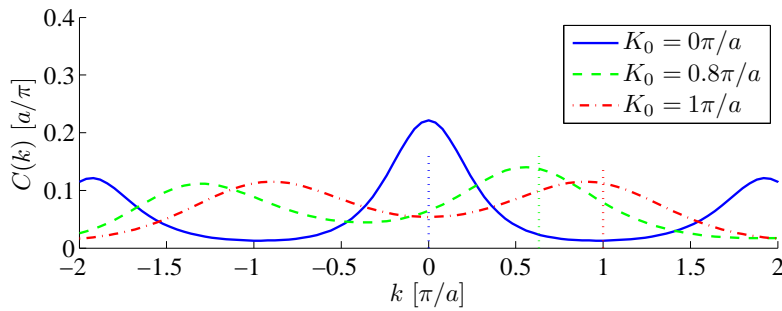


Figure 5.7: Correlation functions for a bound atom pair. The collective quasi-momentum is centered around K_0 as given in the legend and has Gaussian width $\sigma_K = 0.1\pi/a$. The vertical dotted lines indicate the position of $2T_{K_0}$.

5.6 Inclusion of a Feshbach resonance

Most of the results from Chapter 4 can be generalized to mixed species just by updating $G_K^0(E, z)$ and E_K by their new values. Because both the inter-channel coupling and the interaction \hat{U} are δ -functions of the relative coordinate, the phase shift T_K will not influence on the binding energies nor the scattering amplitude and the thereof derived quantities like, *e.g.*, pair tunneling, reflection and transmission probabilities and the scattering length. The phase shift will, however, still affect the wave functions.

We will here only address the molecular dissociation sweep and the bound pair tunneling as proofs of concept, but as outlined above most of the Feshbach physics of Chap. 4 can easily be carried over. However, the validity considerations from Sec. 4.7.2 of course also need to be generalized.

5.6.1 Sweep experiment

In a molecular dissociation sweep the resonance state is scanned trough the continuum. In the continuum the decay width was found in Sec. 4.4.4 to be $\Gamma = 2\text{Im}[\mathcal{W}^2 G_K^U(E, 0)]/\hbar$, which again is unchanged except for the expression for E_K . Therefore, the survival probability is identical to Eq. (4.31)

$$\chi = m(|E_K|) = \exp \left[-2\pi\alpha \left(1 - \sqrt{\frac{\beta_K^2}{1 + \beta_K^2}} \right) \right], \quad (5.25)$$

except that $\beta_K = U/E_K$ has changed. The survival probability increases with increasing $|\beta_K|$, this happens when $|U|$ is increased, or, if $J_\Sigma > J_\Delta$, when $|K|$ approaches the zone boundary. The value of β_K is either strictly increasing or decreasing towards its zone boundary value $\beta_{K=\pi/a} = J_\Sigma/J_\Delta \times \beta_{K=0}$ depending on whether $J_\Sigma < J_\Delta$ or $J_\Sigma > J_\Delta$, respectively. In the case of identical particles the survival probability always approached unity at $K = \pi/a$, because β_K diverged at this point. The present model does not have this pathological feature, because E_K never reaches zero (when $J_\Sigma, J_\Delta = 0$). The dependence on the adiabaticity parameter $\alpha = \mathcal{W}^2/\Delta\mu\hat{B}\hbar$ is unchanged and the survival probability still drops as α is increased. Both the survival probability and the average energy of the dissociated atoms are shown in Fig. 5.8 [cf. Fig. 4.12]. The average energy of the decayed atoms are calculated from Eq. (4.32). The curve approach $E_K/2$ as α is increased.

5.6.2 Two-channel pair tunneling

From the two-channel calculation we can carry over Eq. (4.35) to give

$$J_{\text{pair}} = -\frac{2J_A J_B}{E_b^{[E_K=0]}}, \quad (5.26)$$

We remind the reader that for most values of the resonance energy there are two bound states and therefore also two values of $E_b^{[E_K=0]}$ and J_{pair} . When

the resonance is far off-resonant one of the pair tunnelings approaches the single-channel result, Eq. (5.22).

5.7 Conclusion

In this chapter we have generalized the analytical solutions for identical particles obtained in the previous chapters to the case of two different atomic species. We have shown that it is possible, due to the discrete nature of the Hamiltonian (5.5), to separate the wave function into a collective and a relative coordinate part. In this separation it appeared useful to define the mean and half-difference tunneling amplitudes J_Σ and J_Δ , respectively. We argued that $8|J_\Sigma|$ and $8|J_\Delta|$ determine the maximum and minimum width of the continuum (the sign of the product $J_A J_B$ determines, which is the maximum and which is the minimum.). We parametrized the two-body continuum spectrum in terms of two quantities, which indeed appeared to be central for the physics: The collective energy E_K [Eq. (5.10)] and the phase shift T_K [Eq. (5.11)]. The collective energy delineates the continuum and the phase shift is minus the minimum energy relative quasi-momentum.

The wave functions were obtained directly from the identical particle case by updating E_K and adding the phase factor $e^{iT_K z}$ to the Green's functions. For the scattering waves (5.19) the phase factor ensures that the group velocity of the reflected pair changes sign, while for the bound state wave functions (5.17) it resulted in a quasi-momentum peak centered around $-T_K$ and $\pm\pi/2 - T_K$ for attractively and repulsively bound atoms, respectively, ensuring identical group velocity of the two constituents. This also results in a complex wave function, which was expected, because the relative motion component of Hamiltonian \hat{H}_K^0 is not time-reversal invariant. Furthermore, we suggest how to measure the phase shift experimentally. [Secs. 5.5.3 and 5.5.4]. In analogy with the identical particle case we found bound states both for attractive and

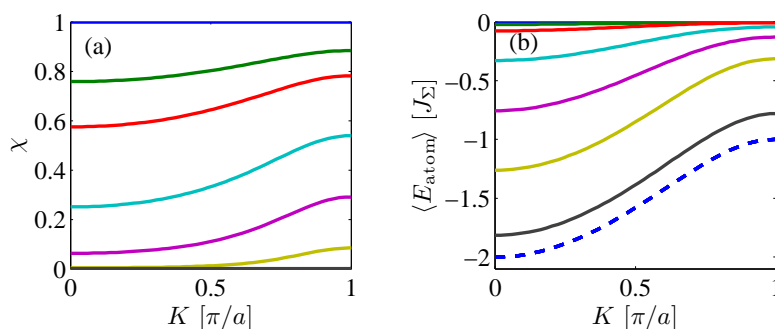


Figure 5.8: (a) Portion of molecules surviving a scan through the continuum and (b) the average energy of the dissociated atoms. From above $\alpha=0, 0.1, 0.2, 0.5, 1, 2, 10$. The blue dashed line in (b) corresponds to $E_K/2$. Here $|U| = 2.7J_\Sigma$.

repulsive interaction. The bound state energies are $E_b = \text{sgn}(U)\sqrt{U^2 + E_K^2}$, and the pair tunneling was obtained: $J_{\text{pair}} \simeq -2J_A J_B / U$. The latter was also derived for the two-channel case [Sec. 5.6.2] and for both the single- and two-channel case it now depends on the sign of the atomic tunneling amplitudes, which were not the case for homonuclear atom pairs.

All scattering properties considered in the thesis so far only depend on the Green's functions evaluated at $z = 0$, therefore we only have to update E_K to generalize those quantities to the different species case. As examples we calculated the single-channel reflection probability [Sec. 5.4.1] and the (two-channel) survival probability of a resonance state to pass through the continuum in a diabatic sweep [Sec. 5.6.1]. In both cases the most pronounced change was that the width of the continuum no longer vanishes at the collective quasi-momentum zone boundary, $K = \pi/a$, but sustained a finite width of $8|J_\Delta|$.

We have nowhere in this chapter used the assumption that both atoms are in the lowest Bloch band. The atoms could have been in whatever band it should be, and all the results in this chapter are still applicable. This opens up for the possibility that identical particles are placed in different Bloch bands, which also provides $J_A \neq J_B$. In that case one should remember the comment on indistinguishably particles in Sec. 3.5.2. Of course, one should also check whether the on-site assumption for the interaction is still reasonable for higher Bloch bands, where the Wannier functions are broadened.

The main message of this chapter is that two-body dynamics with different species can be conveniently described in terms of the Green's function formalism introduced in Chapter 3.

Chapter 6

Two-body dynamics beyond nearest-neighbor tunneling

Up to now we have analyzed the two-body dynamics within the nearest-neighbour approximation. This greatly simplifies the analysis and allows us to do almost everything analytically even for the two-channel problem. Unfortunately, it is not the whole story, since it does not reproduce the correct momentum dependency of the energy dispersion [as discussed in Sec. 2.7]. In this chapter we will show how to extend the results from chapter 3 to go beyond the nearest-neighbor tunneling approximation.

6.1 Introduction

As the experiments improve and can measure quantities with higher and higher precision and get more subtle, the theories have to do the same. Moreover, situations are encountered, where the nearest-neighbor approximation analyzed in the previous three chapters, fails to account for the underlying physical processes in many-body physics, because the reproduced momentum spectrum is inaccurate. As we will see in Chap. 7, this is essential when predicting the outcome of a collision experiment involving condensates. In this chapter we show how to include an arbitrary number of tunneling amplitudes in the results from Chap. 3. We find essential changes to both the bound states and the scattering states.

6.2 Noninteracting atoms

The discrete-lattice Hamiltonian for two identical particles in a quasi-one-dimensional lattice takes the form

$$H_0 = - \sum_{d=1}^{\mathcal{D}} J_d (\Delta_{z_A}^{(d)} + \Delta_{z_B}^{(d)} + 4), \quad (6.1)$$

when we include more than nearest-neighbor hopping. Here $J_d = -\langle w_{1z_{j+d}} | \hat{\mathcal{H}}_0 | w_{1z_j} \rangle$ is the tunneling amplitudes and the action of the “ d^{th} -Laplacian” is given by $\Delta_x^{(d)} f(x) = f(x + ad) + f(x - ad) - 2f(x)$. The number of neighbor tunnelings included is \mathcal{D} , and to exemplify the effect of the remote tunnelings we will compare results for $\mathcal{D} = 1, 2$ and 6 , where $\mathcal{D} = 1$ corresponds to the nearest-neighbor approximation considered in Chap. 3. The derivation of H_0 is similar to that of Eq. (3.2) (see App. A.2), but with the nearest-neighbor single-particle Hamiltonian Eq. (2.14) replaced with Eq. (2.10).

We can still apply the separation Ansatz, $\psi(z_A, z_B) = \sqrt{a/2\pi} e^{iKZ} \psi_K(z)$, where Z and K are the center-of-mass coordinate and quasi-momentum, respectively, and $z = z_A - z_B$ is the relative coordinate. The separation results in a one-body Schrödinger equation for the relative coordinate

$$\left[-2 \sum_{d=1}^{\mathcal{D}} J_d \cos\left(\frac{1}{2}Kda\right) \left(\Delta_z^{(d)} + 2 \right) \right] \psi_K(z) = E \psi_K(z). \quad (6.2)$$

It is readily verified that plane waves, $\psi_K(z) = \sqrt{a/2\pi} e^{ikz}$, are eigenfunctions with energies

$$\epsilon_K(k) = -4 \sum_{d=1}^{\mathcal{D}} J_d \cos\left(\frac{1}{2}Kad\right) \cos(kad). \quad (6.3)$$

If we only include $d = 1$, the above three equations, Eqs. (6.1), (6.2) and (6.3), reduce to their nearest-neighbor counterparts, cf. Eqs. (3.2), (3.9) and (3.6). The spectrum is displayed in an extended Brillouin zone in Figs. 6.1(a)-(c) with inclusion of different numbers of tunneling amplitudes. The spectra are for the first Bloch band and a lattice with longitudinal lattice strength $V_0 = 1$.

In the nearest-neighbor approximation we had a complete degeneracy in k from the front factor $\cos(\frac{1}{2}Ka)$ when $K = \pm\pi/a$, this degeneracy is now lifted by the amount

$$\Delta\epsilon = 8 \sum_{m \in \mathbb{N}} (-1)^m J_{2m}, \quad (6.4)$$

i.e., $\Delta\epsilon$ is the width of the band for $K = \pm\pi/a$, as evident from Figs. 6.1(b)-(c). The different shades of blue in Fig. 6.1 show the density of states:

$$D_K(E) = \sum_{\epsilon_K(k)=E} \left| 4\pi \sum_{d=0}^{\mathcal{D}} d J_d \cos\left(\frac{1}{2}Kad\right) \sin(kad) \right|^{-1}. \quad (6.5)$$

Here $\epsilon_K(k) = E$ can have several (more than two) solutions and therefore the sum is included explicitly (it was replaced by a factor of two in the previous chapters). First we note that the density of states still diverges for $k = 0$ and $k = \pm\pi/a$ due to the flatness of the $\cos(kad)$ -functions in $\epsilon_K(k)$. From Figs. 6.1(b)-(c) we observe the appearance of an additional divergence close to center-of-mass zone boundary, $K = \pm\pi/a$. To see where this extra van Hove

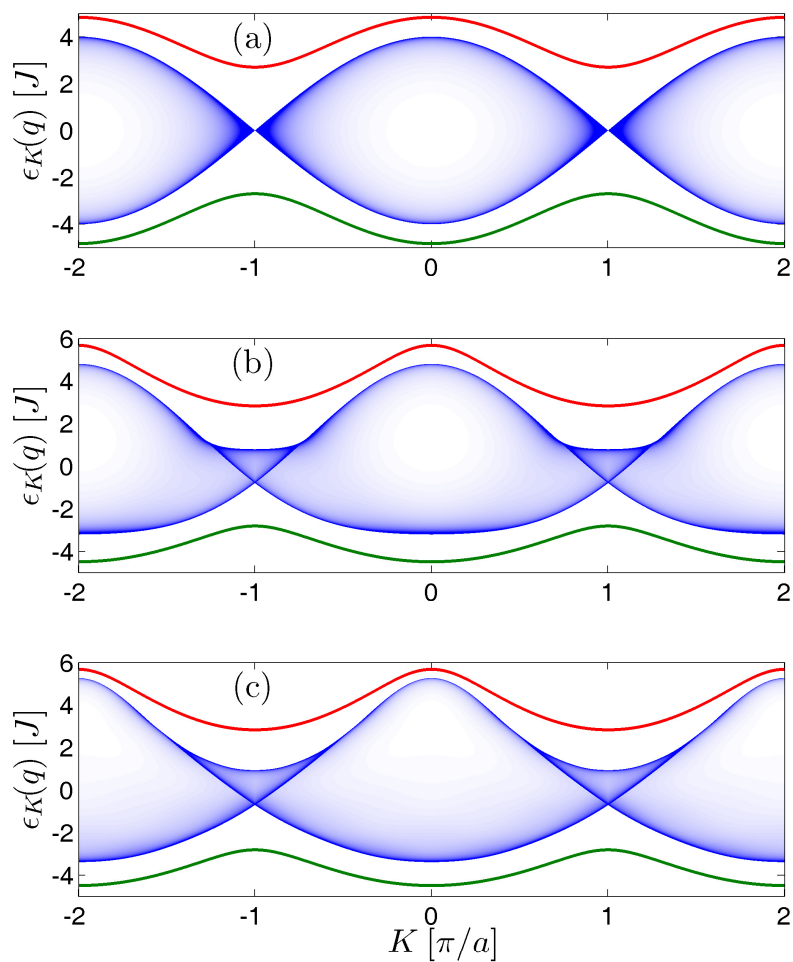


Figure 6.1: Bound state and scattering spectrum for a lattice with $V_0 = 1$. The density of scattering states are indicated by the blue shading with dark colors corresponding to high density. The red and green lines are the bound state energies for $U = 2.7J_1$ and $U = -2.7J_1$, respectively. Calculation including (a) only J_1 , (b) J_1 and J_2 , and (c) J_d up to $d = 6$.

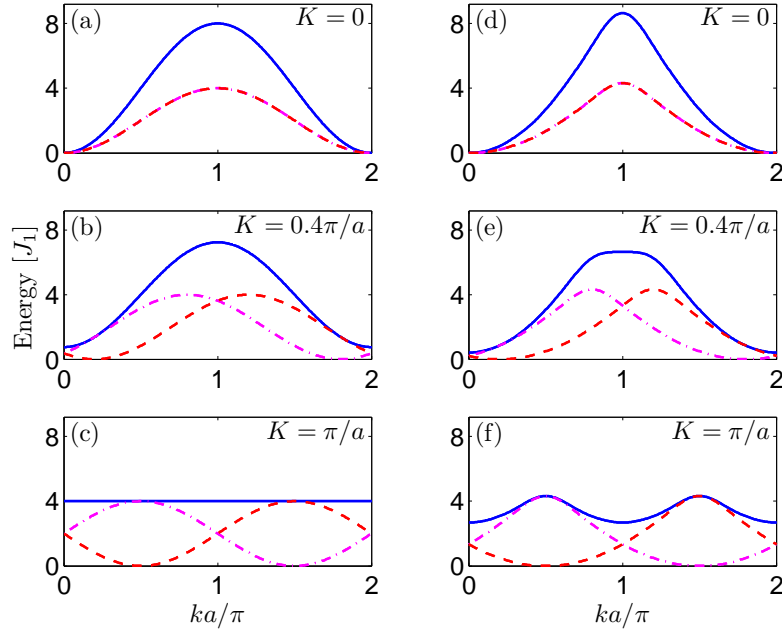


Figure 6.2: Two-body band structure $\epsilon_K(k)$ for different values of K (solid lines) and the band structure of the individual atoms, *i.e.*, $E(K/2 + k)$ and $E(K/2 - k)$ (dotted lines). In (a)-(c) the band structure is approximated by a cosine and in (d)-(f) tunneling terms up to J_6 are included in the band structure. Note that the energy curves in each subfigure has been displaced by a common energy constant as to make all energies positive.

singularity comes from, we remind ourselves that $\epsilon_K(k) = E(\frac{K}{2} + k) + E(\frac{K}{2} - k)$, where $E(q)$ is the one-body band structure, defined in Eq. (2.9). In Fig. 6.2 the band structures for each individual atom are plotted together with the two-body energy spectrum $\epsilon_K(k)$ - all as function of the relative momentum k . The extra van Hove singularity arises due to the appearance of a local minimum in $\epsilon_K(k)$ at $k = \pi/a$. This phenomenon sets in when $\frac{\partial^2 \epsilon_K}{\partial k^2}(k = \pi/a) = 0$ as shown in Fig. 6.2(e) where $K = 0.4 \pi/a$. We note that this can never occur when only nearest-neighbor tunneling is included, since $\frac{\partial^2 \epsilon_K(k)}{\partial k^2} = 0$ and $\frac{\partial \epsilon_K(k)}{\partial k} = 0$ cannot be simultaneously satisfied for a pure cosine dispersion. When $K = \pm \pi/a$, as in Fig. 6.2(f), the energy minima at $k = 0$ and $k = \pi/a$ become degenerate and therefore we expect only two divergences in the density of states in agreement with Figs. 6.1(b) and 6.1(c).

6.3 On-site versus off-site interaction

We still assume that the atoms interact via an on-site interaction $U\delta_{z,0}$ as introduced in Sec. 3.3. But since we now include tunneling amplitudes between lattice sites far apart, we have to justify that we only include on-site interaction

in our model. The interaction between atoms sitting on various lattice sites can be computed as the matrix element

$$U_{ijkl} = g_{1D} \int_{-\infty}^{\infty} dx w_{1z_i}(x) w_{1z_j}(x) w_{1z_k}(x) w_{1z_l}(x) \quad (6.6)$$

with strength parameter $g_{1D} = g_{\text{bg}} [\int dx w_{10}^\perp(x)^4]^2$, where two atoms initially on sites k and l are coupled to sites i and j . This is possible even for a zero range potential due to the finite overlap of Wannier functions centered on different lattice sites. The interaction strengths are unchanged under permutation of the indices, addition of a common integer to all four indices, *i.e.*, $U_{ijkl} = U_{i+p,j+p,k+p,l+p}$ ($p \in \mathbb{Z}$), or a sign change of all indices: $U_{ijkl} = U_{-i,-j,-k,-l}$. In Fig. 6.3 the leading matrix elements are shown in units of the on-site interaction strength, $U = U_{0000}$. These matrix elements fall off rapidly for Wannier functions situated in different wells, and for $V_0 = 1$, we find that the leading “off-site” term is only 5% of U , $U_{1100} = 0.05U$. It is hence a small perturbation compared to the on-site term. However, comparing it to next-nearest-neighbor tunneling we find: $U_{1100}/J_2 = 0.25U/J_1$ (Tab. 2.1). In our examples $U = \pm 2.7J_1$ have been used, in which case the U_{1100} -term may contribute significantly. This suggests that the theory in this chapter is primarily applicable to setups with low background scattering length ($U \propto a_{\text{bg}}^{3D}$) or weak transverse confinement both things reducing g_{1D} in Eq. (6.6). It is worth remembering that the scattering spectrum, and hence all the conclusions in the previous section, is completely independent of the interaction and therefore unaffected by the off-site interaction elements. A more detailed investigation of off-sites interactions can be found in Refs. [105, 106].

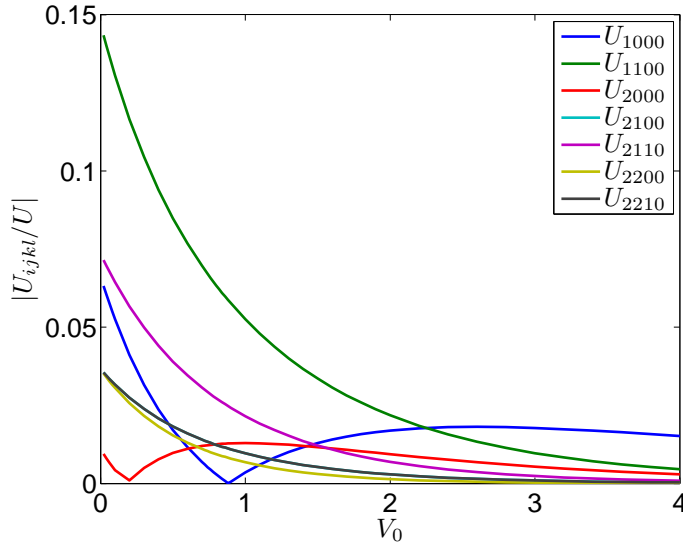


Figure 6.3: Absolute values of off-site interaction elements U_{ijkl} in units of $U = U_{0000}$.

6.4 Green's functions

Like in the other chapters the unperturbed relative-coordinate Green's function is obtained as an integral over the momentum-space representation $\mathcal{G}_K^0(E, k) = 1/(E - \epsilon_K(k))$:

$$G_K^0(E, z) = \frac{a}{2\pi} \int_{-\pi/a}^{\pi/a} dk \frac{e^{ikz}}{E - \epsilon_K(k) + i\eta}, \quad (\eta \rightarrow 0^+). \quad (6.7)$$

We will only attempt to solve this integral numerically. If E is inside the continuum, we can avoid the poles in the numerical integration by Sokhotsky-Weierstrass theorem (3.18),

$$G_K^0(E, 0) = \mathcal{P} \int_{-\infty}^{\infty} \frac{D_K(E')}{E - E'} dE' - i\pi D_K(E). \quad (6.8)$$

We note that an solution for $G_K^0(E, z)$ has been found in [107], which for next-nearest-neighbor tunneling provides an explicit formula. Unfortunately, in the general case with tunneling between $\mathcal{D} > 2$ neighbors the solution includes solving a \mathcal{D} -degree polynomial. The Green's function may also be found from a contour integral approach, this is done for next-nearest-neighbor hopping in App. A.3. However, this is work in progress and we will, in the rest of this chapter, adhere to the numeric technique described above.

6.5 Scattering properties

The scattering states are given by the Lippmann-Schwinger equation (3.27),

$$\psi_K(E, z) = e^{ipz} + UG_K^U(E, z). \quad (6.9)$$

This time we do not have a general analytical expression for the interacting Green's function $G_K^U(E, z) = G_K^0(E, z)/(1 - UG_K^0(E, 0))$ and therefore we cannot identify the scattering amplitude. However, we can calculate the ‘‘on-site’’ probability for the scattered waves

$$|\psi_K(E, 0)|^2 = \frac{1}{[1 - U\text{Re} G_K^0(E, 0)]^2 + [\pi U D_K(E)]^2} \quad (6.10)$$

by means of Eqs. (6.8) and (6.9). We showed for nearest-neighbor tunneling that this quantity is identical to the transmission coefficient $T_K(E)$, unfortunately this is not true for $\mathcal{D} > 1$, because it relied on $\psi_K(E, z)$ being equal to its asymptotic form for all $z \geq 0$. However, the transition probability from a lower lying state $|i\rangle$ to the continuum is still proportional to $|\psi_K(E, 0)|^2$ (Sec. 3.5.2). This quantity is depicted in Figs. 6.4 and 6.5 with next-nearest-neighbor tunneling included in the numeric calculations. The color scale in Fig. 6.4 is chosen such that dark blue in accordance with Fig. 3.2, showing the reflection coefficient $R(K, E)$ for $\mathcal{D} = 1$, corresponds to vanishing transition probability. We first observe that the transition probability still goes to

zero at the continuum boundaries as was also the case in the previous chapters. In addition, it also vanishes at the extra van Hove singularity induced by the beyond-nearest-neighbor tunneling couplings, cf. Fig. 6.1(b). Moreover, the transition probability now depends on the sign of U , whenever $\text{Re} G_K^0(E, 0)$ is nonzero, and we observe that this is the case except for the continuum energies lying above the extra van Hove singularity. This coincides with the energy range in which the two-body spectrum is four-fold degenerate. In the special case of $K = \pm\pi/2a$, where $J_2 \cos(Ka)$ vanishes and only nearest-neighbor tunneling prevails, the dispersion and thereby also the wave function is identical to the nearest-neighbor approximation as clearly seen in Fig. 6.5(b). When $K = \pm\pi/a$, the nearest-neighbor term in $\epsilon_K(k)$ vanishes and no continuum exists in the nearest-neighbor approximation, therefore the transition probability is solely due to J_2 , Fig. 6.5(d). Here the extra van Hove singularity has become degenerate with the lower continuum boundary and $\text{Re} G_K^0(E, 0) = 0$ everywhere.

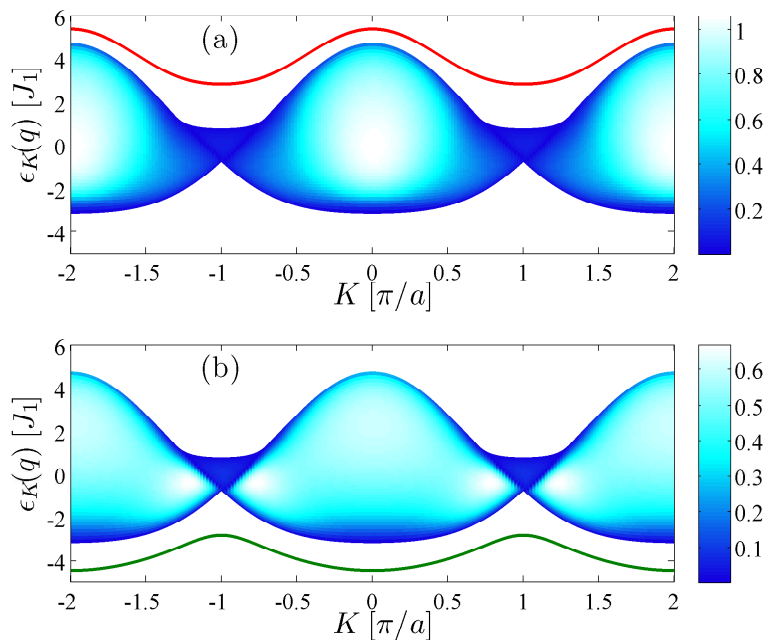


Figure 6.4: On-site probability of the scattering states $|\psi_K(E, 0)|^2$ with (a) $U = 2.7J_1$ and (b) $U = -2.7J_1$. Calculations with J_1 and J_2 . The red and green curves show the bound state energies. Note that the color scales are not identical in the two subfigures.

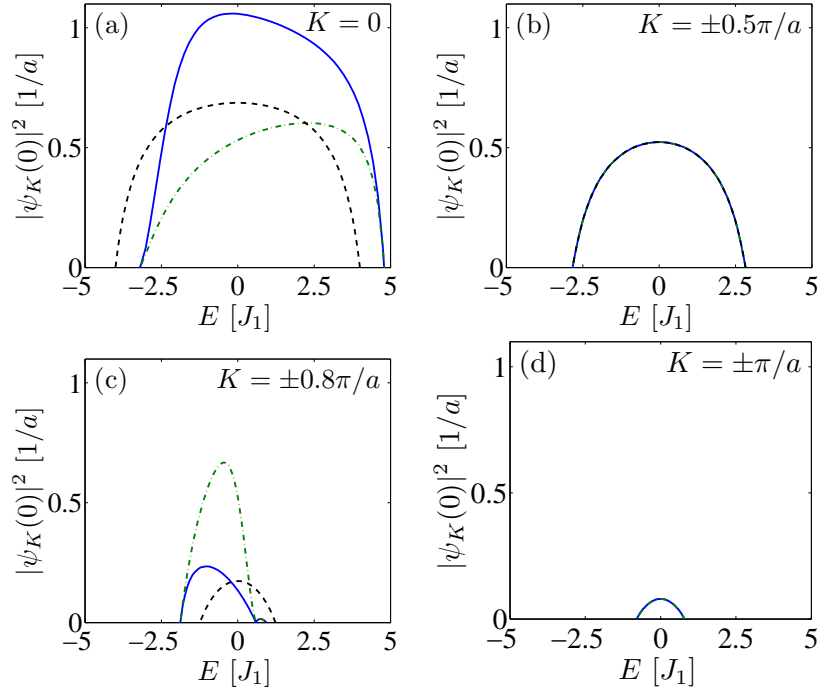


Figure 6.5: On-site probability of the scattering states $|\psi_K(E, 0)|^2$ with $U = 2.7J_1$ (blue line) and $U = -2.7J_1$ (green line) for $\mathcal{D} = 2$. The black dashed line shows the transmission coefficient for the nearest-neighbor approximation, Eq. (3.32).

6.6 Bound states

The energies of the bound states are found numerically as poles of the interacting Green's function, $1 = UG_K^0(E_b, z = 0)$. The found spectra are included in Figs. 6.1 and 6.4.

6.6.1 Bound state wave functions

The bound state wave functions are proportional to $G_K^0(E_b, z)$ in position space and $\mathcal{G}_K^0(E_b, k)$ in momentum space and are displayed for a repulsively and attractively bound atom pairs in Fig. 6.6 and Fig. 6.7, respectively. In both figures J_d with up to $d \leq 6$ has been included in obtaining the k - and z -distributions of the bound states. As discussed previously, the repulsively (attractively) bound states are dominated by the quasi-momentum components at the top (bottom) of the continuum. As the extra van Hove singularity sets in, the two-body spectrum broadens at $k = \pi/a$, which causes more quasi-momentum components to be close to the top of the continuum, and hence contribute to the bound state, compare Figs. 6.2(e) and 6.6(c). In Fig. 6.6(e) we clearly see the consequences of lifting the k -degeneracy at $K = \pm\pi/a$. The

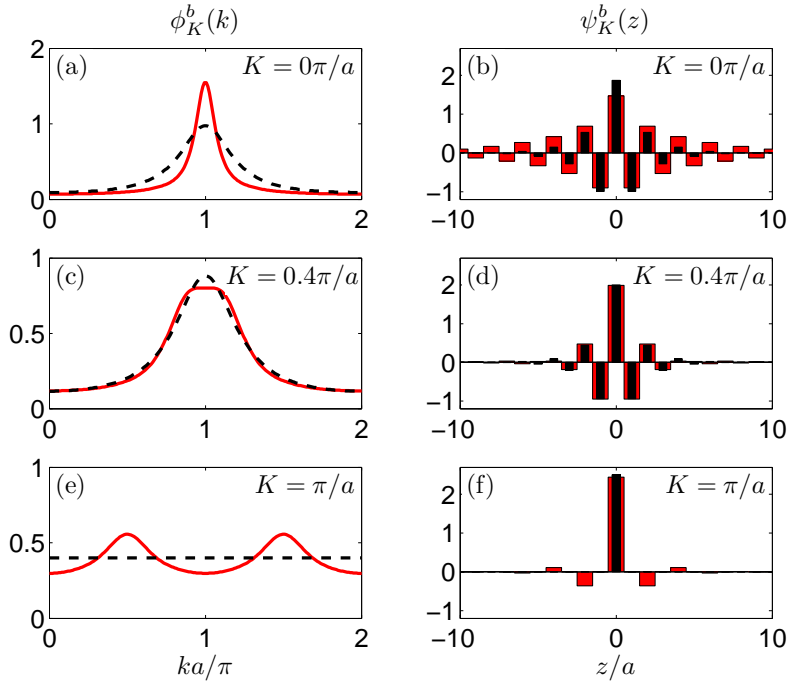


Figure 6.6: Repulsively bound states with tunneling up to J_6 included (red) compared to the nearest-neighbor equivalent (black). First column shows $\phi_K^b(k)$ in units of \sqrt{a} and the second $\psi_K^b(z)$ (dimensionless) obtained from $\mathcal{G}_K^0(E_b, k)$ and $G_K^0(E_b, z)$, respectively. Here $U = 2.7J_1$.

momentum distribution is no longer constant but instead peaked around the two momenta $k = \pm\pi/2a$, which comprise the top of the scattering band, as seen from Fig. 6.2(f).

We observe that for $K = 0$ the quasi-momentum composition of the attractively (repulsively) bound state is broader (narrower) than in the nearest-neighbor approximation, due to the changed two-body spectrum. The broader the momentum composition of a state the more localized is the wave function and visa versa, this results in a more localized (delocalized) attractively (repulsively) bound state. When $K = \pm\pi/a$ the quasi-momentum compositions of the two states are identical except for a shift of $k \rightarrow k + \pi/2a$, and hence the spatial wave functions have equal probability on all lattice sites, compare Figs. 6.6(e,f) and 6.7(c,d).

We observe that the symmetry $\epsilon_K(k) = -\epsilon_K(k + \pi/a)$ discussed in Sec. 3.6.5 is an artifact of the nearest-neighbor model, and disappears when higher J_d tunneling amplitudes are included (more precisely those with even d), and hence the simple relationship between repulsively and attractively bound states from Eqs. (3.57) and (3.58) no longer holds, *i.e.*,

$$E_{rb}(K) \neq -E_{ab}(K) \quad \text{and} \quad \psi_K^{ab}(k) \neq \psi_K^{rb}(k + \pi/a). \quad (6.11)$$

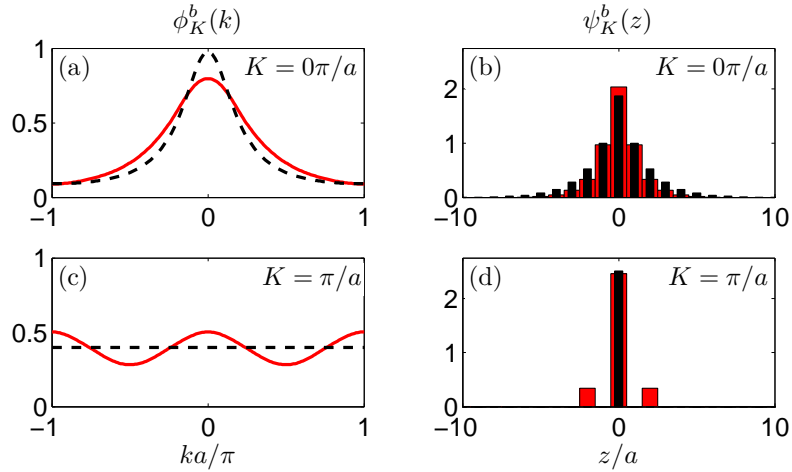


Figure 6.7: Attractively bound state with tunneling up to J_6 included (red) compared to the nearest-neighbor equivalent (black). First column shows $\phi_K^b(k)$ in units of \sqrt{a} and the second $\psi_K^b(z)$ (dimensionless). Note that the k -axis in the first row is changed compared to Fig. 6.6. Here $U = -2.7J_1$.

This is evident from Fig. 6.1 and comparison of Figs. 6.6 and 6.7. In this section we have shown that not only the shape of the band structure is altered compared to the nearest-neighbor model, but also the shape of the wave functions. This can be observed by time-of-flight measurements prepared as prescribed in Sec. 3.6.4.

6.7 Conclusion

In this chapter we have generalized the analytical two-body model to incorporate an arbitrary number of tunneling amplitudes to sites beyond the nearest neighbor. This modifies the scattering properties and the bound states, but it is also necessary, if we want to reproduce the correct quasi-momentum dependency of the spectrum. The latter is particularly important when one studies scattering processes, as we will do in the next chapter.

We found considerable changes in the continuum spectrum compared to the nearest-neighbor model: first of all, the complete degeneracy of all relative quasi-momentum states at the center-of-mass zone boundary is lifted. Another distinct feature is the onset of an extra van Hove singularity close to $K = \pm\pi/a$ which results from the appearance of a local minimum in the two-body spectrum $\epsilon_K(k)$ at $k = \pi/a$. Furthermore, the relative quasi-momentum states at the top and the bottom of the band are no longer necessarily $k = 0$ or $k = \pi/a$.

We have found that a spectroscopic coupling of a deeply bound molecular state $|i\rangle$ is no longer proportional to the transmission probability but is of course still related to the “on-site” wave function. This quantity, we obtained

by numerical integration of the noninteracting Green's function [Sec. 6.5]. Contrary to the nearest-neighbor approximation, it now depends on the sign of the interaction. From the present analysis the scattering amplitudes unfortunately cannot be identified, since we do not know the asymptotic form of the scattered states. This can, however, in the case of next-nearest-neighbor tunneling be overcome by using the analytical solution for $G_K^0(E, z)$ provided in Ref. [107] or App. A.3. This is work in progress.

The bound states were discussed with special emphasis on the differences from the nearest-neighbor approximation [Sec. 6.6]. We argued that there is no longer a simple connection between the energy and wave function of an attractively and repulsively bound states, as was the case for nearest-neighbor tunneling. We also observed that for center-of-mass quasi-momentum close to $K = \pm\pi/a$, the bound state quasi-momentum wave function shows a double peak structure, which we argued can be measured experimentally. Including tunneling couplings beyond nearest-neighbor makes it pertinent to justify the neglect of interactions between neighboring lattice sites [Sec. 6.3]. We showed that the dominant off-site element is less than 5% of the on-site interaction strength for a lattice depth of $V_0 = 1$. This is not necessarily small compared to J_2 , therefore it is preferable to have a weak interaction. This can be achieved by either choosing atoms with a small scattering length (can be accomplished by a Feshbach resonance, see Sec. 4.1) or by choosing a less steep transverse confinement. A different approach not discussed above, could be to replace the Wannier functions by a set of non-orthogonal Wannier-like functions [47]. It has been shown that relaxing the orthonormal requirement $\langle w_{nz_i} | w_{nz_j} \rangle = \delta_{i,j}$ allows construction of more localized functions. It might be possible in that way to reduce off-site interaction by changing the tunneling amplitudes, which is much easier to account for, and by modifying the mapping to continuum space coordinates, *i.e.*, the shape of the basis functions. Fortunately, “off-site” interactions do not affect the main result of this chapter, namely the conceptual changes of the scattering spectrum, because the spectrum is independent of the interatomic interaction.

Chapter 7

Four-wave mixing

This chapter is devoted to the study of quasi-one-dimensional four-wave mixing. Because four-wave mixing is in its nature a many-body phenomenon we will need to introduce some basic many-body theory among other things: how we define a condensate, the Bose-Hubbard model and two numerical methods. However, the emphasis will still be on two-body dynamics and how it explains the many-body process. The chapter is a natural continuation of Chap. 6, in which the two-body theory was extended by including tunneling beyond nearest-neighbor sites and both our theoretical discussion and simulations will emphasize the importance of the findings in Chap. 6. The contents of this chapter has so far not been published.

7.1 Introduction

In this chapter we will examine the implication of the two-body dynamics on a larger sample of atoms. As already argued in the previous chapters, the two-body discussion is particularly relevant at low density and temperature, where three-body collisions are very rare and only two-body interactions are significant. It is in this limit Bose-Einstein condensation is possible; when cooled below a certain critical temperature, the atoms condense into a common ground state. The physics of this type of many-body systems is very rich. We will, however, restrict our discourse into many-body theory to a single phenomenon, namely, four-wave mixing. The name comes from non-linear optics, where two simultaneously present laser beams, *i.e.* electromagnetic waves, are coupled by a non-linear medium to form new light beams at different frequencies. In ultracold atomic physics the four-wave mixing occurs when two condensates with well defined momenta collide and break up into new momentum components [23, 25]. Whereas in optics the coupling comes from the media in which the beams propagate, in cold atom physics it comes from the atomic interaction, which can be dynamically controlled by a Feshbach resonance (see Chap. 4). From the particle point of view a pair of atoms collide and exit the collision with changed momenta as illustrated in Fig. 7.1. This process we know well from introductory mechanics courses, and it has to

fulfil both momentum and energy conservation,

$$\mathbf{q}_A + \mathbf{q}_B = \mathbf{q}'_A + \mathbf{q}'_B, \quad (7.1a)$$

$$E(\mathbf{q}_A) + E(\mathbf{q}_B) = E(\mathbf{q}'_A) + E(\mathbf{q}'_B), \quad (7.1b)$$

where $E(\mathbf{q})$ is the single-particle energy dispersion. Within a lattice $\hbar\mathbf{q}_i$ is the quasi-momenta and Eq. (7.1a) is modulo an integer multiple of the reciprocal lattice vector.

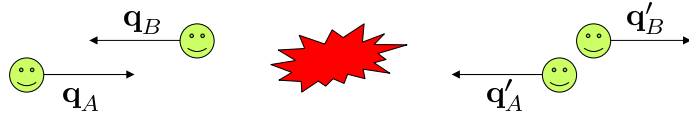


Figure 7.1: Cartoon illustrating four-wave mixing in cold atomic gases: a pair of atoms with (quasi-)momentum \mathbf{q}_A and \mathbf{q}_B collides, and exit the scattering process with (quasi-)momenta \mathbf{q}'_A and \mathbf{q}'_B .

In three-dimensional four-wave mixing there is in general a whole range of possible (quasi-)momenta for the outgoing waves, which in (quasi-)momenta space forms a sphere or an ellipsoid [108]. It is, however, possible to select a certain set of $(\mathbf{q}'_A, \mathbf{q}'_B)$ by seeding a small fraction of atoms in one of the momenta \mathbf{q}'_A or \mathbf{q}'_B . This is due to Bose-stimulation, which is explained later in Sec. 7.4.

As in all the previous chapters, we will also here restrict our analysis to quasi-one-dimensional gases with a weak lattice applied along the direction of motion. Here both incoming (q_A, q_B) and outgoing (q'_A, q'_B) waves are restricted to propagation along the lattice, which greatly reduces the number of possible outgoing waves. We will see in the next section that for a weak quasi-one-dimensional lattice there is at most one possible set $(q_A, q_B) \neq (q'_A, q'_B)$ (for mixtures of different species reflection may also be observed). Of special interest is the case where the two incoming waves are identical, $q_A = q_B = q_0$. In that case the four-wave mixing conditions (7.1) becomes

$$2q_0 = q_1 + q_2 \quad \text{mod } 2\pi/a, \quad (7.2a)$$

$$2E(q_0) = E(q_1) + E(q_2). \quad (7.2b)$$

This can be viewed as a condensate colliding with itself.

This process is particularly interesting, first of all, because it is possible. In free space the energy dispersion is the parabola

$$E(q) = \frac{\hbar^2 q^2}{2m}, \quad (7.3)$$

where m is the atomic mass. With this dispersion the conditions in Eqs. (7.2) can never be fulfilled, because the atom with highest momentum always carry

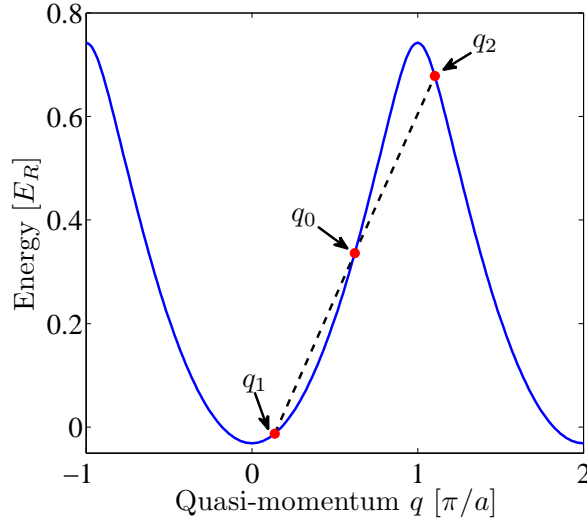


Figure 7.2: Band structure for a single particle in a quasi-one-dimensional lattice with lattice strength $V_0 = 1$. The three quasi-momenta indicated by red dots fulfil both parts of Eq. (7.2).

away too much energy to allow for energy conservation. However, if we introduce a weak lattice, it is possible due to the induced band structure, as depicted in Fig. 7.2.

The process is interesting because the four-wave mixing can be used to generate pairs of entangled gases [109], which is useful in precision measurements. Note that the outcome of four-wave mixing is pair correlated, *i.e.*, for each atom in the q_1 -component there will also be one in the q_2 -component. This is also true in the general three-dimensional four-wave mixing, Eq. (7.1), but in one-dimension the process is highly selective concerning the possible outgoing waves. Splitting up a Bose-Einstein condensate in this way serves as a source of coherent atoms, since the atoms all belong to the same wave function initially. This can be utilized in a Mach-Zehnder-type interferometer [110]. The rough idea is that the four-wave mixing serves as the first mirror in the Mach-Zehnder interferometer sending pairs of atoms in opposite directions, see drawing Fig. 7.3. One of the atomic beams is exposed to a perturbation $\hat{\mathcal{H}}'$, *e.g.*, coming from gravitation or a magnetic field, and therefore acquires a phase which can be read out from the induced interference pattern, when the atoms are brought to interfere at the end of the two paths.

In Fig. 7.2 we did not only prove that energy matching is possible in Eq. (7.2), but the figure also reveals that the first Bloch band is sufficient to explain the process. If the coupling is not too strong, the higher bands may only introduce minor corrections and therefore we will neglect them. Whereas higher bands are insignificant, we find that the beyond nearest-neighbor tunneling is vital: while quasi-momentum conservation is ensured by $q_{1,2} = q_0 \pm \Delta$,

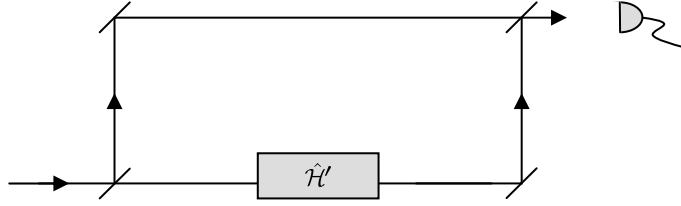


Figure 7.3: Schematic drawing of a Mach-Zehnder interferometer. A coherent cloud of atoms enter in the lower left corner. At the first “beam splitter” a pair of atoms are separated into one atom going along each trajectory. One of the atoms will acquire an phase shift compared to the other due the perturbation $\hat{\mathcal{H}}'$. This phase shift can be measured from the interference pattern when the atoms meet in the upper right corner. There are different proposals for how to guide atomic beams, see references in [110].

the energy conservation reads

$$2 \cos(aq_0) = \cos[a(q_0 + \Delta)] + \cos[a(q_0 - \Delta)] = 2 \cos(a\Delta) \cos(aq_0) \quad (7.4)$$

within the nearest-neighbor approximation. Recall that in that case, the energy dispersion is $E(q) = -2J \cos(aq)$. Except for the uninteresting case, $q_0 = \pi/2a$, where all Δ are possible, this equation implies that $1 = \cos(a\Delta)$. This only occurs when $\Delta = 2\pi p/a$, $p \in \mathbb{Z}$ and since everything is modulo the reciprocal lattice vector this is always zero. Therefore, we cannot have this type of four-wave mixing, if we only include nearest-neighbours hopping.

We will first attack the problem from the two-body point of view, which we argued above is pertinent. Thereafter, we provide the theory needed for the full many-body description. This includes an introduction to the Bose-Hubbard Hamiltonian, which has found numerous applications in cold atom physics with lattices. We use two different models to solve the Bose-Hubbard model: the Gutzwiller approximation and the truncated Wigner method. Finally, we present simulation results of four-wave mixing followed by discussion and outlook.

7.2 Two-body description

The two-body scattering continuum is depicted in Fig. 7.4 for (a) only nearest-neighbor tunneling and (b) for tunneling between lattice sites up to $\mathcal{D} = 6$ sites apart. As dashed lines we have plotted a few k -manifolds, *i.e.*, $\epsilon_K(k)$ as function of K with fixed relative quasi-momentum k . Four-wave mixing can take place whenever two such curves cross, because if $\epsilon_K(k) = \epsilon_K(k')$ for $k \neq k'$, atoms with quasi-momenta $q_{A,B} = K/2 \pm k$ and $q'_{A,B} = K/2 \pm k'$ are degenerate. With only nearest-neighbor tunneling, the k -manifolds only cross at $K = \pm\pi/a$ in which case all states are degenerate, and therefore not interesting in terms of four-wave mixing. This was also concluded from

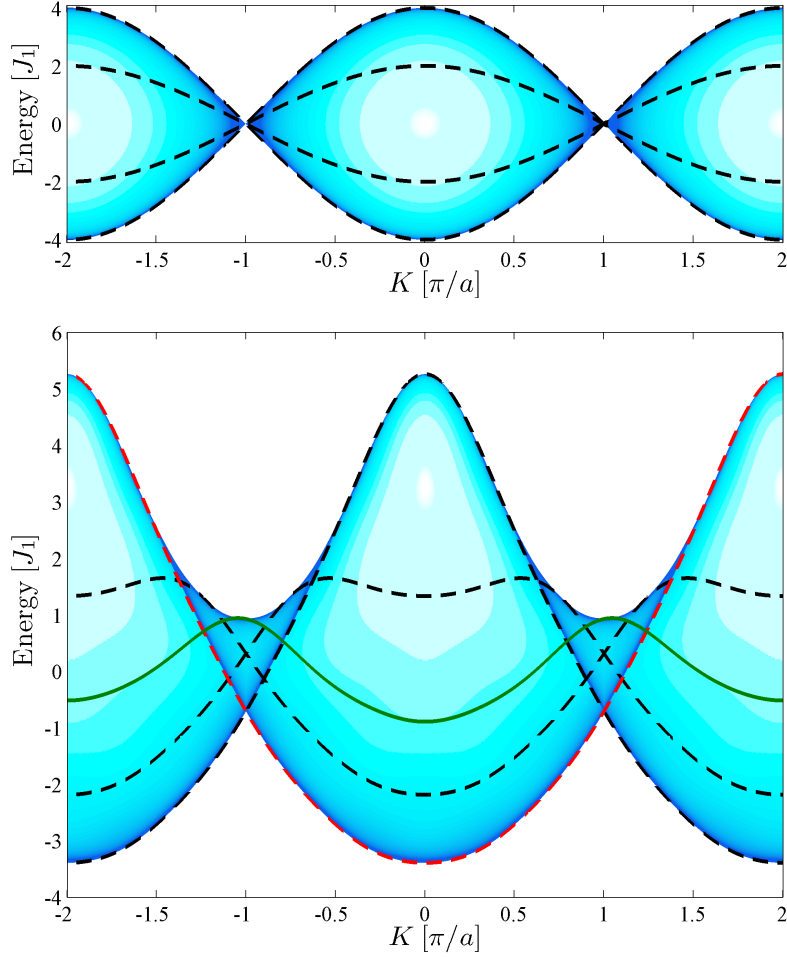


Figure 7.4: Two-body scattering continuum with (a) only nearest-neighbour hopping present and (b) including long-range tunneling amplitudes J_d up to $d \leq 6$. The black dashed lines shows $\epsilon_K(k)$ as function of K with fixed k . From below at $K = 0$ we have $ka/\pi = 0, 1/3, 2/3, 1$. We note that k -manifolds only cross at $K = \pi/2a$ within the nearest-neighbor approximation, whereas the manifolds cross at different quasi-momenta K in (b). In particular the ($k = 0$)-manifold is crossed by all the other k -manifolds along the extra van Hove singularity in the interval $K \in [\pi/a, 2\pi/a - K_c]$, see discussion under Eq. (7.5) for details. In (b) $\epsilon_K(k = 0)$ and $\epsilon_K(k = 0.48\pi/a)$ are plotted by the red and the green curves, respectively. The crossing between these curves represents the four-wave mixing process simulated in Sec. 7.7. Note that the ordinates in the two figures are not equidistant.

Eq. (7.4) above, where we deduced that all pairs with quasi-momenta $q_{A,B} = \pi/2a \pm \Delta$ are degenerate for all values of Δ . Including long-distance tunneling, the situation is quite different; as can be seen in Fig. 7.4(b). In the four-wave mixing process in Eq. (7.2), we have $q_A = q_B = q_0$, and hence $K = 2q_0$ and $k = (q_A - q_B)/2 = 0$ for the entering atoms. The ($k = 0$)-manifold, indicated by the red line, is crossed by all other k -manifolds in the center-of-mass quasi-momentum interval starting with $K = \pi/a$ and ending at $K = 2\pi/a - K_c$, where K_c coincides with the critical point for appearance of an extra van Hove singularity determined by the equation

$$\left. \frac{\partial^2 \epsilon_{K_c}}{\partial k^2} \right|_{k=\pi/a} = 0 \quad (7.5)$$

discussed in Sec. 6.2. Before we explain this we first observe that $k = 0$ for $K \in [\pi/a, 2\pi/a - K_c]$ is identical to $k = \pi/a$ with $K \in [-\pi/a, -K_c]$, where the latter point is inside the first Brillouin zone. This is seen by subtracting $2\pi/a$ from q_B giving $k = (q_A - q_B)/2 \rightarrow k + \pi/a$ and $K = q_A + q_B \rightarrow K - 2\pi/a$. Having justified this, we now recall that $k = \pi/a$ in the two-body spectrum is degenerate whenever $K_c < |K| < 2\pi/a$ with K_c given by Eq. (7.5), see Figs. 6.2 and 7.5. For a lattice depth of $V_0 = 1$ we found $K_c \simeq 0.4\pi/a$ in Sec. 6.2. From this analysis it follows that if we want a condensate to break up in exactly two components, we have to choose $K = 2q_0 \in [\pi/a, 2\pi/a - K_c]$. This is equivalent to

$$\pi/2a < q_0 < q_{\text{inf}}, \quad (7.6)$$

where q_{inf} is the point of inflection for the single-particle band spectrum, $E''(q_{\text{inf}}) = 0$. Note that when the incoming waves are identical we have $\epsilon_{2q_0}(\pi/a) = 2E(q_0)$, which reduces (7.5) to $E''(q_0) = 0$. More generally, for any incoming pair of atoms with quasi-momenta (q_A, q_B) , we conclude that if

$$\epsilon_K(\pi/a) < E(q_A) + E(q_B) < \max_k \epsilon_K(k), \quad (7.7)$$

they are degenerate with a set (q'_A, q'_B) , which is not just a momentum interchange (*i.e.*, a reflection of relative quasi-momentum, $k \rightarrow -k$), see the red curves in Fig. 7.5.

Returning to the continuum spectrum (in Fig. 7.4), we conclude that four-wave mixing only takes place in the regions above the extra van Hove singularity. Those regions are marked by magenta and orange in Fig. 7.6. In the above discussion we focused on the magenta region, but the two areas are identical up to reversing directions. This is seen by changing sign simultaneously on q_A and q_B : $(K, k) \rightarrow -(K, k)$.

The two-body picture is of course not the whole truth. Here we will only mention two things relevant to four-wave mixing that is not explained by the two-body physics alone: firstly, it does not take into account that the last added atom in a condensate has a different energy than the first one, *i.e.*, the mean energy per particle changes with the population of a quantum state. Hence the occupation of the modes influence, which quasi-momentum

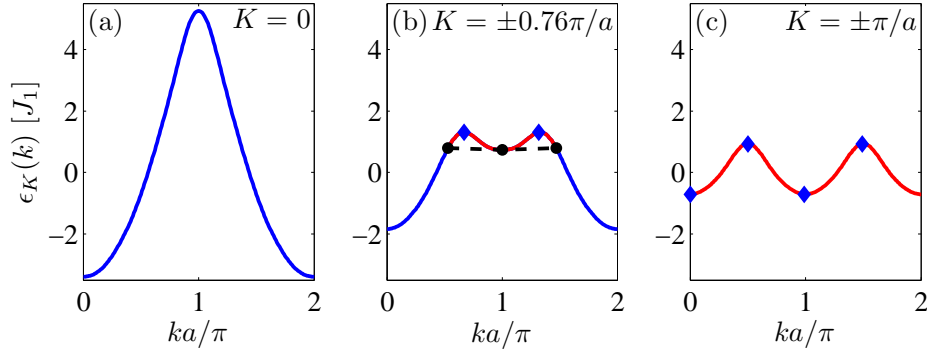


Figure 7.5: Two-body spectrum $\epsilon_K(k)$ for (a) $K = 0$, (b) $K = 2q_0 = \pm 0.76\pi/a$ (the example simulated in Sec. 7.7) and (c) $K = \pm\pi/a$. The blue and red parts of the curves indicate the region in which the quasi-momenta are two- or four-fold degenerate, respectively, *i.e.*, the red region marks where four-wave mixing is possible. In (b) the black dots indicate the three-fold degeneracy allowing the discussed four-wave mixing process, Eq. (7.2). The blue diamonds are extrema of $\epsilon_K(k)$ and the only points on the red curves, which are only two-fold degenerate, *i.e.*, where only quasi-momentum interchange is allowed in a scattering process.

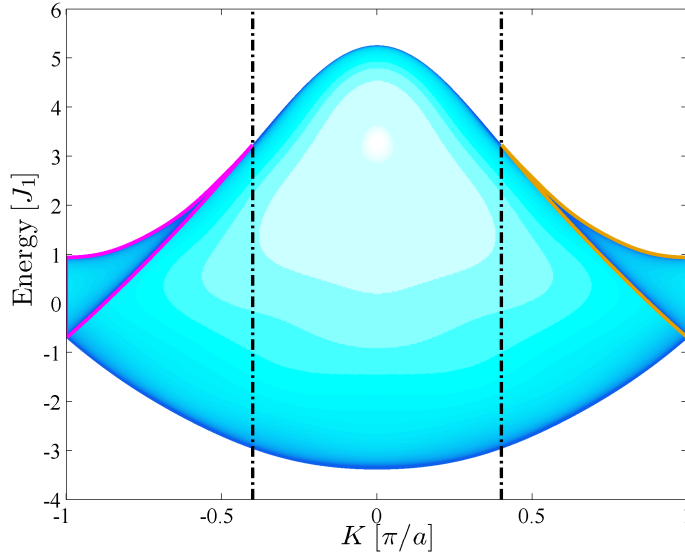


Figure 7.6: Single zone scattering continuum. The two regions where four-wave mixing can take place are enclosed by magenta and orange lines. The regions corresponds to the red part of the curves in Fig. 7.5. The dashed vertical lines indicate $\pm K_c$ as defined in Eq. (7.5).

components are resonant in the four-wave mixing process. Secondly, the two-body process does not account for the “stimulation” of the Bose-stimulated process, *i.e.*, the amplification of the coupling if the modes are populated already. Both things will be explained below in the many-body description.

7.3 Many-body dynamics

“And now for something completely different”

John Cleese

Turning now to the many-body description [30, 111, 112], we first of all write up the Hamiltonian operator in second quantized form

$$\hat{\mathcal{H}} = \int d^3\mathbf{x} \hat{\Psi}^\dagger(\mathbf{x}) \left(-\frac{\hbar^2}{2m} \nabla^2 + V_{\text{lat}}(\mathbf{x}) + V_{\text{ext}}(\mathbf{x}) + \frac{g_{\text{bg}}}{2} \hat{\Psi}^\dagger(\mathbf{x}) \hat{\Psi}(\mathbf{x}) \right) \hat{\Psi}(\mathbf{x}), \quad (7.8)$$

where $\hat{\Psi}(\mathbf{x})$ ($\hat{\Psi}^\dagger(\mathbf{x})$) is the field operator that removes (creates) a particle at the position \mathbf{x} . The bosonic field operators satisfy the bosonic commutator relations

$$[\hat{\Psi}(\mathbf{x}), \hat{\Psi}^\dagger(\mathbf{x}')] = \delta(\mathbf{x} - \mathbf{x}') \quad \text{and} \quad [\hat{\Psi}(\mathbf{x}), \hat{\Psi}(\mathbf{x}')] = 0, \quad (7.9)$$

and the number of atoms at position $\mathbf{x} = (x_1, x_2, x_3)$ is given by $\hat{n}(\mathbf{x}) = \hat{\Psi}^\dagger(\mathbf{x}) \hat{\Psi}(\mathbf{x})$. In Eq. (7.8) a two-body interaction with a zero-range pseudopotential of strength $g_{\text{bg}} = 4\pi\hbar^2 a_{\text{bg}}^{3\text{D}}/m$ has been assumed. This is equivalent to the assumptions in the two-body discussion in the previous chapters, see Sec. 3.3.

7.3.1 Condensate dynamics

For very low temperatures we expect a gas of bosons to all occupy the ground state forming a Bose-Einstein condensate,

$$\frac{1}{\sqrt{N}} \left[\int d^3\mathbf{x} \psi(\mathbf{x}) \hat{\Psi}^\dagger(\mathbf{x}) \right]^N |vac\rangle. \quad (7.10)$$

This is a Hartree state with N particles all in the same state, and we can determine the wave function $\psi(\mathbf{x})$ by using the state (7.10) as a variational Ansatz for the Hamiltonian (7.8). This gives the Hartree equation

$$\left(-\frac{\hbar^2}{2m} \nabla^2 + V_{\text{lat}}(\mathbf{x}) + V_{\text{ext}}(\mathbf{x}) + g_{\text{bg}}(N-1)|\psi(\mathbf{x})|^2 \right) \psi(\mathbf{x}) = \mu\psi(\mathbf{x}), \quad (7.11)$$

Alternatively we could write the field operator as

$$\hat{\Psi}(\mathbf{x}) = \psi_N(\mathbf{x}) + \delta\hat{\Psi}(\mathbf{x}) \quad (7.12)$$

where $\psi_N(\mathbf{x}) = \langle \hat{\Psi}(\mathbf{x}) \rangle$ is the c-number and $\delta\hat{\Psi}(\mathbf{x})$ is the derivation from the c-number. In mean field theory $\delta\hat{\Psi}(\mathbf{x})$ is neglected and the field operator is replaced by its c-number field. This is identical to assuming that the state is an eigenstate of the field operator, *i.e.*,

$$\hat{\Psi}(\mathbf{x}) |\psi_N\rangle = \psi_N(\mathbf{x}) |\psi_N\rangle. \quad (7.13)$$

Minimizing the expectation value of the Hamiltonian with the additional requirement that the average number of atoms fulfils $\int d^3\mathbf{x} \langle \hat{\Psi}(\mathbf{x})^\dagger \hat{\Psi}(\mathbf{x}) \rangle = N$, one finds that $\psi_N(\mathbf{x}) = \sqrt{N}\psi(\mathbf{x})$, where ψ has to satisfy the Gross-Pitaevskii equation

$$\left(-\frac{\hbar^2}{2m} \nabla^2 + V_{\text{lat}}(\mathbf{x}) + V_{\text{ext}}(\mathbf{x}) + g_{bg} N |\psi(\mathbf{x})|^2 \right) \psi(\mathbf{x}) = \mu \psi(\mathbf{x}). \quad (7.14)$$

Here μ is the chemical potential, *i.e.*, the energy per particle. If N is large, this equation is identical to the Hartree equation (7.11). Note that under the mean field assumption the number of atoms is no longer definite, but a Poisson distribution with mean value N . The proper physical state always has a definite number of atoms, therefore calculations based on the latter method may be followed by a projection to a specific number state.

7.4 The Bose-Hubbard model

After this little digression into condensate dynamics, we will now return to the Wannier states, which we shall use as the basis for constructing a discrete many-body Hamiltonian. We will assume the presence of a strong transverse two-dimensional lattice, which makes the gas effectively one-dimensional, and an additional weak lattice along the third direction (x_3). We introduce a set of mode operators

$$\hat{a}_j = \int d^3\mathbf{x} w_j(\mathbf{x})^* \hat{\Psi}(\mathbf{x}) \quad (7.15)$$

associated with the product state $w_j(\mathbf{x}) = w_{10}^\perp(x_1)w_{10}^\perp(x_2)w_{1z_j}(x_3)$ of the first Bloch band longitudinal $w_{1z_j}(x_3)$ and transverse $w_{10}^\perp(x_i)$ Wannier functions. The interpretation of the operator \hat{a}_j^\dagger (\hat{a}_j) is that it creates (destroys) a particle in the Wannier state $w_j(\mathbf{x})$ located at the lattice site centered at the longitudinal coordinate $x_3 = z_j$ and the transverse coordinates $x_1 = x_2 = 0$. We will in the following suppress the transverse degrees of freedom, and just keep in mind that we may have several parallel quasi-one-dimensional gases. It follows from the field operator commutator relations (7.9) and the orthonormality of the Wannier states, that \hat{a}_j obeys the standard Bose commutator relations

$$[\hat{a}_i, \hat{a}_j^\dagger] = \delta_{i,j} \quad [\hat{a}_i, \hat{a}_j] = 0. \quad (7.16)$$

We now expand the field operator on the mode operators

$$\hat{\Psi}(\mathbf{x}) = \sum_j w_j(\mathbf{x}) \hat{a}_j + \delta\hat{\Psi}(\mathbf{x}), \quad (7.17)$$

where $\delta\hat{\Psi}(\mathbf{x})$ represents all the unpopulated modes such as higher Bloch bands, which will be ignored. When we insert the expanded field operator into the Hamiltonian (7.8), we obtain the well-known Bose-Hubbard Hamiltonian [30, 31]

$$\hat{\mathcal{H}}_{\text{BH}} = - \sum_{i \geq j} J_{i-j} (\hat{a}_j^\dagger \hat{a}_i + \hat{a}_i^\dagger \hat{a}_j) + \sum_j \epsilon_j \hat{a}_j^\dagger \hat{a}_j + \frac{1}{2} \sum_{i,j,k,l} U_{ijkl} \hat{a}_i^\dagger \hat{a}_j^\dagger \hat{a}_k \hat{a}_l \quad (7.18)$$

Here J_d with $d = i - j$ is the longitudinal tunneling amplitudes defined in Sec. 2.6,

$$J_d = \int_{-\infty}^{\infty} dx w_{1z_d}(x) \left(-\frac{\hbar}{2m} \frac{\partial^2}{\partial x^2} + V_{\text{lat}}(x) \right) w_{10}(x). \quad (7.19)$$

Recall that the Wannier states are real, and therefore complex conjugation has been omitted. The constant J_0 can be omitted, since it only adds an overall constant to the energy. Furthermore, the tunneling amplitudes decrease in size as d increases, and we can introduce a cut-off \mathcal{D} such that only couplings between lattice sites less than $a\mathcal{D}$ apart are included. The interaction matrix elements

$$U_{ijkl} = g_{1\text{D}} \int_{-\infty}^{\infty} dx w_{1z_i}(x) w_{1z_j}(x) w_{1z_k}(x) w_{1z_l}(x) \quad (7.20)$$

with coupling strength $g_{1\text{D}} = g_{\text{bg}} [\int dx w_{10}^\dagger(x) w_{10}(x)]^2$ were discussed in Sec. 6.3, where we argued that the leading off-site term is less than 5% of the on-site term, $U \equiv U_{0000}$, for a lattice with $V_0 = 1$. Therefore we will neglect all but the on-site interaction term. The last parameter is related to the external potential:

$$\epsilon_j = \int d^3\mathbf{x} V_{\text{ext}}(\mathbf{x}) |w_j(\mathbf{x})|^2 \simeq V_{\text{ext}}(0, 0, z_j), \quad (7.21)$$

where the last equality follows if the external potential varies slowly and can be assumed constant over a lattice period. In the following we will omit the external potential assuming a homogeneous lattice. This is reasonable because we want to show that a particular process, the four-wave mixing process, can take place inside a condensate. Modification due to the trapping and behaviour on the edge of the condensate, would be a study in its own right.

Summarizing the above considerations we end up with the considerably simpler Bose-Hubbard Hamiltonian:

$$\hat{\mathcal{H}}_{\text{BH}} = \sum_j \left[- \sum_{d=1}^{\mathcal{D}} J_d (\hat{a}_j^\dagger \hat{a}_{j+d} + \hat{a}_{j+d}^\dagger \hat{a}_j) + \frac{1}{2} U \hat{n}_j (\hat{n}_j - 1) \right]. \quad (7.22)$$

Here $\hat{n}_j = \hat{a}_j^\dagger \hat{a}_j$ counts the number of particles at site j . We note that $\hat{n}_j (\hat{n}_j - 1)/2$ is the number of pairs at site j , which all interact with strength U . The action of the Bose-Hubbard Hamiltonian is illustrated in Fig. 7.7. Usually, the Bose-Hubbard model only include tunneling between nearest-neighbor sites,

but as already argued in Sec. 7.2 couplings beyond nearest-neighbor may be of great importance, and is crucial for understanding four-wave mixing.

We can use the number states as our basis for the Bose-Hubbard model

$$|n_1, \dots, n_j, \dots\rangle = \prod_j (\hat{a}_j^\dagger)^{n_j} |vac\rangle \quad (7.23)$$

with n_j atoms at the j th site of the lattice. In the number basis any state can be expanded as

$$|\Psi\rangle = \sum_{n_1, \dots, n_j, \dots} c_{n_1, \dots, n_j, \dots} |n_1, \dots, n_j, \dots\rangle. \quad (7.24)$$

This will leave us with $(M + N)!/M!N!$ coefficients for a lattice with N particles and M lattice sites. Already for relative small numbers of lattice sites and particles, this becomes an intractably large Hilbert space. Therefore, we will need to simplify the dynamics. This we will do by two very different methods, the Gutzwiller approximation and the truncated Wigner method covered in the next section. But first we will give some general comments on the Bose-Hubbard model.

If we apply the mode operators to a condensate state, here defined as an eigenstate of the field operator (7.13), we find that the condensate is also an eigenstate of the mode operators

$$\hat{a}_j |\psi_N\rangle = \int d^3\mathbf{x} w_j(\mathbf{x})^* \hat{\Psi}(\mathbf{x}) |\psi_N\rangle = \alpha_j |\psi_N\rangle \quad (7.25)$$

with eigenvalue $\alpha_j = \int d^3\mathbf{x} w_j(\mathbf{x})^* \psi_N(\mathbf{x})$. Therefore characterizing the condensate by the function $\psi_N(\mathbf{x})$ or the set of amplitudes $\{\alpha_j\}_{j \in \mathbb{Z}}$ is equivalent. Recall that the coherent state of an operator \hat{a} with eigenvalue α is given by

$$|\alpha\rangle = e^{-|\alpha|^2/2} \sum_n \frac{\alpha^n}{\sqrt{n!}} |n\rangle, \quad (7.26)$$

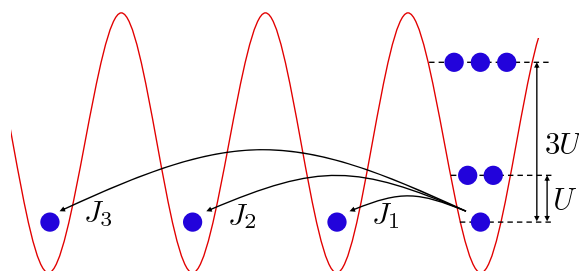


Figure 7.7: Dynamics in the Bose-Hubbard model. The J_d -coefficients are the tunneling amplitudes and $Un(n-1)/2$ is the energy of having n particles at the same lattice site.

and has mean occupation number $\langle \hat{n} \rangle = |\alpha|^2$ and variance $\text{var}(n) = |\alpha|^2$. It is a peculiarity of the perfect condensate that it is a product state, *i.e.*,

$$|\psi_N\rangle = \prod_j \left[\sum_n \frac{(\alpha_j \hat{a}_j^\dagger)^n}{n!} \right] |vac\rangle = \prod_j |\alpha_j\rangle. \quad (7.27)$$

We will use a perfect condensate with all atoms in a specific Bloch state with quasi-momentum q as the starting point in our simulations. This is only the exact eigenstate of the Hamiltonian when there is no interaction, $U = 0$. The quasi-momentum mode operators are given by

$$\hat{a}_q = \int d^3\mathbf{x} \phi_{1q}(\mathbf{x})^* \hat{\Psi}(\mathbf{x}) = \frac{1}{\sqrt{M}} \sum_j e^{-iqz_j} \hat{a}_j \quad (7.28)$$

and vice versa

$$\hat{a}_j = \frac{1}{\sqrt{M}} \sum_q e^{iqz_j} \hat{a}_q \quad (7.29)$$

where \hat{a}_q^\dagger (\hat{a}_q) creates (destroys) a particle in a Bloch state with quasi-momentum q . If the whole condensate is in the q -mode, we have $\alpha_q = \sqrt{N}$ and thus, according to Eq. (7.29), $\alpha_j = \alpha_0 e^{iqz_j}$ with $\alpha_0 = \sqrt{N/M}$. This will be our starting conditions in the unseeded simulations below. Here M is the number of lattice sites and N the total amount of atoms. In order to seed the four-wave mixing a fraction of atoms is transferred to a different quasi-momentum state by a two-photon process. This is described by a perturbation of the form $\hat{H}' = \gamma \hat{a}_{q'}^\dagger \hat{a}_q + \gamma^* \hat{a}_q \hat{a}_{q'}^\dagger$. If the applied pulse is short, we can ignore all but H' in the evolution under the pulse, and the mode operators evolves according to

$$i\dot{\hat{a}}_q = [\hat{H}', \hat{a}_q] = -\gamma \hat{a}_{q'} \quad \text{and} \quad i\dot{\hat{a}}_{q'} = [\hat{H}', \hat{a}_{q'}] = -\gamma \hat{a}_q \quad (7.30)$$

or equivalently $\ddot{\hat{a}}_q = \hat{a}_q$ and $\ddot{\hat{a}}_{q'} = \hat{a}_{q'}$. The general solution is of the form

$$\hat{a}_q(t) = \cos(\gamma t) \hat{a}_q(t=0) + \sin(\gamma t) \hat{a}_{q'}(t=0) \quad (7.31a)$$

$$\hat{a}_{q'}(t) = \sin(\gamma t) \hat{a}_q(t=0) + \cos(\gamma t) \hat{a}_{q'}(t=0) \quad (7.31b)$$

Knowing the time evolution of the operator and starting from an initial state $\hat{a}_q(t=0)|\psi_N\rangle = \sqrt{N}|\psi_N\rangle$ and $\hat{a}_{q'}(t=0)|\psi_N\rangle = 0$, we have $\alpha_q(t_{\text{end}}) = \cos(\gamma t_{\text{end}})\sqrt{N}$ and $\alpha_{q'}(t_{\text{end}}) = \sin(\gamma t_{\text{end}})\sqrt{N}$ after the pulse. Here t_{end} is the duration of the pulse and the seeded fraction is $|\alpha_{q'}(t_{\text{end}})|^2/N$ or simply $\sin^2(\gamma t)$.

If the interaction strength is non-zero we observe that adding the $(n+1)$ th particle to a mode requires the energy

$$\frac{U}{2} [(n+1)n - n(n-1)] = nU, \quad (7.32)$$

and therefore the energy matching in the four-wave mixing, Eq. (7.2b), becomes dependent on the mode populations, as also briefly discussed in the

introduction. In the limit, where $U \gg J$, this energy dominates the dynamics and the ground state will have a fixed number of atoms per site, provided that the mean occupation $\bar{n} = N/M$ is an integer. This is called a Mott insulator and is conveniently written

$$|\text{MI}, \bar{n}\rangle = \prod_j \left(\hat{a}_j^\dagger \right)^{\bar{n}} |vac\rangle. \quad (7.33)$$

A phase transition between this and the superfluid state Eq. (7.27) occurs as U exceed $U_c \simeq 5.8zJ$ (for $\bar{n} = 1$), where z is the number of nearest-neighbor sites, *i.e.*, two times the number of dimensions for a cubic lattice [28, 113]. (If U exceeds U_c but \bar{n} is not an integer, there is no transition to a Mott insulator state for a translationally invariant lattice. However, this is a theoretical abstraction, since in experiments there is always some inhomogeneities and in this case the atoms will arrange themselves in disks with integer fillings.)

If we had expanded the second quantized Hamiltonian on the Bloch waves instead, we would have obtained the Hamiltonian

$$\hat{\mathcal{H}} = - \sum_q E(q) \hat{a}_q^\dagger \hat{a}_q + \frac{aU}{4\pi} \sum_{q_0, q_1, q_2, q_3} \hat{a}_{q_3}^\dagger \hat{a}_{q_2}^\dagger \hat{a}_{q_1} \hat{a}_{q_0}, \quad (7.34)$$

where the summations are over the first Brillouin zone. We also used the fact that on-site interaction for Wannier functions is equivalent with a constant interaction $\langle k' | \hat{U} | k \rangle = aU/2\pi$ between any two relative quasi-momenta, $k = q_0 - q_1$ and $k' = q_2 - q_3$ (cf. Sec. 3.4.2).

7.5 The Gutzwiller approximation

As argued above it is in general impossible to solve the Bose-Hubbard model directly and we have to introduce some approximations to make the problem numerically feasible.¹ The first method we will apply is the Gutzwiller approximation, in which the product ansatz

$$|\Psi\rangle \simeq |G : f\rangle = \prod_j \left(\sum_{n=0}^{\infty} f_n^j |n\rangle_j \right) \quad (7.35)$$

is assumed. Here $\sum_{n=0}^{\infty} f_n^j |n\rangle_j$ is the state of the j th site in the lattice and f_n^j is the amplitude of having n atoms at the site j denoted by the number states $|n\rangle_j$. The probability of finding n atoms at site j is given by $P(n, j) = |f_n^j|^2$, and summing over all possible measured number of atoms at site j , it gives the normalization requirement

$$\sum_n P(n, j) = \sum_{n=0}^{\infty} |f_n^j|^2 = 1, \quad (7.36)$$

¹It should be noted that faster and more accurate methods are available, see for example [114]. The advantages of the two presented methods are their simplicity and the fast implementation.

i.e., each site has to be normalized on its own.

We note that the correct eigenstates of both the extreme limits $J/U = 0$ and $J/U = \infty$ are correctly reproduced by the Gutzwiller Ansatz. In the first limit we have a Mott insulator (7.33) and simply have $f_n^j = \delta_{n,\bar{n}}$ for all lattice sites ($\bar{n} \in \mathbb{N}_0$ assumed), and in the latter limit we have a coherent state (7.27) with $f_n^j = \alpha_n^j / \sqrt{n!}$. This state will be used to initialize the calculations below based on the coherent states devised in Eq. (7.31).

The time evolution of the f_n^j -coefficients is obtained from the time-dependent variational principle [115]

$$0 = \frac{\delta}{\delta f_n^{j*}} \langle G : f | i \frac{\partial}{\partial t} - \hat{\mathcal{H}}_{\text{BH}} | G : f \rangle, \quad (7.37)$$

which leads to

$$i \dot{f}_n^j = -\sqrt{n+1} \psi_j^* f_{n+1}^j - \sqrt{n} \psi_j f_{n-1}^j + U n(n-1) f_n^j. \quad (7.38)$$

For simplicity we have set $\hbar = 1$ and introduced

$$\psi_j = \sum_{\substack{d=-\mathcal{D} \\ d \neq 0}}^{\mathcal{D}} J_d \langle \hat{a}_{j+d} \rangle, \quad (7.39)$$

which is a weighted sum over c-numbers of the neighboring mode operators, $\langle \hat{a}_{j+d} \rangle = \sum_n \sqrt{n} f_n^{j*} f_{n+1}^j$. We note that the c-numbers measure the coherent fraction of atoms $N_{\text{coh}} = \sum_n |\langle \hat{a}_{j+d} \rangle|^2$ and if they vanish, the condensate is lost. Moreover, if the c-numbers vanish, the two first terms on the right of Eq. (7.38) disappears and there is nothing left of the kinetic and lattice part of the original Hamiltonian. From the sketched derivation it is not clear, when the Gutzwiller approximation is valid. In App. B a different derivation is provided, which shows that the Gutzwiller approach is equivalent to a mean field approximation for the kinetic and lattice part of the Hamiltonian, *i.e.*, for the tunneling part $-\sum_j \sum_{d=1}^{\mathcal{D}} J_d (\hat{a}_j^\dagger \hat{a}_{j+d} + \hat{a}_{j+d}^\dagger \hat{a}_j)$, whereas the on-site interaction is treated correctly. Furthermore, the derivation in App. B shows how to make the Gutzwiller approximation exact by introducing stochastic noise.

For all practical purposes the sum over the number of atoms at the individual lattice sites n_j can be truncated at some upper bound N_{max} . The Gutzwiller approximation, hence, reduces the parameter space for the case of M sites to be $M(N_{\text{max}} + 1)$ -dimensional.

7.6 The truncated Wigner method

Replacing the mode operators with c-numbers in the Bose-Hubbard Hamiltonian and applying the time-dependent variational principle will in analogy

with Eq. (7.14) give the discrete Gross-Pitaevskii equation

$$i\dot{\alpha}_j = - \sum_{d=1}^{\mathcal{D}} J_d \alpha_{j+d} + U \alpha_j |\alpha_j|^2. \quad (7.40)$$

This happens to be identical to the equation for the trajectories found by different means in the truncated Wigner approximation [109, 116–118]. In the truncated Wigner approach we have to sample the initial values $\alpha_j(t=0)$ according to the zero-temperature Wigner function

$$W(\tilde{\alpha}_j, \tilde{\alpha}_j^*) = \frac{1}{2\pi\sigma^2} \exp\left(-\frac{|\tilde{\alpha}_j - \alpha_j|^2}{2\sigma^2}\right) \quad (7.41)$$

with $\sigma = 1/2$ for a zero-temperature Bose-Einstein condensate. The Wigner function serves as a probability distribution, and each trajectory has to be propagated according to Eq. (7.40).

The truncated Wigner method is not exact, and it is difficult to estimate the error. However, it is in general reasonable if the number of particles are much larger than the number of modes [116]. The expectation value of the mode operators is found as the average of the c-numbers over all trajectories,

$$\langle \{\hat{a}_i^n (\hat{a}_j^\dagger)^m\}_{\text{sym}} \rangle = \langle \alpha_i^n (\alpha_j^*)^m \rangle_W, \quad (7.42)$$

where $\langle \cdot \rangle_W$ is the average over all trajectories and $\{\hat{a}_i^n (\hat{a}_j^\dagger)^m\}_{\text{sym}}$ is the Weyl symmetric form, *e.g.*, $\{\hat{a}_i \hat{a}_j^\dagger\}_{\text{sym}} = (\hat{a}_i \hat{a}_j^\dagger + \hat{a}_j^\dagger \hat{a}_i)/2$. In particular we have the mean occupation number

$$\langle \hat{n}_j \rangle = \langle \alpha_j^* \alpha_j \rangle_W - \frac{1}{2} \quad (7.43)$$

and the number of coherent atoms are

$$N_{\text{Coh}} = \sum_n |\langle \hat{a}_j \rangle|^2 = \sum_n |\langle \alpha_j \rangle_W|^2. \quad (7.44)$$

A coherent state is always coherent, but the opposite is not necessarily correct, since the moments of the mode operator has to fulfil $\langle (\hat{a}^\dagger)^m \hat{a}^n \rangle = (\alpha^*)^m \alpha^n$ for the state to be a coherent state. However, coherence is still of utmost importance if we want to observe interference. Note that the two results, Eqs. (7.43) and (7.44), are also valid for quasi-momentum operators, the conversion follows from Eqs. (7.28) and (7.29). We could just as well have derived a discrete Gross-Pitaevskii equation for the quasi-momentum states

$$i\dot{\alpha}_q = E(q)\alpha_q + \frac{aU}{2\pi} \sum_{q', q'', q'''} \alpha_{q'}^* \alpha_{q''} \alpha_{q'''} \delta(q + q' - q'' - q''') \quad (7.45)$$

following [109, 116, 119]. From this equation it is easy to understand the Bose-stimulation, because the more populated the q' , q'' and q''' modes are,

the stronger the coupling term in Eq. (7.45) is. Furthermore, we see that if only the q -mode is populated the right hand side of Eq. (7.45) is zero, and hence there will be no four-wave mixing in the discrete Gross-Pitaevskii equation. This is why we need to go beyond the mean field theory to simulate *spontaneous* four-wave mixing. The truncated Wigner method solves this problem by adding quantum fluctuations to the initial states, which leads to non-vanishing amplitude of all modes in every single trajectory, but on average the initial occupation is, however, still zero, cf. Eq. (7.43).

7.7 Simulations

We first present results for a quasi-one-dimensional lattice with lattice strength $V_0 = 1$, a low filling factor of $\bar{n} = 4$ atoms per site and $M = 29$ lattice sites. In this regime we can use both the Gutzwiller approximation and the truncated Wigner method and hence compare the results. In the Gutzwiller approximation we have set the cutoff to $N_{\max} = 20$, which leaves us 609 coefficients to solve for, which can still be done reasonably fast on a standard laptop. We assume cyclic boundary conditions in all simulations, which means that the atoms can tunnel from one end to the other, *e.g.*, the M th site can tunnel to the d th site with amplitude J_d .

Recall that on a finite lattice only a finite number of discrete quasi-momentum states are allowed,

$$q = 2\pi n/aM, \quad n = 0, \dots, M-1, \quad (7.46)$$

therefore we can in general not expect to find three quasi-momenta that simultaneously fulfil both criteria in Eq. (7.2) exactly. However, it is readily verified that for the following three quasi-momenta the criteria are almost fulfilled:

$$q_0 = 0.62\pi/a, \quad q_1 = 1.10\pi/a, \quad \text{and} \quad q_2 = 0.14\pi/a. \quad (7.47)$$

This is the quasi-momenta shown in Fig. 7.2.

First we apply our numerical methods with a seed of 1% in the q_1 -mode. In Fig. 7.8(a) we compare the truncated Wigner method (solid lines) with the result of the discrete Gross-Pitaevskii equation (dashed lines), Eq. (7.40). The latter can be seen as a single trajectory of the truncated Wigner method. Only the population of the three modes in Eq. (7.47) is shown, since the other modes hardly get populated (the remaining modes is occupied by less than 2.3 particles during the simulated time). The discrete Gross-Pitaevskii calculations shows Rabi oscillations between the q_0 -mode and the q_1 - and q_2 -modes in agreement with the findings in Ref. [24], where the continuous Gross-Pitaevskii equation was solved. In the truncated Wigner calculation the oscillation dies out due to dephasing (in agreement with the findings in Ref. [25, 117]), because the different coherent components acquire different phases over time. In the shown calculations 20000 trajectories have been averaged. As a measure of convergence the relative error of $\langle \alpha_q^* \alpha_q \rangle_W$ in going

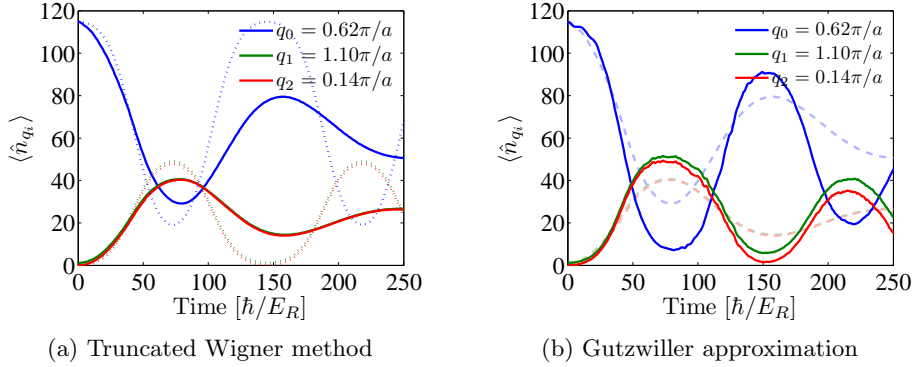


Figure 7.8: Four-wave mixing with 1% seeding in q_2 . Other parameters: mean occupation $\bar{n} = 4$, $M = 29$ lattice sites and on-site interaction $U = 0.01J$. (a): The solid lines are obtained by the truncated Wigner method and as dotted lines the solution to the discrete Gross-Pitaevskii equation, Eq. (7.40), is included. (b): Results for the Gutzwiller approximation. The dashed lines are identical to the solid lines in (a) and included for comparison. The time scale is in units of $\hbar/E_R \simeq 0.8$ ms for rubidium.

from 10000 to twice the number of trajectories was less than 10^{-3} for all sites.

In Fig. 7.8(b) we have solved the same problem with the Gutzwiller approximation. We see that compared to the pure mean-field discrete Gross-Pitaevskii equation (dotted line in Fig. 7.8(a)) it shows some dephasing. However, this dephasing happens at a slower time scale than in the truncated Wigner calculation. This is probably because of the mean field character of the method. Recall that the Gutzwiller approximation treats the lattice Hamiltonian $\hat{\mathcal{H}}_{\text{lat}}$ according to the mean-field method (see Sec. 7.5 and App. B). It should be noted that the effectiveness of the process is highly dependent on the energy matching of the modes, and as discussed above this is limited by the discretization in quasi-momentum in our numerical implementation.

Next we have compared different seedings in Fig. 7.9. The full line is without seeding and the first thing one should note is that the conversion occurs at all. This is not the case for the Gutzwiller simulation shown as the dotted line. This emphasizes the need to go beyond mean field to simulate this process. Seedings of 1% and 5% in q_2 are included as dashed and dot-dashed curves, respectively. For the 5% seed we see a prevailing difference in occupation of q_1 and q_2 , whereas they are equally populated for the unseeded process. We note that the less seeding the slower the four-wave mixing process, and consequently, the conversion efficiency is lowered due to the ongoing dephasing. The number of coherent atoms are shown in Fig. 7.10. We observe for the truncated Wigner calculations that for large seeding a larger part of the atoms stays in a coherent state for a longer time. In a stimulated process the

phase of the two scattered atoms is fixed and not random as it may be in the unstimulated process. Moreover, if the outcoupling of the atoms from the initial coherent state happens over a shorter time period, the phase acquired from time evolution will be less significant, and therefore the outcoupled atoms will have the same phase. Moreover, we have plotted the coherent fraction for the Gutzwiller simulation with 1% seeding as the gray line in Fig. 7.10, and we observe that the coherent fraction of atoms is only very slowly depleted in agreement with the conclusion above: mean-field calculation cannot sufficiently simulate this process.

Finally, we have made simulations based on parameters from the experiment by Campbell *et al.* [25]. In this experiment a weak lattice with lattice strength $V_0 = 0.5$ is applied along the axis of an elongated rubidium condensate. The transverse trapping was due to the magnetic trap with a trapping frequency of 35 Hz. This is not in the quasi-one-dimensional regime, but we will apply the theory anyway, since the trapping still reduces the number of resonant outgoing modes. The on-site coupling is in this case as low as

$$U \approx 2.4 \times 10^{-4} J_1 \quad (7.48)$$

and the average site occupation is of the order $\bar{n} \sim 1000$ atoms. The tunneling coefficients can be found in Tab. 2.1. Campbell *et al.* perform the experiment both with a small seed up to 5% and without seeding. We present simulations for both scenarios, see Figs. 7.11 and 7.12. We have included $M = 200$ lattice sites to ensure high resolution of the quasi-momentum states, and we have chosen the three modes in accordance with the experimental parameters;

$$q_0 = 0.66\pi/a, \quad q_1 = 0.19\pi/a, \quad \text{and} \quad q_2 = 1.13\pi/a. \quad (7.49)$$

The seeding was done in mode q_1 . We note that in this simulation we have $N \gg M$, which is the condition for applying the truncated Wigner method.

Most importantly, we note that the truncated Wigner is capable of simulating the process in both cases. If we first look at the seeded process, it is remarkable that the initial coherent fraction remains almost intact while the q_0 -mode is reduced to only 7.5% of its initial population, *i.e.*, the two new modes are phase coherently populated. The high conversion efficiency measured here, is in the experiment limited by the vanishing overlap between the modes, because the atoms move apart. The overlap vanishes after 6-8 ms in the experiment and that is long before the mixing has peaked. Note the time scale on the figures in this section is in units of $\hbar/E_R \simeq 0.8$ ms.

Without seeding the coherence decays along with the population of the q_0 -mode. Note that we do not control which modes get populated if we do not seed, and a whole range of quasi-momenta centered around q_0 , q_1 and q_2 gets populated. Therefore the solid curves show the occupations in an $\pm 0.1\pi/a$ interval around the modes listed in Eq. (7.49), whereas the dashed curves show the population of the single modes, q_0 , q_1 and q_2 . We observe that the coherence is lost along with the initial condensate (cf. blue and black dashed lines). This is because (i) no predefined phase is specified when the

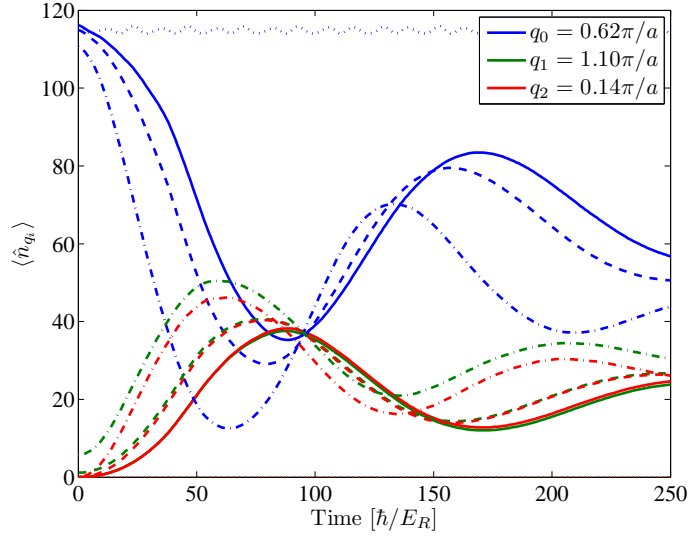


Figure 7.9: Four-wave mixing with different amount of seeding. The solid lines are for simulation without seeding, the dashed lines are for 1% seed (identical to the solid curves in Fig. 7.8) and the dash-dotted lines show the calculations for 5% seeding. We have included the result from a Gutzwiller approximation as the dotted line. Here only the q_0 -mode was significantly populated.

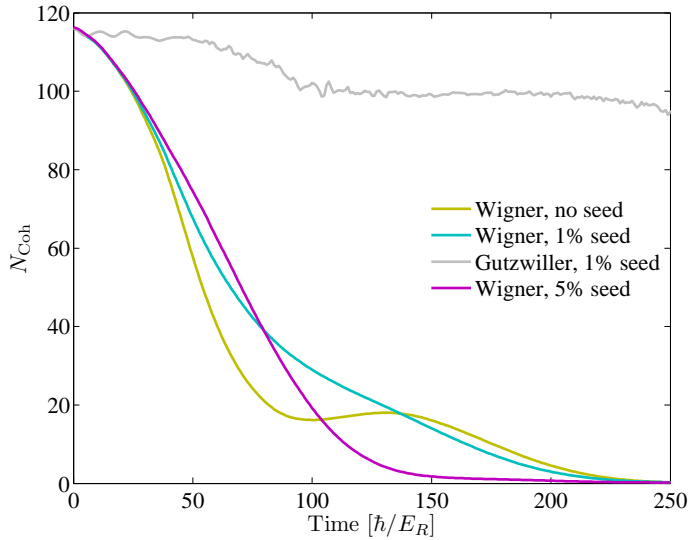


Figure 7.10: The number of coherent atoms, $N_{\text{Coh}} = \sum_n |\langle \hat{a}_j \rangle|^2$, for simulations with 0%, 1% and 5% seeding for the truncated Wigner method. The result from a Gutzwiller simulation with 1% seeding is plotted with gray.

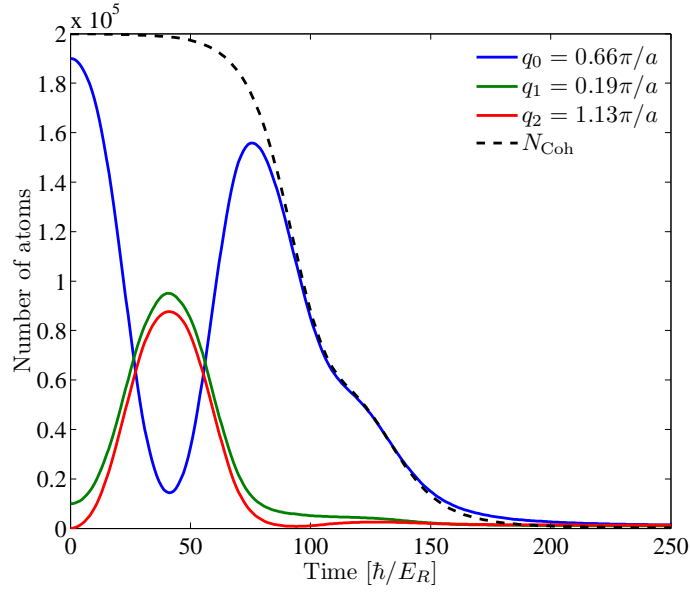


Figure 7.11: Population of the modes in Eq. (7.49) obtained by the truncated Wigner method and a 5% seed in the q_1 -mode. The dashed black dashed line is the number of coherent atoms.

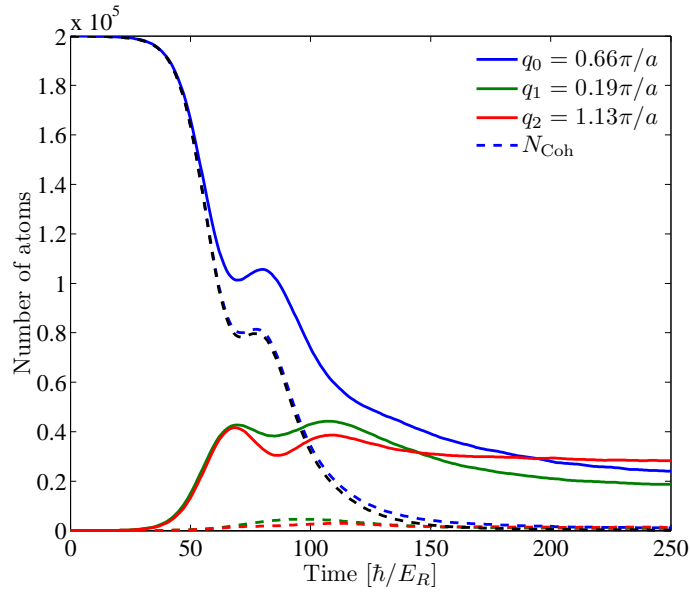


Figure 7.12: Population of the modes in Eq. (7.49) obtained by the truncated Wigner method without seeding. The dashed curves show the population of the single modes, Eq. (7.49), whereas the solid lines include the population in the nearby modes in an interval $q_i \pm 0.1\pi/a$. The black dashed line is the number of coherent atoms.

atoms scatter into new modes, and secondly when the atoms couples back into the q_0 or a nearby mode, they have collected different phases depending on which mode they have been occupying, and this will eventually kill the mother condensate. We note that after the Rabi oscillation has peaked and the atoms start to couple back, we begin to populate states near the q_0 -mode as seen from the separation of the solid and dashed blue lines. Finally, we observe that all plotted modes eventually decays.

7.8 Conclusion

The theme throughout this chapter has been when four-wave mixing is and is not possible, and this problem has been discussed in terms of both few-body and many-body theory. Our interest is in the special one-dimensional four-wave mixing where only one quasi-momentum component is populated at the beginning:

$$2q_0 = q_1 + q_2 \pmod{2\pi/a}, \quad (7.2a)$$

$$2E(q_0) = E(q_1) + E(q_2). \quad (7.2b)$$

We started out, based only on the single-body spectrum, by arguing that this process is never possible in free space, but if a lattice is applied along the direction of motion it is possible (see Fig. 7.2). However, we also argued that in a discrete model it is imperative to include tunneling between more than nearest-neighboring sites in the lattice. This follows because the single-body energy dispersion is a cosine function if only nearest-neighbor tunneling is included and a cosine dispersion does not feature the requisite degeneracies.

Thereafter we analyzed the process in terms of two-body theory [Sec. 7.2]. From which we arrived at the same conclusion as in the single-body analysis that the first Bloch band is capable of explaining the four-wave mixing provided that more than nearest-neighbor tunneling is included. The two-body analysis allowed us to obtain an interval in which this four-wave mixing takes place, namely,

$$\pi/2a < q_0 < q_{\text{inf}}, \quad (7.6)$$

where q_{inf} is the point of inflection of the single-particle dispersion curve, which coincides with $\pi/2a$ for a cosine dispersion. Furthermore, the two-body description revealed that in general the quasi-momenta of two atoms have to fulfil

$$\epsilon_K(\pi/a) < E(q_A) + E(q_B) < \max_k \epsilon_K(k), \quad (7.7)$$

for four-wave mixing to be allowed in a one-dimensional lattice.

After having discussed the process from the few-body perspective we wanted to simulate the process and for this purpose we needed the full many-body physics. We provided a rough derivation of the Bose-Hubbard Hamiltonian, which consists of mode operators creating or annihilation atoms in the localized Wannier functions. The assumptions applied to obtain the Bose-Hubbard model are identical to those introduced in the previous chapters: a homogeneous translationally invariant lattice and a short-range two-body interaction

potential. Furthermore, the parameters of the Hamiltonian, *i.e.*, J_d and U , coincides with those from the two-body model. However, further approximations were needed to reduce the Hilbert space in order to make the time propagation numerical feasible, and we introduced two methods: the Gutzwiller approximation [Sec. 7.5] and the truncated Wigner method [Sec. 7.6]. The Gutzwiller approach, we argued, is partly a mean-field calculation, since it does not properly incorporate the tunneling part of the Hamiltonian and cannot describe correlations between lattice sites [App. B]. The simulation showed four-wave mixing if seeded, but in agreement with other mean-field approaches it could not describe the unseeded process. Moreover, the atoms retained coherence much longer in the Gutzwiller simulation than in the truncated Wigner simulations, which also may be a signature of the mean-field method.

The other numerical approach, the truncated Wigner method, is a phase space technique, where quantum fluctuations is introduced by sampling the ($t = 0$)-state with respect to the zero-temperature Wigner distribution. The sample states are propagated according to the discrete Gross-Pitaevskii equation. We showed that this process reproduces the four-wave mixing both for the seeded and unseeded processes. Applied to the physical system from the paper by Campbell *et al.* [25], it not only reproduces the four-wave mixing, but it also predicts that the atoms stay coherent until after the population of the q_1 and q_2 modes has peaked.

In the future it could be very interesting to apply our beyond nearest-neighbor two-body model and many-body techniques to an experiment with a shaken lattice like, *e.g.*, Gemelke *et al.* [26], where they observed Rabi oscillations between the zone center, $q = 0$, and boundary, $q = \pm\pi/a$. In a shaken lattice the Hamiltonian become time dependent and energy is hence not conserved. However, the system can be described by a set of dressed states with a quasi-energy dispersion, and for the right amplitude and frequency of the modulation, the zone center and boundary become degenerate [93]. The effective band structure can be obtained from Floquet theory and given that, it should be possible to apply all the machinery above to the problem. It would also be interesting in the near future to calculate the pair correlations for the four-wave mixing process

$$\text{Var}(\hat{n}_{q_1} - \hat{n}_{q_2}) \tag{7.51}$$

which is important in precision measurements.

Chapter 8

Conclusion and outlook

I have presented a discrete theoretical model describing a physical system consisting of two ultracold atoms in a one-dimensional periodic potential. Periodic potentials in effectively one-dimensional gases are readily realized in experiments and in those experiments the two-body dynamics are of utmost importance, because the density and the temperature are such that collisions between three and more atoms can be safely ignored, leaving only two-body interactions to rule the many-body physics. This point was illustrated in Chapter 7, where we analyzed an inherently many-body phenomenon, namely four-wave mixing, with both single-particle, two-particle and many-particle methods. The two-body description provided valuable insight into the four-wave-mixing process, such as setting up criteria for when it is possible. Moreover, it explained the importance of allowing atoms to jump between sites that are not necessarily adjacent when modeling four-wave mixing. Four-wave mixing is a very interesting process, because it illustrates the analogy between quantum optics and ultracold atom physics, and furthermore, because it may be a useful tool in precision measurements serving as a source of coherent atoms and in quantum computing by producing macroscopically populated entangled states.

However, the source of inspiration for our investigation of two-body dynamics came from a completely different type of experiments probing scattering and bound state properties of isolated pairs of atoms in a periodic potential. The periodic potential breaks the continuum up into separated bands, and in between those bands bound pairs of repulsive atoms can exist, and in the recent experiment by Winkler *et al.* both energy and wave function of such repulsively bound pairs were measured. The foundation of the two-body formalism is provided Chapter 3, where a discrete analytical model was devised in terms of Green's functions. The Green's function formalism was coupled to the scattering amplitude leading to other important quantities such as the scattering length and the phase shift. Moreover, we introduced spectral functions to characterize how the spectral weight was distributed over bound and continuum states. In the context of the discrete lattice model everything could be attained by purely analytical arguments.

In Chapter 4, the two-body method was extended to a two-channel model,

in which a molecular bound state with tunable energy offset with respect to the atomic continuum band was included. This type of system gives rise to a Feshbach resonance, and has found numerous applications in cold atom physics, since it can be used to both produce molecules and adjust the interatomic interaction strength. We exploited the interplay between the structured continuum and the tunable state. This led to, in my opinion, very interesting suggestions such as, *e.g.*, the existence of *motionally* bound states, where a bound state only exist if the center-of-mass quasi-momentum exceeds a critical value, and the possibility of molecular sweep experiments, where a molecular state is scanned through the continuum band to a stable region *above* the continuum.

Recent cooling schemes have made it possible to have ultracold atomic gases of mixed species. Therefore, we extended the theory in Chapter 5 to also account for heteronuclear pairs. The main result was that the discrete two-body model is readily generalized to heteronuclear atoms, but we also found new features such as a phase shift of the two-body scattering spectrum, which, we argued, can be measured experimentally. Furthermore, in Chapter 6 we included tunneling between distant lattice sites into the discrete two-body formalism to improve the approximate Bloch dispersion modeled. This significantly changed the continuum spectrum and the bound states. There appeared an extra singularity in the continuum spectrum - a divergence that in Chapter 7 proved to be crucial in the explanation of the four-wave mixing.

8.1 Outlook

A natural extension of our present work would be, first of all, to pursue the ideas of Appendix A, Sec. A.3. In Chapter 6 the Green's function including beyond nearest-neighbor tunneling was obtained by numerical integration, which prevented us from identifying the scattering amplitude and derive analytical expressions for the bound states. However, we showed in Appendix A that the Green's function by means of complex contour integration *can* be obtained analytically at least for the case with next-nearest-neighbor tunneling. This will most likely allow us to write up analytical expressions for the scattering amplitude, transmission coefficient and many other quantities already derived for the two-body model with nearest-neighbor tunneling. Moreover, it could be interesting in connection with the two-channel model devised in Chapter 4 to include coupling of the molecular state to atoms not necessarily located at the same lattice site. We have promising ideas on how to accomplish this. Finally, it would be interesting to apply the analysis of the two-body and many-body theory with next-nearest-neighbor tunneling devised in Chapter 7 to a shaken lattice as experimentally studied by, *e.g.*, Gemelke *et al.*, where it was argued that the periodic modulation of the periodic potential induces an effective band structure in which the center and zone boundary become degenerate - a scenario we can model by choosing the tunneling couplings carefully.

The experimental progress in cold atom physics is fast and I strongly be-

lieve that we also in the future will see many interesting experiments. We will continue to see experiments enlightening the splendor of fundamental quantum mechanics, but also more application-oriented experiments both in the direction of quantum computing and high-precision measurements. Hopefully, demonstrations of our experimental suggestions will be among them.

Appendix A

Various useful calculations

A.1 Normalization of Bloch waves

A.1.1 Single-particle wave functions

The solutions to the single-particle lattice Hamiltonian, Eq. (2.4), are Bloch waves, which in the Wannier basis take the form $|\phi_{nq}\rangle = \sum_{z_j} \psi_q(z_j) |w_{nz_j}\rangle$ with

$$\psi_q(z) = \alpha \exp(iz). \quad (\text{A.1})$$

Here z is the quasi-position of the Wannier states and α is the normalization factor to be determined. We only consider a one-dimensional lattice. On an infinite lattice the eigenstates (A.1) cannot be normalized, since

$$\sum_z |\psi_q(z)|^2 = \infty \quad \text{for } \alpha \neq 0.$$

This does not mean that the Bloch waves are unphysical, but that real physical states necessarily have to be normalizable linear combinations of (A.1). We will, however, need a convention on how to choose the norm in order to ensure consistency. Because the quasi-momentum is a continuous coordinate, the requirement will be of the form

$$\langle \psi_{q'} | \psi_q \rangle = \beta \delta(q - q'), \quad (\text{A.2})$$

where we choose $\beta = 1$. From the well known formula $\sum_{n \in \mathbb{Z}} e^{int} = 2\pi \delta(t)$, we can now determine the normalization constant:

$$\langle \psi_{q'} | \psi_q \rangle = \sum_{j \in \mathbb{Z}} |\alpha|^2 e^{i(q-q')aj} = 2\pi |\alpha|^2 \delta(qa - q'a) = \frac{2\pi}{a} |\alpha|^2 \delta(q - q') \quad (\text{A.3})$$

We see that $\alpha = \sqrt{a/2\pi}$ will do the job, and the normalized wave functions become

$$\psi_q(z) = \sqrt{\frac{a}{2\pi}} \exp(iz). \quad (\text{A.4})$$

A.1.2 Two-particle wave functions

For the noninteracting two-particle lattice Hamiltonian [see Eqs. (5.5) and (6.1)] the eigenstates are products of single-particle Bloch waves,

$$\psi_{q_A, q_B}(z_A, z_B) = \frac{a}{2\pi} \exp(iq_A z_A) \exp(iq_B z_B), \quad (\text{A.5})$$

where

$$\langle \psi_{q'_A, q'_B} | \psi_{q_A, q_B} \rangle = \delta(q_A - q'_A) \delta(q_B - q'_B) \quad (\text{A.6})$$

is inherited from Eq. (A.2). In terms of center-of-mass (collective) and relative coordinates this becomes

$$\langle \psi_{K', k'} | \psi_{K, k} \rangle = \delta(K - K') \delta(k - k'). \quad (\text{A.7})$$

The conversion between the two sets of coordinates is addressed in Sec. 3.2.

When we split the wave function into a center-of-mass and a relative coordinate part, $\psi_{K, k}(Z, z) = \Psi_K(Z) \psi_{K, k}(z)$, it is natural to require each part to fulfil the same normalization requirement as in Eq. (A.2), *i.e.*,

$$\langle \psi_{K, k} | \psi_{K, k'} \rangle = \delta(k - k') \quad \text{and} \quad \langle \Psi_K | \Psi_{K'} \rangle = \delta(K - K'). \quad (\text{A.8})$$

This is fulfilled if the two wave functions share the prefactor equally:

$$\Psi_K(Z) = \sqrt{\frac{a}{2\pi}} \exp(iKZ) \quad \text{and} \quad \psi_{K, k}(z) = \sqrt{\frac{a}{2\pi}} \exp(ikz). \quad (\text{A.9})$$

A.2 Derivation of the noninteracting two-body Hamiltonian for $\psi(x_A, x_B)$

In this section we determine the action of the noninteracting two-body lattice Hamiltonian on the discrete wave function $\psi(z_A, z_B)$ in the Wannier product basis:

$$\Psi(x_A, x_B) = \sum_{z_A, z_B} \psi(z_A, z_B) w_{z_A}(x_A) w_{z_B}(x_B), \quad (\text{A.10})$$

where x_A and x_B is the position coordinate of the atoms and $w_z(x)$ is the Wannier function centered at position z . In Dirac notation the above state can be written

$$|\Psi\rangle = \sum_{z_A, z_B} \psi(z_A, z_B) |w_{z_A}\rangle |w_{z_B}\rangle. \quad (\text{A.11})$$

Note that all considerations in this section is for one-dimensional lattices and we further omit the band index, focusing on a single Bloch band, say, the first.

The noninteracting two-body lattice Hamiltonian, $\hat{\mathcal{H}}_0 = \hat{\mathcal{H}}_0^A + \hat{\mathcal{H}}_0^B$, is the sum of two single-particle Hamiltonians,

$$\hat{\mathcal{H}}_0^\beta = - \sum_{z_\beta} J (|w_{z_\beta - a}\rangle \langle w_{z_\beta}| + |w_{z_\beta + a}\rangle \langle w_{z_\beta}|), \quad (\text{A.12})$$

where $\beta = A, B$ labels the atomic coordinate on which $\hat{\mathcal{H}}_0^\beta$ acts and J is the nearest-neighbor tunneling amplitudes. Applied to the state (A.11) above this gives

$$\begin{aligned} (\hat{\mathcal{H}}_0^A + \hat{\mathcal{H}}_0^B) |\Psi\rangle = -J \sum_{z_A, z_B} \psi(z_A, z_B) & \left[|w_{z_A-a}\rangle |w_{z_B}\rangle + \right. \\ & \left. |w_{z_A+a}\rangle |w_{z_B}\rangle + |w_{z_A}\rangle |w_{z_B-a}\rangle + |w_{z_A}\rangle |w_{z_B+a}\rangle \right] \end{aligned} \quad (\text{A.13})$$

and, if we change the summation variables,

$$\begin{aligned} -J \sum_{z_A, z_B} \left[\psi(z_A + a, z_B) + \psi(z_A - a, z_B) + \right. \\ \left. \psi(z_A, z_B + a) + \psi(z_A, z_B - a) \right] |w_{z_A}\rangle |w_{z_B}\rangle \end{aligned} \quad (\text{A.14})$$

Introducing the discrete Laplacian, $(\Delta_z + 2)f(z) = f(z + a) + f(z - a)$, we can rewrite this as

$$-J \sum_{z_A, z_B} [(\Delta_{z_A} + 2) + (\Delta_{z_B} + 2)] \psi(z_A, z_B) |w_{z_A}\rangle |w_{z_B}\rangle. \quad (\text{A.15})$$

Therefore, the action of the noninteracting two-particle lattice Hamiltonian on the wave function $\psi(z_A, z_B)$ is

$$H_0 = -J(\Delta_{z_A} + 2) - J(\Delta_{z_B} + 2). \quad (\text{A.16})$$

A.3 Calculation of the noninteracting Green's function

In this section we will calculate the integral [see Secs. 3.4 and 6.4]

$$G_K^0(E, z) = \int_{-\pi/a}^{\pi/a} \frac{dk}{2\pi} \frac{ae^{ikz}}{E - \epsilon_K(k) + i\eta} \quad (\text{A.17})$$

with the energy dispersion

$$\epsilon_K(k) = -4 \sum_{d=1}^{\mathcal{D}} J_d \cos(\frac{1}{2}Kad) \cos(kad), \quad (\text{A.18})$$

where \mathcal{D} is the maximal number of tunneling elements, J_d , included and $\eta > 0$ is a positive infinitesimal.

We will use the method of contour integrals, which states that for a closed contour Γ in the complex plane and a sufficiently well behaved complex function $f(x)$, one has

$$\int_{\Gamma} f = 2\pi i \sum_{x_i} \text{Res } f(x), \quad (\text{A.19})$$

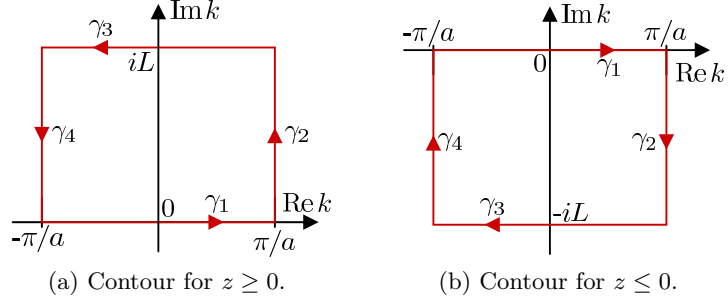


Figure A.1: Contours along which the integrations are performed. See text for details.

where x_i are the poles of f lying inside the contour Γ and $\text{Res}_{x_i} f(x)$ are the corresponding residues [120]. In the following we will take f to be the integrand of Eq. (A.17) and use the contours shown in Fig. A.1. Depending on the sign of the relative position coordinate z we will have to use either the contour in Fig. A.1(a) or that of Fig. A.1(b). Both contours have been split into four line integrals labeled by γ_i , $i \in \{1, 2, 3, 4\}$. We recognize $\int_{\gamma_1} f$ as the integral (A.17), whereas the other three curves are given by

$$\gamma_2 : \begin{cases} [0, L] \rightarrow \mathbb{C} \\ t \mapsto it + \pi/a \end{cases}, \quad \gamma_3 : \begin{cases} [-\pi/a, \pi/a] \rightarrow \mathbb{C} \\ t \mapsto iL - t \end{cases} \quad \text{and} \quad -\gamma_4 : \begin{cases} [0, L] \rightarrow \mathbb{C} \\ t \mapsto it - \pi/a \end{cases}, \quad (\text{A.20})$$

here written for $z \geq 0$. Note that $-\gamma_4$ is the contour γ_4 with the direction reversed and that t and L are in units of inverse length. We will in the following argue that $\int_{\gamma_2} f$ and $\int_{\gamma_4} f$ cancel out and that $\int_{\gamma_3} f$ vanish as L is increased. In that case the integral (A.17), $\int_{\gamma_1} f$, equals the residues inside the contour, when $L \rightarrow \infty$. First we show that γ_2 and γ_4 cancel:

$$\begin{aligned} \int_{\gamma_2} f &= \frac{a}{2\pi} \int_0^L \frac{e^{-zt} e^{iz\pi/a}}{E - \epsilon_K(it + \pi/a) + i\eta} dt \\ &= \frac{a}{2\pi} \int_0^L \frac{e^{-zt} e^{-iz\pi/a}}{E - \epsilon_K(it - \pi/a) + i\eta} dt = \int_{-\gamma_4} f \end{aligned} \quad (\text{A.21})$$

Here we used that $\cos(x + 2\pi p) = \cos(x)$ for all $p \in \mathbb{Z}$ and $x \in \mathbb{C}$, and that z is an integer multiple of the lattice constant a . Therefore, as promised above,

$$\int_{\gamma_2} f + \int_{\gamma_4} f = 0. \quad (\text{A.22})$$

The remaining integral is

$$\int_{\gamma_3} f = \frac{a}{2\pi} \int_{-\pi/a}^{\pi/a} \frac{e^{-zL} e^{-izt}}{E - \epsilon_K(iL - t) + i\eta} dt. \quad (\text{A.23})$$

We observe that $\epsilon_K(iL - t) \sim 2J_{\mathcal{D}}e^{-ia\mathcal{D}t}e^{a\mathcal{D}L}$ in the limit where $L \rightarrow \pm\infty$, therefore

$$\lim_{L \rightarrow \infty} \int_{\gamma_3} f = \frac{a}{2\pi} \lim_{L \rightarrow \infty} \int_{-\pi/a}^{\pi/a} \frac{e^{-zL}e^{izt}}{2J_{\mathcal{D}}e^{-ia\mathcal{D}t}e^{a\mathcal{D}L}} dt = 0, \quad (\text{A.24})$$

whenever $z > -a\mathcal{D}$. If $z \leq -a\mathcal{D}$, we have to close the contour in the lower complex half plane, this amounts to replacing L with $-L$ above (see Fig. A.1), and in that case we similarly find

$$\lim_{L \rightarrow -\infty} \int_{\gamma_3} f = 0 \quad (\text{A.25})$$

for all $z < a\mathcal{D}$.

It only remains to determine the poles and the residues. We will first treat the nearest-neighbor tunneling approximation.

A.3.1 Nearest-neighbor approximation

In the nearest-neighbor approximation the energy dispersion takes the form $\epsilon_K(k) = E_K \cos(ka)$ with $E_K = 4J_1 \cos(\frac{1}{2}Ka)$. If we take the energy to be inside the continuum $|E| \leq |E_K|$, we find poles at quasi-momenta

$$k^{\pm} = \pm \frac{1}{a} \cos^{-1} \frac{E + i\eta}{E_K} \simeq \pm(k_0 + i\eta'), \quad (\text{A.26})$$

where $k_0a = \cos^{-1}(E/E_K)$ are always chosen to be positive and η' is an infinitesimal with same sign as η .¹ Therefore, k^+ (k^-) lies in the upper (lower) complex half plane for $\eta > 0$ and in the lower (upper) when η is negative. The poles are simple and applying l'Hospital's rule we determine the residues to

$$\text{Res}_{k^{\pm}} \frac{a}{2\pi} \frac{e^{ikz}}{E - \epsilon_K(k) + i\eta} = \mp \frac{1}{2\pi} \frac{e^{\pm ik_0z}}{|E_K| \sin(ak_0)}. \quad (\text{A.27})$$

Noting $|E_K| \sin(ak_0) = \sqrt{E_K^2 - E^2} \cos^2(ak_0)$ we arrive at the solutions for the integral Eq. (A.17):

$$G_K^0(E, z \geq 0) = 2\pi i \text{Res}_{k^+} f(k) = -i \frac{e^{ik_0z}}{\sqrt{E_K^2 - E^2}}, \quad (\text{A.28a})$$

$$G_K^0(E, z \leq 0) = -2\pi i \text{Res}_{k^-} f(k) = -i \frac{e^{-ik_0z}}{\sqrt{E_K^2 - E^2}}. \quad (\text{A.28b})$$

¹This is seen from a Taylor expansion around $k_0 \in [0, \pi/a]$ of the cosine:

$$\cos[(k_0 + i\eta')a] \simeq \cos(k_0a) - a \sin(k_0a) i\eta' = (E + i\eta'a \sin(k_0a))/E_K,$$

where $\sin(k_0a) > 0$ and $E_K < 0$.

The minus sign in (A.28b) appears because the integration direction has changed to clockwise, see Fig. A.1(b). The above equation can be stated more compact as

$$G_K^0(E, z) = -\frac{i \exp(ik_0|z|)}{\sqrt{E_K^2 - E^2}}. \quad (\text{A.29})$$

We note that if we had chosen $\eta < 0$, the imaginary part of the poles in Eq. (A.26) would change sign, which instead would provide us with the advanced Green's function

$$G_K^{0,A}(E, z) = \frac{i \exp(-ik_0|z|)}{\sqrt{E_K^2 - E^2}}. \quad (\text{A.30})$$

If applied in the Lippmann-Schwinger equation in Eq. (3.26), the advanced Green's function would result in an incoming, instead of outgoing, "scattered" wave,

$$\psi_K^{\text{bg}}(E, z) = e^{ik_0z} + f_{\text{bg}} e^{-ik_0|z|}, \quad (\text{A.31})$$

where f_{bg} is the scattering amplitude (see Eq. (3.30)).

If on the other hand $|E| > |E_K|$, *i.e.*, for energies outside the continuum band, the poles are purely complex: $\epsilon_K(\pm i\kappa_0) = E$ (here $\eta = 0$) with

$$\kappa_0 = \frac{1}{a} \cosh^{-1} \left| \frac{E}{E_K} \right|. \quad (\text{A.32})$$

Following the same procedure as inside the band we find

$$G_K^0(E, z) = \text{sgn}(E) \frac{\exp(-\kappa_0|z|)}{\sqrt{E^2 - E_K^2}} [-\text{sgn}(E)]^{z/a}. \quad (\text{A.33})$$

A.3.2 Next-nearest-neighbor tunneling

This subsection covers work in progress. There are many open questions and for the same reason many of the findings lack a proper discussion of the underlying physics.

It is more complicated to locate the poles, when tunneling between more than nearest-neighbors are included. We have to solve the equation

$$E + i\eta = -4 \sum_{d=1}^{\mathcal{D}} J_d \cos\left(\frac{1}{2}Kad\right) \cos(kad). \quad (\text{A.34})$$

Since the $\cos(kad)$ -factors can be written as d -degree polynomials in $y = \cos(ka)$,² equation (A.34) becomes a \mathcal{D} -degree polynomial in y . If $\mathcal{D} = 2$, we

²This follows from the recursive relation

$$\cos(kam + ka) = 2 \cos(ka) \cos(kam) - \cos(kam - ka), \quad m \in \mathbb{N}.$$

find

$$0 = -8J_2 \cos(Ka)y^2 - 4J_1 \cos(\frac{1}{2}Ka)y + 4J_2 \cos(Ka) - E - i\eta \quad (\text{A.35})$$

with solutions

$$y^\pm = \frac{4J_1 \cos(\frac{1}{2}Ka) \pm \sqrt{(4J_1 \cos(\frac{1}{2}Ka))^2 + 32J_2 \cos(Ka) (4J_2 \cos(Ka) - E - i\eta)}}{-16J_2 \cos(Ka)} \quad (\text{A.36})$$

from which we can determine the poles:

$$k_i = \pm k_0^\pm, \quad k_0^\pm = \frac{1}{a} \cos^{-1} y^\pm. \quad (\text{A.37})$$

This gives two pairs of poles, where each pair has one in the upper and one in the lower complex half plane. We denote the four poles by k_i , $i \in \{1, 2, 3, 4\}$. As our calculation in Fig. A.2 shows, the poles can be both purely real ($\eta \rightarrow 0$), purely imaginary and mixed real and imaginary. The values in the figure is for a lattice with strength $V_0 = 1$ similar to the lattice considered in the numerical examples of Chapter 6. Note that the denominator of Eq. (A.36) diverges at $K = \pi/2a$ because $J_2 \cos(Ka)$ goes to zero, fortunately this is also the case for the dispersion Eq. (A.18), which reduces to the energy dispersion known from the nearest-neighbor approximation. Therefore we can treat the integral (A.17) as if only nearest-neighbor tunneling were included, *i.e.*, the solutions are given by Eqs. (A.29) and (A.33).

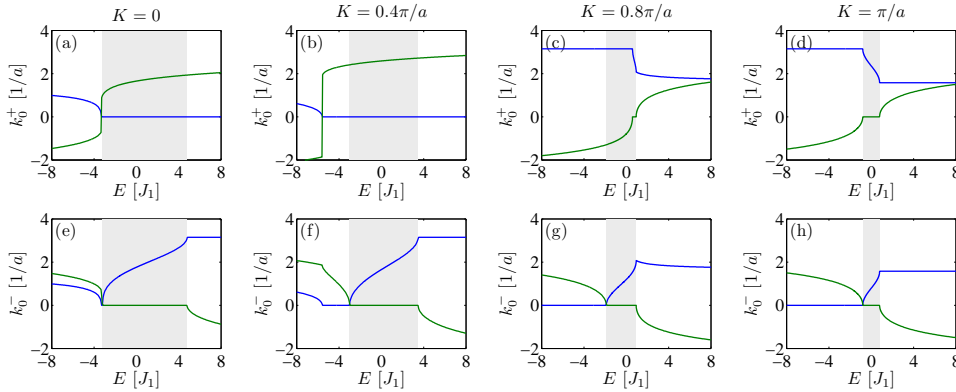


Figure A.2: Poles of the Green's function (A.17) for $\mathcal{D} = 2$ and $V_0 = 1$. The blue (green) curve shows the real (imaginary) part of k_0^\pm . The first and second row of figures shows k_0^+ and k_0^- , respectively, whereas the columns corresponds to $K = 0, 0.4, 0.8, 1 \pi/a$ from left to right. The energy range of the continuum states are indicated by the gray shading. The two poles $-k_0^+$ and $-k_0^-$ are not shown.

Assuming all poles are simple, the Green's function can be conveniently written

$$G_K^0(E, z \geq 0) = 2\pi i \sum_{\text{Im } k_i > 0} \text{Res}_{k_i} f(k) = i \sum_{\text{Im } k_i > 0} \frac{ae^{ik_i z}}{\epsilon'_K(k_i)} \quad (\text{A.38a})$$

for $z \geq 0$, whereas for $z \leq 0$ we have

$$G_K^0(E, z \leq 0) = -2\pi i \sum_{\text{Im } k_i > 0} \text{Res}_{-k_i} f(k) = i \sum_{\text{Im } k_i > 0} \frac{e^{-ik_i z}}{\epsilon'_K(k_i)}. \quad (\text{A.38b})$$

In (A.38b) we have used $\epsilon'_K(-x) = -\epsilon'_K(x)$ for any $x \in \mathbb{C}$, which is a property inherited from $\sin(x) = (e^{ix} - e^{-ix})/2i$. Furthermore, we have used that the poles come in pairs with opposite sign ($k_i = -k_j$ for some i and j), therefore a sum over $\text{Im } k_i < 0$ is identical to a sum over $\text{Im } k_i > 0$ with k_i replaced with $-k_i$.

As in the nearest-neighbor tunneling case we can collect Eqs. (A.38a) and (A.38b) to one equation:

$$G_K^0(E, z) = i \sum_{\text{Im } k_i > 0} \frac{ae^{ik_i|z|}}{\epsilon'_K(k_i)}, \quad (\text{A.39})$$

which is valid for all energies E .

We note that for energies inside the continuum range, a real pole causes a scattered wave in the Lippmann-Schwinger equation, while a complex pole gives a decaying contribution to the Green's function above. With this in mind we observe from Fig. A.2 that for E inside the continuum (indicated by the gray shading) there is always at least one real pole. Moreover, we observe that for K close to $\pm\pi/a$, a region exist, where both sets of poles become real. This can be understood from Fig. A.3 showing the dispersion $\epsilon_K(k)$. The energy range, which features two real poles, are marked by gray shading and we observe that this is exactly the range with four-fold degeneracy. In this energy interval two momenta of the scattered waves are possible in perfect agreement with a Green's function with two real poles.

For energies outside the continuum the poles are mixed real and imaginary numbers, this is puzzling because it may impose a z -dependent phase factor on the Green's function (A.39). However, it appears that the complex and the real parts are of equal absolute values. We recall that the bound state wave functions in the presence of a delta-function interaction is proportional to the Green's function (see Sec. 3.6). As pointed out earlier this is work in progress.

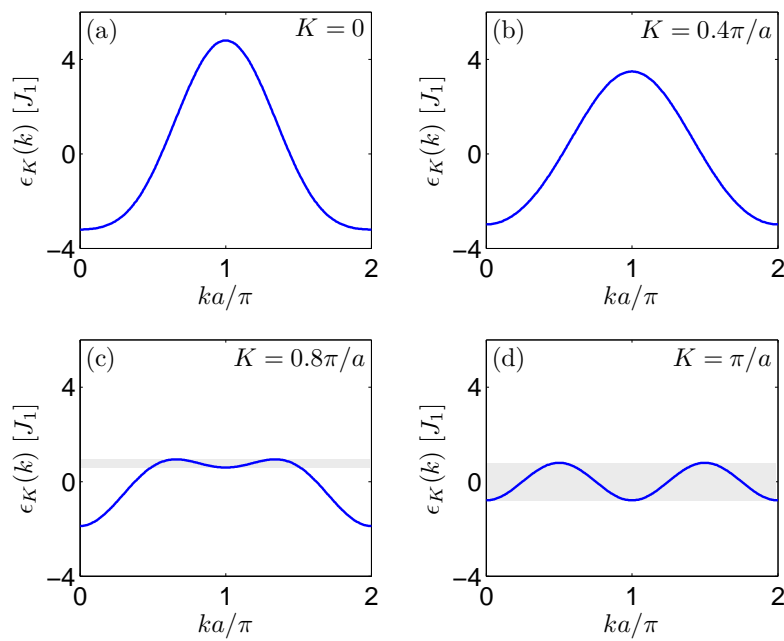


Figure A.3: Two-body band structure $\epsilon_K(k)$ for the values of K considered in Fig. A.2. The gray shading in (c)-(d) indicates the energy range in which the degeneracy of the scattered waves are doubled from two to four.

Appendix B

Stochastic Gutzwiller method

The Gutzwiller Approximation (GA), as introduced in Sec. 7.5, goes beyond common mean field in that it allows non-coherent states at each site in the lattice, even though the sites still only influence one another by the operator c-value $\langle \hat{a}_j \rangle$. This neglects all spatial correlations, because if we want the expectation value of, say, $\langle \hat{a}_1^\dagger \hat{a}_0 \rangle$, the Gutzwiller Ansatz will give back a product of the two sites treated individually, *i.e.*, $\langle \hat{a}_1^\dagger \hat{a}_0 \rangle = \langle \hat{a}_1^\dagger \rangle \langle \hat{a}_0 \rangle$.

In this appendix we present and improve a stochastic method that incorporates correlations into the GA. The method was first suggested by Carusotto and Castin in Ref. [121] and is an exact reformulation of the GA. We improve it to incorporate more than nearest-neighbor tunneling. Our original intent was to apply it on the four-wave mixing, discussed in Chap. 7, but this is not possible due to the involved time scales. The criteria for applying the model is considered in details at the end of this section.

First of all we will need some notation: To allow for more indices we will write $f(j, n)$ instead of f_n^j and all the undefined coefficients, *e.g.*, $f(j, -1)$, are set to zero. The state at lattice site j is written $|f(j)\rangle = \sum_n f(j, n) |n\rangle_j$. For simplicity we will define the non-local delta-function $\delta_{j,l}^{(d)} = \delta_{j,l+d} + \delta_{j,l-d}$. The inner product of two Gutzwiller states given by the functions f_a and f_b are in this new notation

$$\langle G : f_a | G : f_b \rangle = \prod_j \sum_n f_a(j, n)^* f_b(j, n) = \prod_j \langle f_a(j) | f_b(j) \rangle. \quad (\text{B.1})$$

We are not guaranteed that the norm is preserved in the stochastic model, and therefore all expectation values have to be normalized, *e.g.*, the order parameter ϕ_j is defined

$$\phi_j = \frac{\langle f(j) | \hat{a}_j | f(j) \rangle}{\langle f(j) | f(j) \rangle}. \quad (\text{B.2})$$

The tunneling part of the Bose-Hubbard Hamiltonian (7.22) can be written

as¹

$$\mathcal{H}_J = - \sum_{d,j,l} J_d \delta_{j,l}^{(d)} \{ (\hat{a}_j^\dagger - \phi_j^*) (\hat{a}_l - \phi_l) + \phi_l \hat{a}_j^\dagger + \phi_l^* \hat{a}_j - \phi_l^* \phi_j \}. \quad (\text{B.3})$$

In mean field theory the first term is assumed to be small and thus eliminated, but we will keep it in the following. The last term will only contribute as an overall phase factor $e^{i\chi(t)}$, where

$$\chi(t) = \int dt \sum_{d,j,l} J_d \delta^{(d)} \phi_j^* \phi_l, \quad (\text{B.4})$$

and hence can be ignored.

We want to determine the evolution in f . To do this we consider what happens to the state vector in an infinitesimal time step dt

$$d|G : f\rangle = -idt \mathcal{H} |G : f\rangle \quad (\text{B.5a})$$

$$= -idt \sum_{j,n} \left[U n (n-1) f(j, n) \right] \quad (\text{B.5b})$$

$$- \sqrt{n+1} f(j, n+1) \sum_{d,l} J_d \delta_{j,l}^{(d)} \phi_l^* \quad (\text{B.5c})$$

$$- \sqrt{n} f(j, n-1) \sum_{d,l} J_d \delta_{j,l}^{(d)} \phi_l \left] |n_j\rangle \prod_{\gamma \neq j} \sum_m f(\gamma, m) |m_\gamma\rangle \quad (\text{B.5d})$$

$$+ idt \sum_{\substack{j,l,d \\ n,m}} J_d \delta_{j,l}^{(d)} (\sqrt{n} f(j, n-1) - \phi_j^* f(j, n)) \quad (\text{B.5e})$$

$$\times (\sqrt{m+1} f(l, m+1) - \phi_l f(l, m)) |n\rangle_j |m\rangle_l \prod_{\gamma \neq j,l} \sum_l f(\gamma, l) |l\rangle_\gamma. \quad (\text{B.5f})$$

Line b-d are already accounted for in GA, but the last two lines are new. The trick is now to split the infinitesimal change in f into two parts $df(j, n) = df_d(j, n) + df_s(j, n)$, where df_d is a deterministic part of order dt and df_s is a stochastic white noise of order $dt^{1/2}$, *i.e.*, with mean $\overline{df_s} = 0$ and variance $\overline{df_s df_s} = dt$. Here we denote the average over different realizations by $\overline{}$. By collecting terms only to first order in dt and on the same time averaging over

¹In this and the following equations it is always a good idea to count the number of terms to make sure that each term is counted exactly once.

realizations, we obtain

$$\begin{aligned}
\overline{d|G : f\rangle} &= \overline{|G : f + df\rangle - |G : f\rangle} \\
&= \overline{\prod_j \sum_n (f(j, n) + df(j, n)) |n\rangle_j - |G : f\rangle} \\
&= \sum_{j, n} df_d(j, n) |n\rangle_j \prod_{l \neq j} \sum_m f(l, m) |m\rangle_l \\
&\quad + \sum_{\substack{j \neq l \\ n, m}} \overline{df_s(j, n) df_s(l, m)} |n\rangle_j |m\rangle_l \prod_{\gamma \neq j, l} \sum_l f(\gamma, l) |l\rangle_\gamma.
\end{aligned} \tag{B.6}$$

The average here is over the infinitesimal time step given a state f . Comparing Eqs. (B.5) and (B.6) we can identify the deterministic part of the differential

$$\begin{aligned}
df_d(j, n) &= -idt \left[(Un_j(n_j - 1) - \chi)f(j, n) \right. \\
&\quad \left. - \sqrt{n+1}f(j, n+1) \sum_{d, l} J_d \delta_{j, l}^{(d)} \phi_l^* \right. \\
&\quad \left. - \sqrt{n}f(j, n-1) \sum_{d, l} J_d \delta_{j, l}^{(d)} \phi_l \right],
\end{aligned} \tag{B.7}$$

which is the traditional Gutzwiller evolution, and the stochastic part

$$\begin{aligned}
\overline{df_s(j, n) df_s(l, m)} &= idt \sum_{d=1}^{\mathcal{D}} J_d \delta_{j, l}^{(d)} (\sqrt{n}f(j, n-1) - \phi_j^* f(j, n)) \\
&\quad \times (\sqrt{m+1}f(l, m+1) - \phi_l f(l, m)) \\
&= \frac{idt}{2} \sum_{d=1}^{\mathcal{D}} J_d \delta_{j, l}^{(d)} (\sqrt{n}f(j, n-1) - \phi_j^* f(j, n)) \times (\sqrt{m+1}f(l, m+1) - \phi_l f(l, m)) \\
&\quad + (\sqrt{n}f(l, n-1) - \phi_l^* f(l, n)) \times (\sqrt{m+1}f(j, m+1) - \phi_j f(j, m)).
\end{aligned} \tag{B.8}$$

To obtain the last equality we have used the property that the correlation matrix for any two stochastic variables is symmetric, $\overline{df_s(j, n) df_s(l, m)} = \overline{df_s(l, m) df_s(j, n)}$. It is important to note that $df_s(j, n) df_s(j, m)$ never appears in (B.6), and therefore can be chosen freely. However, it appears in the error term, so it has to be minimized.

In general the noise term can be generated by

$$\begin{aligned}
df_s(j, n) &= \sqrt{\frac{idt}{2}} \left((\sqrt{n}f(j, n-1) - \phi_j^* f(j, n)) dB_j \right. \\
&\quad \left. + (\sqrt{n+1}f(j, n+1) - \phi_j f(j, n)) dB_j^* \right),
\end{aligned} \tag{B.9}$$

where dB_j is a stochastic variable satisfying

$$\overline{dB_j^* dB_l} = \sum_{d=1}^{\mathcal{D}} J_d \delta_{j,l}^{(d)} \quad \text{for } j \neq l, \quad (\text{B.10})$$

$$\overline{dB_j} = \overline{dB_j dB_l} = 0. \quad (\text{B.11})$$

The new stochastic variable dB_j in turn can be generated by

$$dB_j = c_0 e^{i\theta_j} + c_1 e^{i\theta_{j+1}} + \dots + c_{\mathcal{D}} e^{i\theta_{j+\mathcal{D}}}, \quad (\text{B.12})$$

where $\theta_j \in [0, 2\pi]$ is a set of M uniformly distributed numbers (M is the number of lattice sites included in the calculation). For simplicity we will in the rest of this section assume that only tunneling to the nearest neighbors and next-nearest neighbors is important, *i.e.*, $\mathcal{D} = 2$. It is straightforward to show that the noise in Eq. (B.12) fulfils Eqs. (B.10) and (B.11) under the conditions:

$$J_1 = \overline{dB_j^* dB_{j+1}} = c_1^* c_0 + c_2^* c_1, \quad (\text{B.13})$$

$$J_2 = \overline{dB_j^* dB_{j+2}} = c_2^* c_1. \quad (\text{B.14})$$

The upper bound on the free term becomes

$$|dB_j^* dB_j| \leq (|c_0| + |c_1| + |c_2|)^2, \quad (\text{B.15})$$

so we have to minimize $|c_0| + |c_1| + |c_2|$. Since there are three variables and two constraints we end up with a one-variable equation to minimize: $\min_{c_0} \{|c_0| + |J_2/c_0| + |J_1/(c_0 + J_2/c_0)|\}$, where $c_1 = J_1/(c_0 + J_2/c_0)$ and $c_2 = J_2/c_0$. In the deep lattice limit where $J_2 \rightarrow 0$ we get the optimal solution $c_0 = \text{sgn}(J_1)c_1 = \sqrt{J_1}$ and $c_2 = 0$, which results in $|dB_j^* dB_j| \leq 4|J_1|$.

We will use the sampling variance as an estimate for the error

$$\begin{aligned} E(t) &= \overline{\| |G : f(t)\rangle - |\Psi(t)\rangle \|^2} \\ &= \overline{\langle G : f(t) | G : f(t) \rangle} - \langle \Psi(t) | \Psi(t) \rangle \\ &= \Delta(t) - 1. \end{aligned} \quad (\text{B.16})$$

The vector $|\Psi\rangle$ is the exact solution and accordingly it is normalized. So the variance only depends on the average of the norm $\Delta(t) = \overline{\langle G : f(t) | G : f(t) \rangle}$. This can be estimated by considering a differential increment

$$d\Delta = \langle G : f + df | G : f + df \rangle - \Delta(t). \quad (\text{B.17})$$

In Sec. B.1 we estimate an upper bound on this increment to be

$$d\Delta = \sum_j \langle df_s(j) | df_s(j) \rangle \leq M \mathcal{J} (6\mathcal{N}_{max} + 1) \Delta(t) dt, \quad (\text{B.18})$$

where $\mathcal{J} = \sup |dB_j|^2 = (|c_0| + |c_1| + |c_2|)^2$ and \mathcal{N}_{\max} is the maximal allowed number of atoms per site. With this upper bound we can now determine an upper bound on $\Delta(t)$ to be

$$\Delta(t) \leq \Delta(0)e^{\mathcal{J}M(6\mathcal{N}_{\max}+1)t} \quad (\text{B.19})$$

and hence

$$E(t) \leq (E(0) + 1)e^{\mathcal{J}M(6\mathcal{N}_{\max}+1)t} - 1. \quad (\text{B.20})$$

The higher the error is, the more simulations are needed for the final state to converge. We have shown that the error is bounded, but the bound is growing exponentially on a time scale defined by $t_{\text{err}} = 1/\mathcal{J}M(6\mathcal{N}_{\max} + 1)$. Thus only for processes that takes place on this time scale or faster can be efficiently simulated. To estimate the time scale for the Gutzwiller simulation of four-wave-mixing provided in Sec. 7.7, we assume for simplicity only nearest-neighbor tunneling, which allow us to write $\mathcal{J} \sim 4|J_1| \sim E_R$, and we get $t_{\text{eff}} = 2 \times 10^{-4} \hbar/E_R$. This is an extremely short scale compared to the mixing process shown in Fig. 7.8 and 7.9, where the relevant time scale is tens of \hbar/E_R .

So far in the literature this method has only been used to obtain ground states by steepest descent (propagation in imaginary time) [121, 122]. In Ref. [122] they have no lattice, and the tunneling coefficients comes from the numerical discretized kinetic energy operator

$$\hat{\mathcal{K}} = -\frac{\hbar^2}{2m}\nabla_x^2 \rightarrow -\frac{\hbar^2}{2m\Delta x^2}\Delta_{x_i} + \mathcal{O}(\Delta x^4), \quad (\text{B.21})$$

where x is the continuous position coordinate and x_i the discretized coordinate with the discrete Laplacian $\Delta_{x_i} f(x_i) = f(x_i + \Delta x) + f(x_i - \Delta x) - 2f(x_i)$, cf. Sec. 3.2. The tunneling amplitudes are readily determined to $J_1 = \hbar^2/2m\Delta x^2$ and $J_d = 0$ for all $d \geq 2$.

If applied for longer time scales, the issue of convergence needs to be addressed, since stochastic time propagation converges slower due to the $dt^{1/2}$ -scaling. This is comprehensively discussed in Ref. [123].

B.1 Error estimation in the Stochastic Gutzwiller Method

You can consider this an appendix to the appendix. We will in this section derive an upper bound on the infinitesimal increment of the error $\Delta(t)$,

$$d\Delta = \langle G : f + df | G : f + df \rangle - \Delta(t), \quad (\text{B.22})$$

used in Eq. (B.18). The derivation is rather technical and long.

Recall that

$$|G : f + df\rangle = \prod_j (|f(j)\rangle + |df_d(j)\rangle + |df_s(j)\rangle). \quad (\text{B.23})$$

We will benefit from the fact that both the deterministic, df_d , and the stochastic increment df_s are orthogonal to the state vector, the later can be seen by

$$\begin{aligned}
& \sum_n f(j, n)^* df_s(j, n) = \\
& \sqrt{idt} dB_j \left(\sum_n \sqrt{n} f(j, n)^* f(j, n-1) - \phi_j^* \sum_n f(j, n)^* f(j, n) \right) \\
& + \sqrt{idt} dB_j^* \left(\sum_n \sqrt{n+1} f(j, n)^* f(j, n+1) - \phi_j \sum_n f(j, n)^* f(j, n) \right) \\
& = \sqrt{idt} (dB_j(\phi_j^* - \phi_j) + dB_j^*(\phi_j - \phi_j)) \langle f(j) | f(j) \rangle = 0.
\end{aligned} \tag{B.24}$$

Here we have used $\phi_j = \langle f(j) | f(j) \rangle = \sum_n \sqrt{n+1} f(j, n)^* f(j, n+1)$. This only works because ϕ_j is normed otherwise we will be left with a term proportional to $(1 - \langle f(j) | f(j) \rangle)$. Furthermore, an expression for the norm of df_s is necessary

Furthermore $\langle df_s(j) | df_d(j) \rangle$ has order $dt^{3/2}$ and can be neglected. This leaves us only the following term to consider

$$\begin{aligned}
& \langle df_s(j) | df_s(j) \rangle = \sum_n df_s(j, n)^* df_s(j, n) = \\
& \sum_n \left((|\sqrt{n} f(j, n-1) - \phi_j^* f(j, n)|^2 + |\sqrt{n+1} f(j, n+1) - \phi_j f(j, n)|^2) dB_j^* dB_j + \right. \\
& \left. 2\text{Re} [(\sqrt{n} f(j, n-1) - \phi_j^* f(j, n))(\sqrt{n+1} f(j, n+1)^* - \phi_j^* f(j, n)^*) dB_j dB_j] \right) dt.
\end{aligned} \tag{B.25}$$

In what follows we will use the definition $\mathcal{J} = \sup |dB_j|^2$. We now estimate the terms in Eq. (B.25) one by one:

$$\begin{aligned}
& \sum_n |\sqrt{n} f(j, n-1) - \phi_j^* f(j, n)|^2 = \\
& \sum_n \left(n |f(j, n-1)|^2 - \phi_j^* \sqrt{n} f(j, n-1)^* f(j, n) \right. \\
& \left. - \phi_j \sqrt{n} f(j, n-1) f(j, n)^* + |\phi_j f(j, n)|^2 \right) = \\
& \langle f(j) | \hat{n} | f(j) \rangle + (1 - |\phi_j|^2) \langle f(j) | f(j) \rangle \leq (\mathcal{N}_{max} + 1) \langle f(j) | f(j) \rangle,
\end{aligned} \tag{B.26a}$$

$$\begin{aligned}
& \sum_n |\sqrt{n+1} f(j, n+1) - \phi_j f(j, n)|^2 = \\
& \langle f(j) | \hat{n} | f(j) \rangle - |\phi_j|^2 \langle f(j) | f(j) \rangle \leq \mathcal{N}_{max} \langle f(j) | f(j) \rangle \tag{B.26b}
\end{aligned}$$

and the cross term is

$$\begin{aligned}
 & 2\text{Re} \left[\sum_n (\sqrt{n}f(j, n-1) - \phi_j^* f(j, n)) (\sqrt{n+1}f(j, n+1)^* - \phi_j^* f(j, n)^*) dB_j dB_j \right] \\
 &= 2\text{Re} \left[\langle f(j) | \hat{a}^\dagger \hat{a}^\dagger | f(j) \rangle - \phi_j^{*2} \langle f(j) | f(j) \rangle dB_j dB_j \right] \\
 &\leq 2 \left| \langle f(j) | \hat{a} \hat{a} | f(j) \rangle - \phi_j^2 \langle f(j) | f(j) \rangle \right| |dB|^2 \\
 &\leq 2\mathcal{J}(\sqrt{\mathcal{N}_{max}(\mathcal{N}_{max}-1)} + \mathcal{N}_{max}) \langle f(j) | f(j) \rangle \\
 &\leq 4\mathcal{J}\mathcal{N}_{max} \langle f(j) | f(j) \rangle.
 \end{aligned} \tag{B.26c}$$

Hence we obtain

$$\langle df_s(j) | df_s(j) \rangle \leq \mathcal{J} (6\mathcal{N}_{max} + 1) \langle f(j) | f(j) \rangle dt. \tag{B.27}$$

From which we now can estimate the differential increment (B.22) to

$$d\Delta = \sum_j \langle df_s(j) | df_s(j) \rangle = \Delta(t) \sum_j \frac{\langle df_s(j) | df_s(j) \rangle}{\langle f(j) | f(j) \rangle} \leq M\mathcal{J} (6\mathcal{N}_{max} + 1) \Delta(t) dt, \tag{B.28}$$

where M is the number of lattice periods and \mathcal{N}_{max} is the number of Fock states included in the calculation.

An examination of Eqs. (B.26) shows that for a perfect coherent state

$$\langle df_s(j) | df_s(j) \rangle_{\text{Coherent}} = \mathcal{J} \langle f(j) | f(j) \rangle dt, \tag{B.29}$$

which gives the increments

$$d\Delta_{\text{Coherent}} = M\mathcal{J}\Delta(t)dt. \tag{B.30}$$

This indicate that the error and hence the number of needed realizations might be smaller for a coherent state. However a coherent state will quickly be lost in a trajectory, *i.e.*, a single simulation, due to the stochastic noise.

Bibliography

- [1] R. Piil and K. Mølmer, *Tunneling couplings in discrete lattices, single-particle band structure, and eigenstates of interacting atom pairs*, Phys. Rev. A **76**, 023607 (2007).
- [2] N. Nygaard, R. Piil and K. Mølmer, *Feshbach molecules in a one-dimensional optical lattice*, Phys. Rev. A **77**, 021601(R) (2008).
- [3] N. Nygaard, R. Piil and K. Mølmer, *Two-channel Feshbach physics in a structured continuum*, Phys. Rev. A **78**, 023617 (2008).
- [4] R. T. Piil, N. Nygaard and K. Mølmer, *Scattering and binding of different atomic species in a one-dimensional optical lattice*, Phys. Rev. A **78**, 033611 (2008).
- [5] P. B. Blakie and C. W. Clark, *Wannier states and Bose-Hubbard parameters for 2D optical lattices*, J. Phys. B: At. Mol. Opt. Phys. **37**, 1391 (2004).
- [6] K. I. Petsas, A. B. Coates and G. Grynberg, *Crystallography of optical lattices*, Phys. Rev. A **50**, 5173 (1994).
- [7] L. Santos, M. A. Baranov, J. I. Cirac, H.-U. Everts, H. Fehrmann and M. Lewenstein, *Atomic Quantum Gases in Kagomé Lattices*, Phys. Rev. Lett. **93**, 030601 (2004).
- [8] G. Grynberg, *Cold atoms in dissipative optical lattices*, Phys. Rep. **355**, 335 (2001).
- [9] B. Paredes, A. Widera, V. Murg, O. Mandel, S. Fölling, I. Cirac, G. V. Shlyapnikov, T. W. Hansch and I. Bloch, *Tonks-Girardeau gas of ultracold atoms in an optical lattice*, Nature **429**, 277 (2004).
- [10] T. Kinoshita, T. Wenger and D. Weiss, *Observation of a one-dimensional Tonks-Girardeau gas.*, Science **305**, 1125 (2004).
- [11] M. Budde and K. Mølmer, *Number distributions for fermions and fermionized bosons in periodic potentials*, Phys. Rev. A **70**, 053618 (2004).

-
- [12] M. Greiner, I. Bloch, O. Mandel, T. W. Hänsch and T. Esslinger, *Exploring Phase Coherence in a 2D Lattice of Bose-Einstein Condensates*, Phys. Rev. Lett. **87**, 160405 (2001).
- [13] A. Görlitz, J. M. Vogels, A. E. Leanhardt, C. Raman, T. L. Gustavson, J. R. Abo-Shaeer, A. P. Chikkatur, S. Gupta, S. Inouye, T. Rosenband and W. Ketterle, *Realization of Bose-Einstein Condensates in Lower Dimensions*, Phys. Rev. Lett. **87**, 130402 (2001).
- [14] M. Greiner, O. Mandel, T. W. Hänsch and I. Bloch, *Collapse and Revival of the Matter Wave Field of a Bose-Einstein Condensate*, Nature **419**, 51 (2002).
- [15] A. Sørensen and K. Mølmer, *Spin-Spin Interaction and Spin Squeezing in an Optical Lattice*, Phys. Rev. Lett. **83**, 2274 (1999).
- [16] O. Mandel, M. Greiner, A. Widera, T. Rom, T. W. Hänsch and I. Bloch, *Controlled collisions for multi-particle entanglement of optically trapped atoms*, Nature **425**, 937 (2003).
- [17] K. Winkler, G. Thalhammer, F. Lang, R. Grimm, J. Hecker Denschlag, A. J. Daley, A. Kantian, H. P. Büchler and P. Zoller, *Repulsively bound atom pairs in an optical lattice*, Nature **441**, 853 (2006).
- [18] J. Hecker Denschlag and A. J. Daley, *Exotic atom pairs: Repulsively bound states in an optical lattice*, *Proceedings of the international school of physics "Enrico Fermi", Course CLXIV, Ultra-Cold Fermi Gases* (2006), e-print arXiv:cond-mat/0610393v1.
- [19] S. Fölling, S. Trotzky, P. Cheinet, M. Feld, R. Saers, A. Widera, T. Müller and I. Bloch, *Direct observation of second-order atom tunnelling*, Nature **448**, 1029 (2007).
- [20] H. Moritz, T. Stöferle, K. Günter, M. Köhl and T. Esslinger, *Confinement Induced Molecules in a 1D Fermi Gas*, Phys. Rev. Lett. **94**, 210401 (2005).
- [21] M. H. Anderson, J. R. Ensher, M. R. Matthews, C. E. Wieman and E. A. Cornell, *Observation of Bose-Einstein Condensation in a Dilute Atomic Vapor*, Science **269**, 198 (1995).
- [22] K. B. Davis, M. O. Mewes, M. R. Andrews, N. J. van Druten, D. S. Durfee, D. M. Kurn and W. Ketterle, *Bose-Einstein Condensation in a Gas of Sodium Atoms*, Phys. Rev. Lett. **75**, 3969 (1995).
- [23] J. M. Vogels, K. Xu and W. Ketterle, *Generation of Macroscopic Pair-Correlated Atomic Beams by Four-Wave Mixing in Bose-Einstein Condensates*, Phys. Rev. Lett. **89**, 020401 (2002).

- [24] K. M. Hilligsøe and K. Mølmer, *Phase-matched four wave mixing and quantum beam splitting of matter waves in a periodic potential*, Phys. Rev. A **71**, 041602 (2005).
- [25] G. K. Campbell, J. Mun, M. Boyd, E. W. Streed, W. Ketterle and D. E. Pritchard, *Parametric Amplification of Scattered Atom Pairs*, Phys. Rev. Lett. **96**, 020406 (2006).
- [26] N. Gemelke, E. Sarajlic, Y. Bidel, S. Hong and S. Chu, *Parametric Amplification of Matter Waves in Periodically Translated Optical Lattices*, Phys. Rev. Lett. **95**, 170404 (2005).
- [27] K. Mølmer, *Phase-matched matter wave collisions in periodic potentials*, New J. Phys. **8**, 170 (2006).
- [28] M. Greiner, O. Mandel, T. Esslinger, T. W. Hänsch and I. Bloch, *Quantum phase transition from a superfluid to a Mott insulator in a gas of ultracold atoms*, Nature **415**, 39 (2002).
- [29] T. Stöferle, H. Moritz, C. Schori, M. Köhl and T. Esslinger, *Transition from a Strongly Interacting 1D Superfluid to a Mott Insulator*, Phys. Rev. Lett. **92**, 130403 (2004).
- [30] D. Jaksch, C. Bruder, J. I. Cirac, C. W. Gardiner and P. Zoller, *Cold Bosonic Atoms in Optical Lattices*, Phys. Rev. Lett. **81**, 3108 (1998).
- [31] M. P. A. Fisher, P. B. Weichman, G. Grinstein and D. S. Fisher, *Boson localization and the superfluid-insulator transition*, Phys. Rev. B **40**, 546 (1989).
- [32] P. A. F. da Veiga, L. Ioriatti and M. O'Carroll, *Energy-momentum spectrum of some two-particle lattice Schrödinger Hamiltonians*, Phys. Rev. E **66**, 016130 (2002).
- [33] I. Bloch, *Ultracold quantum gases in optical lattices*, Nat. Phys. **1**, 23 (2005).
- [34] I. Bloch, J. Dalibard and W. Zwerger, *Many-body physics with ultracold gases*, Rev. Mod. Phys. **80**, 885 (2008).
- [35] M. Haas, U. D. Jentschura and C. H. Keitel, *Comparison of classical and second quantized description of the dynamic Stark shift*, Am. J. Phys. **74**, 77 (2006).
- [36] S. Peil, J. V. Porto, B. L. Tolra, J. M. Obrecht, B. E. King, M. Subbotin, S. L. Rolston and W. D. Phillips, *Patterned loading of a Bose-Einstein condensate into an optical lattice*, Phys. Rev. A **67**, 051603 (2003).
- [37] F. Deuretzbacher, K. Plassmeier, D. Pfannkuche, F. Werner, C. Ospelkaus, S. Ospelkaus, K. Sengstock and K. Bongs, *Heteronuclear molecules in an optical lattice: Theory and experiment*, Phys. Rev. A **77**, 032726 (2008).

-
- [38] M. Olshanii, *Atomic Scattering in the Presence of an External Confinement and a Gas of Impenetrable Bosons*, Phys. Rev. Lett. **81**, 938 (1998).
- [39] T. Bergeman, M. G. Moore and M. Olshanii, *Atom-Atom Scattering under Cylindrical Harmonic Confinement: Numerical and Analytic Studies of the Confinement Induced Resonance*, Phys. Rev. Lett. **91**, 163201 (2003).
- [40] V. Peano, M. Thorwart, C. Mora and R. Egger, *Confinement-induced resonances for a two-component ultracold atom gas in arbitrary quasi-one-dimensional traps*, New J. Phys. **7**, 192 (2005).
- [41] J. I. Kim, J. Schmiedmayer and P. Schmelcher, *Quantum scattering in quasi-one-dimensional cylindrical confinement*, Phys. Rev. A **72**, 042711 (2005).
- [42] V. A. Yurovsky, *Feshbach resonance scattering under cylindrical harmonic confinement*, Phys. Rev. A **71**, 012709 (2005).
- [43] V. A. Yurovsky, *Properties of quasi-one-dimensional molecules with Feshbach-resonance interaction*, Phys. Rev. A **73**, 052709 (2006).
- [44] N. Ashcroft and N. Mermin, *Solid State Physics* (Thomson Learning, Inc., 1976).
- [45] C. Kittel, *Introduction to Solid State Physics* (John Wiley & Sons, Inc., 1996), 7th edition.
- [46] W. Kohn, *Analytic Properties of Bloch Waves and Wannier Functions*, Phys. Rev. **115**, 809 (1959).
- [47] L. He and D. Vanderbilt, *Exponential Decay Properties of Wannier Functions and Related Quantities*, Phys. Rev. Lett. **86**, 5341 (2001).
- [48] D. Jaksch and P. Zoller, *The cold atom Hubbard toolbox*, Ann. Phys. **315**, 52 (2005).
- [49] G. Thalhammer, K. Winkler, F. Lang, S. Schmid, R. Grimm and J. H. Denschlag, *Long-Lived Feshbach Molecules in a Three-Dimensional Optical Lattice*, Phys. Rev. Lett. **96**, 050402 (2006).
- [50] N. Strohmaier, Y. Takasu, K. Gunter, R. Jordens, M. Kohl, H. Moritz and T. Esslinger, *Interaction-Controlled Transport of an Ultracold Fermi Gas*, Phys. Rev. Lett. **99**, 220601 (2007).
- [51] S. M. Mahajan and A. Thyagaraja, *Exact two-body bound states with Coulomb repulsion in a periodic potential*, J. Phys. A: Math. Gen. **39**, L667 (2006).

-
- [52] J.-P. Martikainen, *Cooper problem in a lattice*, Phys. Rev. A **78**, 035602 (2008).
- [53] W. P. Su, J. R. Schrieffer and A. J. Heeger, *Solitons in Polyacetylene*, Phys. Rev. Lett. **42**, 1698 (1979).
- [54] C. Thelander, P. Agarwal, S. Brongersma, J. Eymery, L. Feiner, A. Forchel, M. Scheffler, W. Riess, B. Ohlsson, U. Gsele and L. Samuelson, *Nanowire-based one-dimensional electronics*, Mater. Today **9**, 28 (2006).
- [55] M. Block and M. Holthaus, *Pseudopotential approximation in a harmonic trap*, Phys. Rev. A **65**, 052102 (2002).
- [56] J. R. Taylor, *Scattering Theory: The Quantum Theory on Nonrelativistic Scattering* (John Wiley & Sons, Inc., 1972).
- [57] D. J. Griffiths, *Introduction to Quantum Mechanics* (Prentice Hall, 1995).
- [58] J. H. Eberly, *Quantum Scattering Theory in One Dimension*, Am. J. Phys. **33**, 771 (1965).
- [59] G. Barton, *Levinson's theorem in one dimension: heuristics*, J. Phys. A **18**, 479 (1985).
- [60] H. Friedrich, *Theoretical Atomic Physics* (Springer, 1998).
- [61] R. Micnas, J. Ranninger and S. Robaszkiewicz, *Superconductivity in narrow-band systems with local nonretarded attractive interactions*, Rev. Mod. Phys. **62**, 113 (1990).
- [62] A. B. Kuklov and B. V. Svistunov, *Counterflow Superfluidity of Two-Species Ultracold Atoms in a Commensurate Optical Lattice*, Phys. Rev. Lett. **90**, 100401 (2003).
- [63] L.-M. Duan, E. Demler and M. D. Lukin, *Controlling Spin Exchange Interactions of Ultracold Atoms in Optical Lattices*, Phys. Rev. Lett. **91**, 090402 (2003).
- [64] D. Petrosyan, B. Schmidt, J. R. Anglin and M. Fleischhauer, *Quantum liquid of repulsively bound pairs of particles in a lattice*, Phys. Rev. A **76**, 033606 (2007).
- [65] T. Miyakawa and P. Meystre, *Dissociation Dynamics of Ultracold Atom-Molecule Mixtures in an Optical Lattice*, J. Low Temp. Phys. **148**, 429 (2007).
- [66] M. B. Dahan, E. Peik, J. Reichel, Y. Castin and C. Salomon, *Bloch oscillations of atoms in an optical potential*, Phys. Rev. Lett. **76**, 4508 (1996).

- [67] J. P. Nguenang, R. A. Pinto and S. Flach, *Quantum q -breathers in a finite Bose-Hubbard chain: The case of two interacting bosons*, Phys. Rev. B **75**, 214303 (2007).
- [68] M. Valiente and D. Petrosyan, *Two-particle states in the Hubbard model*, J. Phys. B **41**, 161002 (2008).
- [69] C. Pethick and H. Smith, *Bose-Einstein Condensation in Dilute Gases* (Cambridge University Press, 2002).
- [70] T. Köhler, K. Góral and P. S. Julienne, *Production of cold molecules via magnetically tunable Feshbach resonances*, Rev. Mod. Phys. **78**, 1311 (2006).
- [71] N. Nygaard, B. I. Schneider and P. S. Julienne, *Two-channel R -matrix analysis of magnetic-field-induced Feshbach resonances*, Phys. Rev. A **73**, 042705 (2006).
- [72] Dürr, Stephan, Volz, Thomas, Rempe and Gerhard, *Dissociation of ultracold molecules with Feshbach resonances*, Phys. Rev. A **70**, 031601 (2004).
- [73] C. Chin, V. Vuletić, A. J. Kerman and S. Chu, *High Resolution Feshbach Spectroscopy of Cesium*, Phys. Rev. Lett. **85**, 2717 (2000).
- [74] P. J. Leo, C. J. Williams and P. S. Julienne, *Collision Properties of Ultracold ^{133}Cs Atoms*, Phys. Rev. Lett. **85**, 2721 (2000).
- [75] M. Greiner, C. Regal and D. Jin, *Emergence of a molecular Bose-Einstein condensate from a Fermi gas*, Nature **426**, 537 (2003).
- [76] S. Jochim, M. Bartenstein, A. Altmeyer, G. Hendl, S. Riedl, C. Chin, J. Hecker Denschlag and R. Grimm, *Bose-Einstein Condensation of Molecules*, Science **302**, 2101 (2003).
- [77] M. W. Zwierlein, C. A. Stan, C. H. Schunck, S. M. F. Raupach, S. Gupta, Z. Hadzibabic and W. Ketterle, *Observation of Bose-Einstein Condensation of Molecules*, Phys. Rev. Lett. **91**, 250401 (2003).
- [78] T. Bourdel, L. Khaykovich, J. Cubizolles, J. Zhang, F. Chevy, M. Teichmann, L. Tarruell, S. J. J. M. F. Kokkelmans and C. Salomon, *Experimental Study of the BEC-BCS Crossover Region in Lithium 6*, Phys. Rev. Lett. **93**, 050401 (2004).
- [79] J. Kinnunen, M. Rodríguez and P. Törmä, *Signatures of Superfluidity for Feshbach-Resonant Fermi Gases*, Phys. Rev. Lett. **92**, 230403 (2004).
- [80] E. A. Donley, N. R. Claussen, S. T. Thompson and C. E. Wieman, *Atom-molecule coherence in a Bose-Einstein condensate*, Nature **417**, 529 (2002).

- [81] K. Góral, T. Köhler, S. A. Gardiner, E. Tiesinga and P. S. Julienne, *Adiabatic association of ultracold molecules via magnetic-field tunable interactions*, J. Phys. B **37**, 3457 (2004).
- [82] N. Syassen, D. M. Bauer, M. Lettner, D. Dietze, T. Volz, S. Durr and G. Rempe, *Atom-Molecule Rabi Oscillations in a Mott Insulator*, Phys. Rev. Lett. **99**, 033201 (2007).
- [83] U. Fano, *Effects of Configuration Interaction on Intensities and Phase Shifts*, Phys. Rev. **124**, 1866 (1961).
- [84] J. U. Nöckel and A. D. Stone, *Resonance line shapes in quasi-one-dimensional scattering*, Phys. Rev. B **50**, 17415 (1994).
- [85] A. J. Moerdijk, B. J. Verhaar and A. Axelsson, *Resonances in ultracold collisions of ^6Li , ^7Li , and ^{23}Na* , Phys. Rev. A **51**, 4852 (1995).
- [86] G. Orso, L. P. Pitaevskii, S. Stringari and M. Wouters, *Formation of Molecules near a Feshbach Resonance in a 1D Optical Lattice*, Phys. Rev. Lett. **95**, 060402 (2005).
- [87] C. Zener, *Non-Adiabatic Crossing of Energy Levels*, Proc. Roy. Soc. London, Ser. A **137**, 696 (1932).
- [88] T. Mukaiyama, J. R. Abo-Shaeer, K. Xu, J. K. Chin and W. Ketterle, *Dissociation and Decay of Ultracold Sodium Molecules*, Phys. Rev. Lett. **92**, 180402 (2004).
- [89] M. Grupp, R. Walser, W. P. Schleich, A. Muramatsu and M. Weitz, *Resonant Feshbach scattering of fermions in one-dimensional optical lattices*, J. Phys. B **40**, 2703 (2007).
- [90] M. Köhl, H. Moritz, T. Stöferle, K. Günter and T. Esslinger, *Fermionic Atoms in a Three Dimensional Optical Lattice: Observing Fermi Surfaces, Dynamics, and Interactions*, Phys. Rev. Lett. **94**, 080403 (2005).
- [91] D. B. M. Dickerscheid, U. A. Khawaja, D. van Oosten and H. T. C. Stoof, *Feshbach resonances in an optical lattice*, Phys. Rev. A **71**, 043604 (2005).
- [92] K. B. Gubbels, D. B. M. Dickerscheid and H. T. C. Stoof, *Dressed molecules in an optical lattice*, New J. Phys. **8**, 151 (2006).
- [93] R. B. Diener and T.-L. Ho, *Fermions in Optical Lattices Swept across Feshbach Resonances*, Phys. Rev. Lett. **96**, 010402 (2006).
- [94] L.-M. Duan, *Effective Hamiltonian for Fermions in an Optical Lattice across a Feshbach Resonance*, Phys. Rev. Lett. **95**, 243202 (2005).
- [95] S. A. Gurvitz and Y. B. Levinson, *Resonant reflection and transmission in a conducting channel with a single impurity*, Phys. Rev. B **47**, 10578 (1993).

- [96] C. A. Stan, M. W. Zwierlein, C. H. Schunck, S. M. F. Raupach and W. Ketterle, *Observation of Feshbach Resonances between Two Different Atomic Species*, Phys. Rev. Lett. **93**, 143001 (2004).
- [97] E. Wille, F. M. Spiegelhalder, G. Kerner, D. Naik, A. Trenkwalder, G. Hendl, F. Schreck, R. Grimm, T. G. Tiecke, J. T. M. Walraven, S. J. J. M. F. Kokkelmans, E. Tiesinga and P. S. Julienne, *Exploring an Ultracold Fermi-Fermi Mixture: Interspecies Feshbach Resonances and Scattering Properties of ^6Li and ^{40}K* , Phys. Rev. Lett. **100**, 053201 (2008).
- [98] B. Deh, C. Marzok, C. Zimmermann and P. Courteille, *Feshbach resonances in mixtures of ultracold ^6Li and ^{87}Rb gases*, Phys. Rev. A **77**, 10701 (2008).
- [99] Z. Li, S. Singh, T. V. Tscherbul and K. W. Madison, *Feshbach resonances in ultracold ^{85}Rb - ^{87}Rb and ^6Li - ^{87}Rb mixtures*, Phys. Rev. A **78**, 022710 (2008).
- [100] S. Inouye, J. Goldwin, M. L. Olsen, C. Ticknor, J. L. Bohn and D. S. Jin, *Observation of Heteronuclear Feshbach Resonances in a Mixture of Bosons and Fermions*, Phys. Rev. Lett. **93**, 183201 (2004).
- [101] C. Ospelkaus, S. Ospelkaus, L. Humbert, P. Ernst, K. Sengstock and K. Bongs, *Ultracold Heteronuclear Molecules in a 3D Optical Lattice*, Phys. Rev. Lett. **97**, 120402 (2006).
- [102] S. B. Papp and C. E. Wieman, *Observation of Heteronuclear Feshbach Molecules from a ^{85}Rb - ^{87}Rb Gas*, Phys. Rev. Lett. **97**, 180404 (2006).
- [103] N. Nemitz, F. Baumer, F. Münchow, S. Tassy and A. Görlitz, *Production of ultracold heteronuclear YbRb^* molecules by photoassociation* (2008), arXiv:0807.0852.
- [104] D. DeMille, *Quantum Computation with Trapped Polar Molecules*, Phys. Rev. Lett. **88**, 067901 (2002).
- [105] G. Mazzarella, S. M. Giampaolo and F. Illuminati, *Extended Bose Hubbard model of interacting bosonic atoms in optical lattices: From superfluidity to density waves*, Phys. Rev. A **73**, 013625 (2006).
- [106] H. Heiselberg, *Extended Bose-Hubbard model with incompressible states at fractional numbers*, Phys. Rev. A **73**, 013628 (2006).
- [107] W. A. Schwalm and M. K. Schwalm, *Extension theory for lattice Green functions*, Phys. Rev. B **37**, 9524 (1988).
- [108] N. Katz, E. Rowen, R. Ozeri and N. Davidson, *Collisional Decay of a Strongly Driven Bose-Einstein Condensate*, Phys. Rev. Lett. **95**, 220403 (2005).

- [109] M. K. Olsen and M. J. Davis, *Entanglement properties of degenerate four-wave mixing of matter waves in a periodic potential*, Phys. Rev. A **73**, 063618 (2006).
- [110] M. A. Kasevich, *Coherence with Atoms*, Science **298**, 1363 (2002).
- [111] T. Esslinger and K. Mølmer, *Atoms and Molecules in Lattices: Bose-Einstein Condensates Built on a Shared Vacuum*, Phys. Rev. Lett. **90**, 160406 (2003).
- [112] K. Mølmer, *Phase collapse and excitations in Bose-Einstein condensates*, Phys. Rev. A **58**, 566 (1998).
- [113] D. van Oosten, P. van der Straten and H. T. C. Stoof, *Quantum phases in an optical lattice*, Phys. Rev. A **63**, 053601 (2001).
- [114] A. J. Daley, C. Kollath, U. Schollwöck and G. Vidal, *Time-dependent density-matrix renormalization-group using adaptive effective Hilbert spaces*, J. Stat. Mech.: Theory Exp. P04005 (2004).
- [115] J. Zakrzewski, *Mean-field dynamics of the superfluid-insulator phase transition in a gas of ultracold atoms*, Phys. Rev. A **71**, 043601 (2005).
- [116] A. A. Norrie, R. J. Ballagh and C. W. Gardiner, *Quantum turbulence and correlations in Bose-Einstein condensate collisions*, Phys. Rev. A **73**, 043617 (2006).
- [117] A. J. Ferris, M. J. Davis, R. W. Geursen, P. B. Blakie and A. C. Wilson, *Dynamical instabilities of Bose-Einstein condensates at the band edge in one-dimensional optical lattices*, Phys. Rev. A **77**, 012712 (2008).
- [118] A. Sinatra, C. Lobo and Y. Castin, *The truncated Wigner method for Bose-condensed gases: limits of validity and applications*, J. Phys. B **35**, 3599 (2002).
- [119] A. A. Norrie, R. J. Ballagh and C. W. Gardiner, *Quantum Turbulence in Condensate Collisions: An Application of the Classical Field Method*, Phys. Rev. Lett. **94**, 040401 (2005).
- [120] I. Stewart and D. Tall, *Complex Analysis* (Cambridge University Press, 1983).
- [121] I. Carusotto and Y. Castin, *An exact reformulation of the Bose-Hubbard model in terms of a stochastic Gutzwiller ansatz*, New J. Phys. **5**, 91 (2003).
- [122] B. Schmidt, L. I. Plimak and M. Fleischhauer, *Stochastic simulation of a finite-temperature one-dimensional Bose gas: From the Bogoliubov to the Tonks-Girardeau regime*, Phys. Rev. A **71**, 041601 (2005).
- [123] D. J. Higham, *An Algorithmic Introduction to Numerical Simulations of Stochastic Differential Equations*, Siam Rev. **43**, 525 (2001).